LIQUID-LIQUID EXTRACTION BASED ON A NEW FLOW PATTERN: TWO-FLUID TAYLOR-COUETTE FLOW

By

Gretchen Baier

A dissertation submitted in partial fulfillment of the
requirements for the degree of

Doctor of Philosophy

(Chemical Engineering)

at the

UNIVERSITY OF WISCONSIN – MADISON

1999

LIQUID-LIQUID EXTRACTION BASED ON A NEW FLOW PATTERN: TWO-FLUID TAYLOR-COUETTE FLOW

Gretchen Baier

Under the supervision of Professor Michael D. Graham and

Professor Edwin N. Lightfoot

at the University of Wisconsin-Madison

ABSTRACT

The exploitation of flow instabilities that can occur in rotating flows is investigated as a new approach to liquid-liquid extraction. Two immiscible liquids are radially stratified by centrifugal force in the annulus between corotating coaxial cylinders. When the inner cylinder is then rotated above a critical speed, Taylor vortices form in one or both of the fluids. Although the flow pattern yields a relatively small amount of interfacial surface area, the surface is highly active for interphase mass transfer due to the local vortex motion. With the addition of countercurrent axial flow, efficient continuous processing is also possible. It is proposed that this two-fluid Taylor-Couette flow yields a viable extraction process, particularly for fluid pairs that are easily emulsifiable and therefore have limited processing options with the current commercially available equipment.

With this goal, the present study of two-fluid Taylor-Couette flow with countercurrent axial flow includes:

- A review of aqueous-aqueous and reversed micelle extraction techniques, the commercially available centrifugal extractors, and one fluid Taylor-Couette flow and its variations.
- A theoretical analysis to predict the onset of the two-fluid Taylor-Couette instability in the presence of countercurrent axial flow.
- Theoretical predictions for interphase mass transfer using a combination of penetration theory and computational fluid dynamics.
- The demonstration of two-fluid Taylor-Couette flow with countercurrent axial flow in the laboratory, including: (1) fluid mechanics studies to determine the onset of two-fluid Taylor-Couette flow, and (2) mass transfer studies to determine intraphase and interphase mass transfer characteristics.

The agreement between the theoretical analyses and the experimental results is good for both the fluid mechanics and the mass transfer. Furthermore, the extraction performance of two-fluid Taylor-Couette flow with countercurrent axial flow is very promising with the mass transfer coefficient proportional to the strength of Taylor vortices. This suggests that very high extraction efficiencies can be obtained with even larger relative rotation rates or cylinder modification to promote vortex formation.

Besides two-fluid Taylor-Couette flow, other instabilities can occur that degrade the extraction performance and should be avoided in the design and operation of an extractor. With low viscosity fluids at low rotation rates, two-fluid Taylor-Couette flow is not observed experimentally, but rather the barber pole pattern, which is believed to be a lingering gravitational effect. At high countercurrent axial flowrates, the linear stability analysis predicts a Kelvin-Helmholtz instability related to the countercurrent flow profile. When axial flow is not present, two computational fluid dynamics packages calculate that vortices paired across the interface can corotate, rather than counterrotate, with each other.

Acknowledgement

I feel very lucky to have had this wonderful project for my thesis research and I would like to thank everyone who helped make this research a success. First, thank you, Professor Graham and Professor Lightfoot, for giving me this great opportunity and for your invaluable support and advice along the way! I am also extremely grateful for the expertise and responsiveness of the machinists, John Cannon and Al Hanson, without whose help the experimental portion would not have been possible. Bill Black, Arun Kumar, and Todd Ninman have all helped me with computer related issues and Sarah Yuan with operational ones. Finally, thanks to my very special friends Amanda, Kara M., Kelly, and Jill for their unique perspectives and insights, but most of all...thanks, Jim.

Contents

List of Tables

List of Figures

Chapter 1

Introduction

Taylor-Couette flow is a centrifugally induced hydrodynamic instability that occurs in the flow between coaxial cylinders when the inner cylinder is rotated above a critical speed. Ever since G.I. Taylor's pioneering paper in 1923 [106], one fluid Taylor-Couette flow has continued to attract researchers with its structured cell patterns and its simple geometry both as an experimental device and as a mathematical model. However, in spite of the thorough analysis of one fluid Taylor-Couette flow, the extension to a two fluid analogue has received little attention. Two-fluid Taylor-Couette flow could be achieved by centrifugally stratifying two immisicible fluids and then increasing the inner cylinder rotation rate to produce two sets of counterrotating Taylor vortices; one set for each phase.

From a purely fluid dynamics standpoint, two-fluid Taylor-Couette flow is an interesting variation of the one fluid problem that explores how the interface affects the vortex flow. The range of potential flow patterns is increased, especially when gravitational forces are important, and raises a number of questions. If the vortices do form, do they have the same behavior as one fluid Taylor-Couette flow? Can the two fluid system be treated as two independent one fluid problems with a “pseudo” cylinder rotation rate and radius at the interface? Do the same transitions occur from axisymmetric time independent, to singly periodic, to doubly periodic, and to time dependent? Is there an asymptote at high rotation rates that is similar to the Rayleigh criterion for the one fluid problem?

On a more applied level, the flow behavior at the interface suggests that two-fluid Taylor-Couette flow could find a practical application in liquid-liquid extraction. The two phases retain their individual integrity and contact each other only at a single well-defined interface. The vortex motion indicates a highly active interface surface for mass transfer, a characteristic that is attractive in liquid-liquid extraction. Furthermore, the efficient method of countercurrent contacting could be accomplished by adding a weir system at the inlet and outlet ports. A two-fluid Taylor-Couette extractor is depicted in Figure 1.1.

The precedent has been set for chemical processes to exploit hydrodynamic instabilities. One fluid Taylor-Couette flow has found applications that utilize the vortex motion to increase the performance of mass transfer operations. Although a several-fold increase in filtration and reactor performance has been demonstrated, the commercial success has been limited. For large production scales, the expense of constructing and operating a Taylor-Couette device significantly reduces its cost-effectiveness. For smaller scale operations, less sophisticated methods prevail. Therefore, for a Taylor-Couette device to be commercially appealing, the process stream must be relatively high valued and of moderate flowrate. Liquid-liquid extraction of biological products could be such a niche.

Bioproducts are typically sensitive to their environment. Small changes in conditions can cause the bioproduct to deactivate and become worthless. For this reason, the many standard chemical engineering separation techniques have not been acceptable in bioprocessing. Two chemical systems for liquid-liquid extraction (aqueous-aqueous and reversed micelles) that do perform well have been developed, but in both methods the liquid pairs are easily emulsifiable. As the current commercial processes rely on dispersing one phase in the other followed by phase separation, they are inadequate for such systems. As a result, the expensive processes of electrophoresis and chromatography and the low resolution process of filtration still prevail in bioseparations.

Liquid-liquid extraction utilizing two-fluid Taylor-Couette flow addresses the limitations of the existing process equipment and offers the following potential advantages:

- Continuously stratified fluids. The elimination of dispersing one phase in the other accommodates liquid-liquid extraction fluid pairs that are easily emulsifiable. Such systems typically have low density differences, low interfacial tension, or large viscosity differences.

- Small interfacial area. Although the interfacial area is small, it is highly active due the vortex motion. Bioproducts can denature at interfaces.
- Decoupling of radial and axial transport. The radial mass transport and axial throughput can be separately controlled and optimized.
- Scale-up. The predictable flow patterns facilitate easy and reliable scale-up. The scale-up of other centrifugal extractors is based on empirical correlations.
- Axial stages. Stages sequential in the axial direction allow more flexible operation, simpler scale-up, and improved temperature control. A combination of axial and radial stages is also possible.
- Flooding. A two-fluid Taylor-Couette extractor could operate with more extreme volume ratios of the two phases without the flooding that occurs in other extractors.
- Volume efficient. Low hold-up volumes and short residence times are advantageous for hazardous, reactive, or expensive products.

- Simple mechanical design. With few moving parts and a simple geometry, the extractor would be straightforward to build, maintain, startup, operate, shutdown, and clean. Furthermore, a two-fluid Taylor-Couette extractor would be cost competitive with other centrifugal extractors.
- Solids handling. The elimination of mixing plates and diffusers provides improved solids handling without erosion or plugging to damage or unbalance the equipment.

The disadvantages of two-fluid Taylor-Couette liquid-liquid extraction include some of the standard constraints with centrifugal extractors:

- Flooding can result from unbalanced flow rates.
- The scale-up capacity is limited by practical design and operational considerations.
- Sampling along the extraction train appears impossible.
- The strong centrifugal forces introduce the possibility of debris collecting on the interface and inhibiting the mass transfer.
- The countercurrent flowrates and vortex strength must be balanced to prevent severe backflow and dispersion in extreme operating conditions, such as large viscosity ratios.

With the objective of developing two-fluid Taylor-Couette into a liquid-liquid extraction process, the following sections present (1) an introduction to the liquid-liquid extraction of biologicals and the commercial centrifugal extractors available, (2) a review of the fluid mechanics and mass transfer characteristics of one fluid Taylor-Couette flow, and (3) the theoretical and experimental results for two-fluid Taylor-Couette flow. These include the fluid mechanics, axial dispersion characteristics, and liquid extraction performance. The two-fluid Taylor-Couette extractor is compared with the commercial equipment and recommendations are provided to develop further this new extraction process.

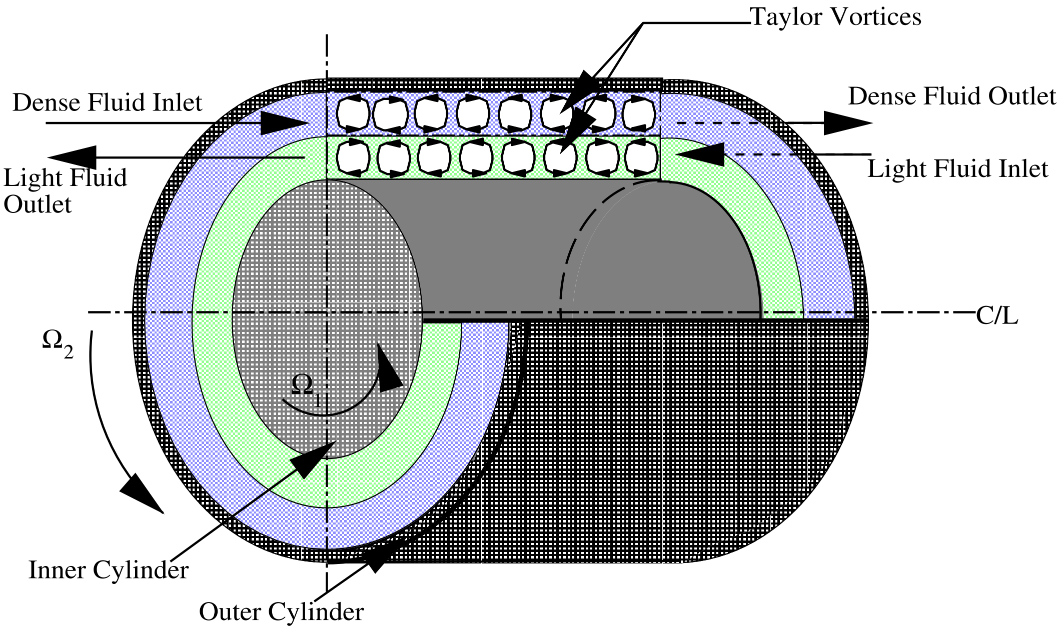

Figure 1.1: Schematic of a Two-Fluid Taylor-Couette Extractor.

Chapter 2

Background

2.1 Bioseparation Techniques

Bioproducts are typically manufactured in large, dilute, multiphase fermentation broths which can require a significant number of downstream separation trains to obtain a marketable concentration. In general, these separations may be divided into the three categories of volume reduction, fractionation, and polishing. Volume reduction is a rough cut to reduce the volume of material processed to a reasonable level. Fractionation is a more selective process to increase the concentration of the desired product. Polishing is a very selective technique to eliminate the remaining trace contaminants.

Bioseparations also differ from the standard chemical engineering operations since bioproducts are unusually sensitive to their environment. Proteins, for example, may denature if placed in an environment outside narrow limits of pH, salt concentration, temperature, and contaminating species. Denatured materials are often useless for their intended application. Therefore, the standard separation techniques of distillation, organic-aqueous liquid-liquid extraction, adsorption, precipitation, and mechanical methods are often not acceptable. The alternative techniques of chromatography and electrophoresis are often the only choices [41]. These methods can be very expensive in capital equipment required, the difficulty in scale-up, and the long residence times required. Filtration is another alternative, but has limited resolution, and membrane fouling can restrict its useful lifetime.

To address the limitations of existing fractionation techniques, two promising methods have been developed that successfully separate bioproducts by liquid-liquid extraction: aqueous-aqueous liquid extraction and reversed micelle liquid extraction. Either technique could effectively handle the volumes required for commercialization. Furthermore, the efficiency of such liquid-liquid extraction may be fine-tuned though polymer or surfactant selection to specifically target individual bioproducts for separation. This achievement alone could significantly reduce the subsequent separation steps required. However, the commercial application of liquid-liquid extraction for bioproducts has been severely limited since adequate process equipment does not exist. The current commercial equipment cannot satisfy the exacting conditions required for aqueous-aqueous or reversed micelle liquid-liquid extraction. This equipment is reviewed in section 2.2.

Aqueous-Aqueous Liquid Extraction. When two incompatible polymers are dissolved in water, the result can be two immiscible water phases: one phase that is rich in one polymer, and the other phase rich in the other polymer [3, 50]. A similar two-phase system may also be achieved with polymer - salt solutions. Multiple phases are a general response in systems containing large molecules where the energy of self-interaction is greater than the entropy of mixing. Figure 2.1 is the phase diagram for several dextran-polyethylene glycol (PEG) aqueous-aqueous systems.

These two-phase aqueous systems may be used in liquid-liquid extraction to concentrate a material of interest into a product phase. The product phase is then fractionated or polished by salt extraction, ultrafiltration, diafiltration, precipitation, or adsorption [41, 113]. Table 2.1 summarizes the partition coefficients for several proteins in PEG-dextran systems. The separation may be further enhanced by manipulating the volume ratios of the two phases.

However, the physical properties of the PEG-dextran aqueous phases are often very similar (Table 2.2) and the standard extraction processes, which rely on high density differences or high interfacial tension, are not feasible. The PEG-salt systems have higher density differences (Table 2.3) than the PEG-dextran systems, but still significantly less than the standard hydrocarbon-water two

Figure 2.1: Phase diagrams of PEG-Dextran aqueous-aqueous systems [3]. PEG (Mw = 6,000); Dextran: 1. D5 (Mn = 2,300; Mw = 3,400) 2. D17 (Mn = 23,000; Mw = 30,000) 3. D24 (Mn = 40,500) 4. D37 (Mn = 83,000; Mw = 179,000) 5. D48 (Mn = 180,000; Mw = 460,000) 6. D68 (Mn = 280,000; Mw = 2,200,000)

Protein	Molecular Weight	Dextran-40 K	Dextran-500 K
Cytochrome c	12	0.18	0.17
Ovalbumin	45	0.58	0.78
Bovine serum albumin	69	0.18	0.34
Lactate dehydrogenase	140	0.06	0.16
Catalase	250	0.11	0.79
Phycoerythrin	290	1.90	12.
β-galactosidase	540	0.24	1.59
Phosphofruktokinase	800	0.004	0.02
Ribulose diphosphate carboxylase	800	0.05	0.28

Table 2.1: Partition coefficients of proteins in Dextran-PEG 8000 (6 wt%:6 wt%) aqueous-aqueous systems $K = C_1^*/C_2^* = C_{PEG}^*/C_{Dex}^*$ [50].

wt% Dex. 500	wt% PEG 35000	wt% PEG 6000	Viscosity Relative to Water PEG-rich Phase μ_1	Dex.-Rich Phase μ_2	Viscosity Ratio μ_{21}
3.9	1.8		5.6	12.8	2.3
4.0	2.0		5.7	16.2	2.8
5.0	2.5		6.9	26.7	3.9
6.0	3.5		9.9	51.1	5.2
7.0	4.5		14.6	89.2	6.1
5.0		3.5	4.9	15.7	3.2
5.2		3.8	3.7	27.9	7.5
6.2		4.4	4.0	50.6	12.7
7.0		5.0	4.4	95.7	21.8

wt% Dextran	wt% PEG	Density at 20C PEG-rich Phase ρ_1	Dex-rich Phase ρ_2	Density Ratio ρ_{21}
8	6	1.0127	1.0779	1.0644
7	4.4	1.0116	1.0594	1.0473
5	4	1.0114	1.0416	1.0299
5	3.5	1.0114	1.0326	1.0210

wt% Dextran 500	wt% PEG 6000	Interfacial Tension (dyne/cm)
5	3.5	0.00046
5	4	0.0031
5.2	3.8	0.0021
6	4	0.007
7	4.4	0.020
8	6	0.066

Table 2.2: Physical property data for Dextran-PEG aqueous systems [3].

phase systems. Additional complications also arise with a large volume change or viscosity change of one of the phases during the extraction, as can happen with cell debris extraction [113]. Nonetheless, some of the standard techniques (Graesser contactor [29], mixer settler trains [52, 87], hollow fibers [20], packed columns [89], spray columns [95], York-Scheibel columns [59], centrifugal extractors [51, 52]) have been evaluated; the results have not been successful enough to justify standard commercial use.

Reversed Micelle Liquid Extraction. Reversed micelle liquid-liquid extraction is based on a water phase and a hydrocarbon phase. The hydrocarbon phase contains a concentration of surfactant above the Critical Micelle Concentration (CMC) in order to form micelles. The typical surfactants used in reversed micelle systems include:

- AOT - sodium di-2-ethylhexylsulfosuccinate
- DDAB - didodecyldimethylammonium bromide
- TOMAC - trioctyl methyl ammonium chloride

The hydrocarbon phase is a solvent such as iso-octane. Figure 2.2 is a schematic of the AOT/iso-octane/water phase diagram.

A reverse micelle is a group of individual surfactant molecules arranged with the hydrophilic ends concentrated together and surrounded by the hydrophobic

wt% PEG 4000	wt% K_2PO_4	wt% KPO_4	Viscosity (mPa-s) PEG-Rich Phase μ_1	Viscosity (mPa-s) Salt-Rich Phase μ_2	Visc. Ratio μ_{21}	Density (g/ml) Salt-Rich Phase ρ_2	Dens. Ratio ρ_{21}
9.55	7.36	3.68	9.49	1.21	0.13	1.116	1.053
9.42	7.58	3.79	11.66	1.22	0.10	1.129	1.056
9.19	7.98	3.99	11.89	1.60	0.13	1.136	1.060
12.00	8.26	4.13	14.39	1.60	0.11	1.147	1.069
8.67	8.91	4.45	15.33	1.22	0.08	1.140	1.066
7.93	10.2	5.1	20.29	1.27	0.06	1.149	1.079

Table 2.3: Physical property data for PEG-salt aqueous systems [59].

Figure 2.2: Ternary phase diagram for the AOT/iso-octane/water reverse micelle system [96].

ends. In this way small hydrophilic environments are created within the organic phase. When a reverse micelle hydrocarbon phase is contacted with an aqueous phase containing a bioproduct, the bioproduct may be captured into the micelle. Figure 2.3 depicts the reversed micelle separation technique.

The aqueous and hydrocarbon phases are then separated, and the process reversed to release the bioproduct into the desired product stream. Several parameters can be optimized to control the forward and back extraction of the bioproduct with the micellar phase. These include pH and ionic strength of the aqueous contacting solution, the salt and buffer type, the surfactant type and concentration, the solvent type, and the volume ratio of the aqueous contacting phase to organic reversed micelle phase [96]. The effect of pH is to control the charge distribution over the protein surface and the protein formations. The ionic strength has two effects: (1) modification of the electrostatic interactions through the electrical double layer between the micelle and the protein, and (2) the possibility to salt out the protein from the micellar phase. The salt type and buffer facilitate the transfer of the protein across a hydrocarbon layer between two different aqueous phases. The surfactant concentration controls the number of reversed micelles, and hence the capacity to contain protein. Figure 2.4 illustrates the influence of surfactant concentration and pH on the partition coefficients of ribonuclease A and concanavalin A [96].

The physical properties of the reversed micelle-aqueous two phase system (Table 2.4) are similar to the fluids used in traditional liquid-liquid extraction. Therefore, the application of existing liquid-liquid technology to the reversed micelles system should be straightforward. However, as with the aqueous-aqueous system, processes to commercialize reversed micelles separation with existing liquid-liquid extraction technologies have been investigated, but with limited success [23, 60, 92, 96]. Mixer-settlers, agitated countercurrent column contactors, and centrifugal extractors (Podbielniak and Westfalia) have been evaluated [96]. Both the centrifugal and column type contactors have performed with low stage efficiencies due to channeling, incomplete mixing, or tendency to flood. Furthermore, the high surfactant concentration can result in strong emulsions that are difficult to break [96]. Membrane contactors, which rely on the two-phase contact controlled by a semi-permeable membrane, are being investigated as a possible alternative [20].

Figure 2.3: Schematic of liquid-liquid extraction using reverse micelles [96].

Phase	Density g/ml	Viscosity cp
Octane	$\rho_1 = 0.821$	$\mu_1 = 0.542$
Water	$\rho_2 = 0.998$	$\mu_2 = 1.002$
Ratio	$\rho_{21} = 1.216$	$\mu_{21} = 1.849$
Interfacial	Tension =	50.8 dyne/cm

Table 2.4: Physical property data for reverse micelle systems

Figure 2.4: Partition coefficients in reverse micelle systems as a function of pH and surfactant concentration for (A) ribonuclease a, (B) concanavalin a. $K = C_1^*/C_2^* = C_{mic.}^*/C_{aq.}^*$. [96]

2.2 Current Equipment for Liquid Extraction of Bioproducts

The standard liquid-liquid extraction process is to disperse one phase as small droplets in the other phase. The result is a large interfacial surface area for mass transfer, but one that is relatively inactive. After mass transfer occurs, the two phases are coalesced back into two continuous phases and the phases separated to recover the product. However, the coalescence step can be difficult, if not impossible, for systems with low density differences or low interfacial tension. Furthermore, additional complications arise in bioseparations since bioproducts can be denatured at interfaces. For such systems, the ideal separator would have a minimal interfacial surface, but one that is highly active. The ideal separation device does not yet exist and centrifugal extractors are currently the best alternative.

Centrifugal extractors offer the advantages of centrifugally accelerated settling, short residence times, low holdup volumes, flexible phase ratios, and a small footprint. These characteristics are desirable in applications where throughput (petroleum industry [40]), safety (nuclear fuel reprocessing [108]), or facilitated settling (bioseparations [113]) are required. However, as centrifugal extractors are finely machined, they tend to be the most expensive type of extractor in capital investment terms.

Centrifugal extractors may be divided into the three categories: differential, multistage, or single stage contactors as in Table 2.5. The differential contactors provide continuous extraction; whereas the multistage or single stage units provide discrete steps for extraction. All of the current centrifugal extractors rely on some sort of mixing and settling process. Only in the α-Laval do the phases remain primarily stratified. The mixing disperses one phase as small droplets in the other phase to maximize the mass transfer area. Perforated plates, distributors, or mixing arms are used for this dispersion. Settling is achieved by centrifugal force to coalesce the mixture into the two continuous phases. In most cases, the fluids are pumped through the extractor and pressure control is required on the outlet streams to prevent flooding of the extractor.

The performance of centrifugal extractors are characterized by five parameters: pressure, holdup, flooding, backmixing, and efficiency. The inlet and outlet pressures determine the position of the interface between the two fluids. The interface must be located such that the extractor operates as designed, especially in the settling and weir regions. Holdup is defined as the volume fraction of the dispersed phase in the mixing zone [75] and is a coarse indication of the contact surface area. Flooding occurs when the two fluids are not effectively separated or a phase inversion occurs in the mixing zone. Flooding is a measure of the extractor capacity and can be caused by extreme heavy to light phase ratios or unbalanced outlet pressures. Backmixing is less important with centrifugal extractors than with other extractors as the centrifugal force strongly promotes unidirectional flow. Efficiency is the final and most important measure for centrifugal extractors and is highly dependent on the operating parameters involved. Centrifugal extractors typically use the efficient method of countercurrent contacting which minimizes the use of solvents and maximizes the final concentration of the solute in the extracting phase. In general, the overall efficiency of centrifugal extractors equals and exceeds that of other extractors.

Table 2.6 summarizes the typical uses for centrifugal extractors [75]. Examples of the operating and performance characteristics of centrifugal extractors are in Tables 2.7 and 2.8 [75]. The primary weakness of these extractors for bioseparations is that the mass transfer is based on dispersion of one phase in the other.

Podbielniak Extractor. The Podbielniak is the original centrifugal extractor and was designed for the large scale extraction of penicillin. The Podbielniak is divided into three zones: a mixing zone in between two settling zones. The heavy (light) fluid enters the Podbielniak from the inside (outside) radial end. Due to the centrifugal force, the light (heavy) fluid travels to the inside (outside) radius. The two fluids mix countercurrently as they pass through a series of perforated plates. Figure 2.5 is a cutaway of the Podbielniak separator. The

Horizontal Extractors	Differential	Podbielniak Quadronic Coil Planet Centrifuge *Two-Fluid Taylor-Couette*
	Multistage	Centrifugal Mixer Settler
Vertical Extractors	Differential	α-Laval UPV Coil Planet Centrifuge
	Multistage	Luwesta Robatel SGN
	Single-stage	Robatel BXP Westfalia TA SRL, ANL

Table 2.5: Classification of centrifugal extractors [75].

Figure 2.5: The Podbielniak extractor [75].

Process	Characteristics	Extractor	Feature
Pharmaceuticals Antibiotic extraction Vitamins refining	Systems easily degrade	Podbielniak, Westfalia, α-Laval, Quadronic	Sealed, fast
Atomic energy Uranium extraction and stripping	Hazardous	Robatel BXP, SRL, ANL	Small volume, shielding, small solvent inventory
Lube processing Aromatic removal	Easy emulsifiable, small density difference	Podbielniak, α-Laval	Emulsion handling, fast settling
Hydrometallurgical Metal extraction Ion exchange	Easy emulsifiable, corrosive	Podbielniak, α-Laval	Emulsion handling, compact
Solid-liquid processes Perfume extraction	Solid-liquid systems	Robatel SGN, Westfalia	Solid handling
Miscellaneous Acid treatment	Corrosive	Podbielniak, Westfalia	Compact
Ether extraction	Toxic	Podbielniak	Compact, small solvent inventory
Waste water	Dilute	Podbielniak, Quadronic	Efficient
Soap manufacture	Solids, viscous	Quadronic	Solids handling, easy cleaning

Table 2.6: Applications of centrifugal extractors [75].

mechanical design is complicated involving four rotary seals and the number of theoretical stages in these separators is low. The radial arrangement of the stages limits the number of stages, and can also require each perforated plate to be specifically designed for the variation of conditions in the radial direction [40]. The perforated plates also introduce the potential for plugging and erosion, which in the extreme could unbalance the machine.

Quadronic. The Quadronic extractor is very similar to the Podbielniak, but with a wider selection of internal mixing designs: orificed disk column, perforated strips, and sectional concentric orificed bands [75]. In addition, the Quadronic is designed to better handle solids and offers multiple inlet and exit ports.

α-Laval Extractor. The α-Laval extractor is a vertical extractor with the two phases entering at the bottom of the extractor; the light (heavy) fluid introduced at the outer (inner) radial position. As fluids are pumped through the extractor they the move countercurrently through a series of concentric cylinders. The two fluids remain stratified except at the small crossover zone to direct the fluids from one annulus to the next. The mass transfer surface area is less than that in the dispersed phase systems, however for easily emulsifiable phases this is an acceptable compromise. The lack of perforated plates is also more amenable to solids handling. When operated at rigid rotation, the two-fluid

Extractor	Model	Vol. (m^3)	Capacity (m^3/hr)	$\bar{t}$ min	rpm	Axis	Diam. (m)
Podbielniak	E 48	0.925	113.5	0.5	1,600	Hor.	1.2
Quadronic	H 4848	0.9	72	0.75	1,500	Hor.	1.2
α-Laval	ABE 216	0.07	21	0.2	6,000	Ver.	-
UPV	-	-	6	-	1,400	Ver.	-
Luwesta	EG 10006	-	5	-	4,500	Ver.	-
Robatel SGN	LX6 70NL	0.072	3.5	1.2	1,600	Ver.	1.3
Robatel BXP	BXP 800	0.220	50	0.3	1,000	Ver.	0.8
Westfalia	TA 15007	0.028	30	0.06	3,500	Ver.	0.7
SRL/ANL	-	0.003	0.05	3.6	3,500	Ver.	0.1
Coil Planet	-	0.0003	0.00012	150	1,600	H/V.	0.05
Centr. Mix-Set	-	0.0023	0.64	0.22	4,800	Hor.	0.094
TFTC	-	0.0008	0.0024	20	450/750	Hor.	0.1
	-	0.0008	0.0066	7.3	450/750	Hor.	0.1

Table 2.7: Typical operating conditions for centrifugal extractors [75].

Figure 2.6: The α-Laval extractor [75].

Extractor	System	ρ_{hvy}/ρ_{lgt}	rpm	Q_h/Q_l	Q_f (m^3/hr)	No. Th. Stages
Pod.						
B-10	Kerosene-NBA-Water	1.25	3000	0.5	5.1	6-6.5
D-18	Kerosene-NBA-Water	1.25	2000	0.5	11.1	5-5.5
A-1	Oil-aromatics-phenol	1.15	5000	3.5	0.01-0.02	5-7.7
9000	Broth-penicillin B - pentacetate		2900	4.4	7.5	1.8
			2900	2.4	7.5	2.21
9500	Oil-aromatics-furfural		2000	4.0	12.0	3-6
A-1	Isoamyl alc - boric acid - water	1.23	5000	1-03	0.01-0.03	3.5-7.7
			3000	1.0	0.01	2.3
			4600	1.0	0.01	2.96
UPV	Oil-aromatics-phenols	1.11	1400	0.8-1.2	6	2-5.8
Rob. SGN						
LX-168N	Uranyl nitrate-30% TBP		1500	1-0.2	2.1-4.5	7
LX-324	Some system		3100	1.6	24-63	3.4-3.9
SRL 1 stg	Uranyl nitrate-ultrasene		1790	0.5-1.5	6.4-12	0.92-0.99
ANL 1 stg	Uranyl nitrate-TBP/dodecane		3500	0.3-4	0.8-1.6	0.97-1
Centr. Mix-Set.	Toluene-acetone-water	1.15	4800	1	0.64	3.5
TFTC	D35/IsoParL-glyc./water-various	1.36-1.5	450/750	1	0.0024	4.5
		1.36-1.5	450/750	1	0.0066	1.5

Table 2.8: Performance of centrifugal extractors with model systems [75].

Taylor-Couette extractor is very similar to the α-Laval. Figure 2.6 illustrates the α-Laval extractor.

The Unpressurized Vertical Extractor. The Unpressurized Vertical (UPV) Extractor is similar to the Podbielniak Extractor except the device is vertical and the phases enter from the top and move downward through the extractor under gravity. Again, the light fluid is introduced near the periphery and the heavy fluid near the shaft. As the fluids move downward, they are mixed while radially convected through the perforated plates by the centrifugal force.

Luwesta Extractor. The multistage Luwesta Extractor operates with several distinct mixing and settling chambers. The fluids enter the top of the extractor under pressure. The fluids are forced to flow countercurrently with the heavy (light) fluid beginning its cycle at the bottom (top) of the extractor. The fluids are simultaneous pumped and centrifuged by angled baffles. In each chamber the two phase are (1) mixed as they passed through a distributor ring, (2) stratified in the chamber by centrifugal force, and (3) separated by a weir system and directed to the next chamber. The Luwesta is essentially a discrete staged version of the Podbielniak. Figure 2.7 diagrams the Luwesta operation. The Westfalia TA is a single stage version of the Luwesta and may also be operated in series.

Figure 2.7: The Luwesta extractor [75].

Figure 2.8: The Robatel SGN extractor [75].

Robatel Extractor. The Robatel SGN Extractor consists of several chambers stacked vertically and configured for countercurrent extraction. Each chamber is physically divided into three sections. In the central section a mixing disk extending off the stationary shaft into the rotating drum mixes the two fluids. The disk also sends the mixture to the settling section where the two phases are separated. A weir system directs the fluids to the next chamber. The lack of perforated plates makes this design attractive to solids handling. The Robatel has a particularly compact construction with the motor protected and is therefore preferred in hazardous services. Figure 2.8 diagrams the Robatel operation.

The Robatel BXP extractor is a single stage extractor very similar in concept to the Robatel SGN system and consists of a stirred mixing chamber followed by stratification and separation zones. These single stages may be operated in series to achieve the multiple stages required for a specific application.

Argonne National and Savannah River Laboratory Extractors. The Argonne National Laboratories (ANL) extractor is very similar to the extractors investigated for dispersed two-fluid Taylor-Couette flow but the flow is often cocurrent [72, 109]. Two fluids enter tangentially the bottom of an annular region. The rotating shaft emulsifies the two phases as they move cocurrently up the annulus. At the top the phases are separated by centrifugal force and collected by weir system. The bottom of the shaft is not supported to minimize corrosion problems but also limits the maximum rotation rate possible. The Savannah River Laboratories (SRL) Extractor operates almost identically, but with the added features of radial mixing vanes to facilitate mixing and a radial weir system. These types of extractors are constructed specifically for the requirements of the nuclear industry, where safety, corrosion, and containment are the major concerns. Vortex motion is probably present in the emulsion and resembles one-fluid Taylor-Couette flow. As a result, the efficiency of the extractors may be improved by a decrease in axial dispersion. Figure 2.9 illustrates the principles of the SRL reactor.

The Centrifugal Mixer Settler. A novel separation device that has not been pursued past the initial paper is the centrifugal mixer-settler [38]. Similar to the other centrifugal extractors, especially the SRL extractor, the centrifugal mixer settler relies on a series of mixing steps followed by stratification by centrifugal force. The mixers in this case are a series of paddles attached to an inner cylinder of a horizontal Couette device. The settlers are zones between the paddles, where the centrifugal force segregates the fluids. Countercurrent axial flow is accomplished by a slight tilt to the apparatus and a series of weirs to distribute the inlet and outlet flows. Rotary seals are eliminated by an effective air seal. Figure 2.10 is a schematic of the centrifugal mixer settler design.

Figure 2.9: The Savannah River Laboratory extractor [75].

Figure 2.10: Schematic of the Centrifugal Mixer Settler [38].

The Coil Planet Centrifuge. The most recent promising new bioseparation process is high speed countercurrent chromatography using the coil planet centrifuge. The planet centrifuge system is based on the “Archimedean screw” principle and consists of a helical coil rotating about both its own axis and an external axis as depicted in Figure 2.11. When the coil is filled with one phase (the stationary phase), and another phase (the mobile phase) is introduced at one end of the rotating coil, the two phases will compete for forward movement. Eventually, hydrodynamic equilibrium is reached with both phases distributed throughout the coil and the mobile phase emerging from the other end at a rate equal to the feed rate. With the introduction of a solute, this operation is a form of chromatography with the elution of the solute based on its partition coefficient between the two phases. Countercurrent flow is also possible when both phases are mobile as in liquid-liquid extraction.

The external centrifugal force is used to create alternating regions of favorable and unfavorable density stratification which, in effect, act as a series of mixer-settlers. The mixing occurs where the centrifugal force mixes the two phases due to the unfavorable density distribution. The settling occurs where the centrifugal force successfully stratifies the two fluids. Figure 2.12 illustrates the fluid motion [54]. Separations on this prototype require a few hours [18]. Larger and smaller versions have been successfully operated, but the scale-up

Figure 2.11: Schematic of the Coil Planet Centrifuge [54].

Figure 2.12: The mixing zone of a Coil Planet Centrifuge [54].

potential is limited by practical considerations. The strong mixing and subsequent settling stages can require small throughput rates or limit the phases to systems with higher interfacial tensions and density differences. In addition, high viscosity fluids are difficult to clean out and require high pressure drops for flow through the small tubing. Plugging can result from cell debris or other material stuck to the tubing wall by the large centrifugal forces.

2.3 One Fluid Taylor-Couette Flow

To develop a two-fluid Taylor-Couette flow system into a viable extractor, the hydrodynamics, mass transport, and other characteristics of the flow must be quantified. Since one fluid Taylor-Couette flow is the basis for two-fluid Taylor-Couette flow and has been very well researched, it is the logical starting point for the two fluid case.

Brief History of Taylor-Couette Flow. One fluid Taylor-Couette flow has been extensively studied ever since G.I. Taylor published a complete theoretical and experimental analysis [106] on what was to become known as Taylor-Couette flow. The first recorded reference to Couette flow is in Newton's 1687 work, *Principia*, where he noted its symmetry and hypothesized concentric streamlines [27]. Much later, in 1848 Stokes predicted that eddies would form in Couette flow when the inner cylinder is rotated faster than the outer cylinder. He also proposed that the use of motes (dust particles) would provide flow visualization to confirm his hypothesis. In 1881, Margules recognized that Couette flow could be used to measure viscosity, and around 1888 Mallock constructed such a viscometer. Mallock made the following observations: (1) The flow was always unstable when the inner cylinder rotated faster than the outer cylinder, and (2) When the inner cylinder was held fixed, the flow was stable up to the critical value of the outer cylinder rotation rate where turbulence sets in. Around the same time, Couette constructed a similar viscometer but with only outer cylinder rotation possible. Consistent with the results of Mallock, Couette reported the onset of turbulence at a critical outer cylinder rotation rate. Since the work of both Mallock and Couette was primarily focused on viscosity measurement, experiments in hydrodynamic instability were not pursued. Later researchers did show, however, that with his inner cylinder rotation experiments, Mallock was always above the critical rotation rate for hydrodynamic instability. In addition, the early onset of turbulence with outer cylinder rotation was due to eccentricity in the cylinder alignment.

Rayleigh's Criterion. The first major attention given to the possibility of hydrodynamic instability in Couette flow was by Rayleigh in 1920. Rayleigh's interest was stimulated by a meteorological study of cyclones. He was also aware of the results of Couette and Mallock and argued for the centrifugal instability of an inviscid fluid based on the following energy analysis. For purely azimuthal, axisymmetric, inviscid flow, the equation for the conservation of angular momentum, neglecting gravity, reduces to

$$\frac{D(ru_\theta)}{Dt} = 0.$$

This equation requires the angular momentum per unit mass to be constant, $ru_\theta = \Omega r^2 = C$ and the kinetic energy may be expressed in terms of this constant, $\mathrm{K} = \frac{\rho}{2}\frac{C^2}{r^2}$. When the flow is considered to be a series of equal volume coaxial rings, the total energy of two rings is then K $= \frac{\rho}{2}(\frac{C_1^2}{r_1^2} + \frac{C_2^2}{r_2^2})$. The first ring is at r_1 with angular momentum C_1, the second at r_2 with C_2, and $r_2 > r_1$.

When the two rings are interchanged such that ring 1 is at r_2 and vice versa, the exchange of kinetic energy is $\Delta K = \frac{\rho}{2}(C_2^2 - C_1^2)(\frac{1}{r_1^2} - \frac{1}{r_2^2})$. If $C_1 > C_2$ the second configuration is preferred as kinetic energy would be released. This implies that the flow would be unstable when the square of the angular momentum decreases with increasing radial position anywhere in the domain. For Couette flow, this Rayleigh criterion can be written, in terms of experimentally controllable parameters, as

$$\Omega_2/\Omega_1 > (R_1/R_2)^2. \tag{2.1}$$

The Rayleigh criterion may also be proved rigorously for an inviscid fluid [30]. For a viscous fluid, there is damping and the Rayleigh criterion is an outer limit. At high outer cylinder rotation rates, the viscous forces become less important compared to the dynamic forces and the Rayleigh criterion is approached as an asymptote. These effects are observed experimentally.

One Fluid Taylor-Couette Flow. Taylor extended the theoretical predictions of Rayleigh and the experimental observations of Mallock to include the centrifugal instability of a viscous fluid. He solved the equations of motion and continuity for Couette flow and then added a small disturbance flow. Based on his prior experimental observations, Taylor assumed axisymmetry, a gap narrow compared to the cylinder radii, negligible gravitational effects, and an axially periodic disturbance flow. He then solved the linearized characteristic equation for the eigenvalue corresponding to the growth rate of the disturbance. The Taylor-Couette analysis is summarized below.

The base flow for Taylor-Couette flow is Couette flow. The inner cylinder has radius R_1 and rotates at an angular velocity Ω_1. The outer cylinder is similarly described but with subscripts 2. The kinematic viscosity of the fluid is ν. When the equations of motion and continuity are solved with no slip boundary conditions at the cylinder walls, the Couette solution has only an angular velocity component:

$$V = Ar + \frac{B}{r} = \Omega r, \tag{2.2}$$

where

$$A = \frac{\Omega_1 (R_{12}^2 - \Omega_{21})}{R_{12}^2 - 1},$$
$$B = \frac{\Omega_1 R_1^2 (\Omega_{21} - 1)}{R_{12}^2 - 1},$$
$$R_{12} = \frac{R_1}{R_2},$$

and

$$\Omega_{21} = \frac{\Omega_2}{\Omega_1}.$$

The Taylor-Couette disturbance velocity is assumed to be periodic

$$\mathbf{v} = \begin{pmatrix} v_r \\ \\ v_\theta \\ \\ v_z \end{pmatrix} e^{i\alpha(z-ct+n\theta)}, \tag{2.3}$$

where the gap width is $d = R_2 - R_1$, $t = t^*\nu/d^2$, $r = r^*/d$, and $z = z^*/d$. The variables t^*, r^*, z^* are dimensional. The azimuthal wavenumber, n, is zero for axisymmetric flows. The scaled axial wavenumber is α and c is the wave speed of an imposed disturbance. When the imaginary part of c is negative ($Im(c) < 0$) the flow is linearly stable to external disturbances; when the imaginary part of c is positive ($Im(c) > 0$) the disturbance will grow to represent a hydrodynamic instability. The point where the imaginary part of c is zero ($Im(c) = 0$) is the neutral point where a disturbance will neither grow nor decay and indicates a transition point between linearly stable and unstable flow. The total flow pattern is then

$$\mathbf{V} = V\mathbf{e}_\theta + \mathbf{v}$$

and is inserted into the equations of motion and continuity. The resulting equations are linearized by neglecting the terms containing disturbance velocity products. As the disturbance velocity is considered small compared to the base flow, the products between two disturbance velocities is very small. The linearized system may be simplified to two equations:

$$[DD_* - \alpha^2 + i\alpha c](DD_* - \alpha^2)v_r = \frac{2\Omega\alpha^2 d^2}{\nu} v_\theta,$$

$$[DD_* - \alpha^2 + i\alpha c]v_\theta = \frac{2Ad^2}{\nu} v_r$$

with the no slip boundary conditions $v_r = v_\theta = v_z = 0$ at $y = 0, 1$. Here $y = r - \frac{1-\epsilon}{\epsilon}$ $(0 \le y \le 1)$, $\epsilon = d/R_2$, $D = \partial/\partial y$, and $D_* = D + \frac{1}{y+(1-\epsilon)/\epsilon}$. In the narrow gap limit ($\epsilon = d/R_2 \to 0$, so $D_* \to D$ and $\Omega \to [1-(1-\Omega_{21})y]$) and the two equations simplify to

$$[D^2 - \alpha^2 + i\alpha c](D^2 - \alpha^2)v_r = [1-(1-\Omega_{21})y]v_\theta, \tag{2.4}$$

$$[D^2 - \alpha^2 + i\alpha c]v_\theta = -T\alpha^2 v_r \tag{2.5}$$

where v_r has been rescaled to

$$v_r = \frac{2\Omega_1 d^2}{\nu} v_r$$

and

$$T = \frac{-4A\Omega_1 d^4}{\nu^2} = -\frac{4\Omega_1^2 d^4 (R_{12}^2 - \Omega_{21})}{\nu^2 (R_{12}^2 - 1)} = \epsilon Re_\theta^2 + O(\epsilon^2)$$

where

$$Re = \frac{(\Omega_1 - \Omega_2) d R_1}{\nu}.$$

The Taylor number, T, is a meaure of centrifugal to viscous forces. As the subsequent analysis will show, when the Taylor number exceeds a critical value, the flow becomes unstable and Taylor vortices form. Equations 2.4 and 2.5 can be combined into one sixth order differential equation

$$[D^2 - \alpha^2 + i\alpha c]^2(D^2 - \alpha^2)v_\theta = -T\alpha^2[1 - (1 - \Omega_{21})y]v_\theta \tag{2.6}$$

with the no slip boundary conditions

$$y = 0, 1 \quad v_\theta = 0$$

$$y = 0, 1 \quad v_r = 0 = (D^2 - \alpha^2)v_\theta$$

$$y = 0, 1 \quad v_z = 0 = D(D^2 - \alpha^2)v_\theta = Dv_r$$

At the critical point ($c = 0$) and near rigid rotation ($\Omega_{21} \approx 1$), Equation 2.6 simplifies, at leading order, to an analytically solvable differential equation

$$[D^2 - \alpha^2]^3 v_\theta = -T\alpha^2 v_\theta.$$

The solution has the form

$$v_\theta = C_1 \cosh q_0 x + C_2 \sinh q_0 x + C_3 \cosh qx + C_4 \sinh qx + C_5 \cosh q^* x + C_6 \sinh q^* x$$

where, iq_0, q, q^* are roots to the equation $(q^2 - \alpha^2)^3 = -T\alpha^2$ and $x = y - 1/2$. The symmetry of the boundary conditions further require the solution to be either even or odd relative to the gap centerline ($x = 0$). Therefore, the six no slip boundary conditions reduce to a system of three equations of the form $AC = 0$. This system of equations is identical to the Bénard convection problem for the thermal instability of a fluid contained between two rigid plates of different temperatures [14]. For the even solution

$$\begin{pmatrix} v_\theta|_{x=1/2} \\ v_r|_{x=1/2} \\ v_z|_{x=1/2} \end{pmatrix} = \begin{pmatrix} \cos\frac{q_0}{2} & \cosh\frac{q}{2} & \cosh\frac{q*}{2} \\ -q_0\sin\frac{q_0}{2} & q\sinh\frac{q}{2} & q*\sinh\frac{q*}{2} \\ \cos\frac{q_0}{2} & \frac{(i\sqrt{3}-1)}{2}\cosh\frac{q}{2} & -\frac{(i\sqrt{3}+1)}{2}\cosh\frac{q_*}{2} \end{pmatrix} \begin{pmatrix} C_1 \\ C_3 \\ C_5 \end{pmatrix} = 0$$

For a nontrivial solution to exist the determinant of A must equal zero. This determines a characteristic equation in terms of the unknowns, α and T. For a given value of α, the critical Taylor number, T_c, can thus be determined by numerical methods.

The above solution is valid at rigid rotation. A perturbation solution expands the rigid rotation solution for small deviations from rigid rotation. When the small parameter, δ, is defined as $\delta = -2(1-\Omega_{21})/(1+\Omega_{21})$ and the disturbance velocities are expanded as $\mathbf{v} = \mathbf{v_0} + \delta\mathbf{v_1} + \delta\mathbf{v_2} + ...$, the next term in this perturbation solution is of order δ^2, not δ. This result demonstrates why the leading order rigid rotation solution is actually very accurate for small deviations from rigid rotation [14].

The neutral curves (α vs. T_c) for the first even and odd solutions are in Figure 2.13. The even solution corresponds to axisymmetric pairs of counter-rotating vortices and occurs at a lower Taylor number than the odd solution. The minimum wavenumber, α, for the even solution occurs at 3.114 ($\alpha = \pi/l$ where l is the vortex length scaled with the gap width d), which indicates the vortices should be approximately square, with length approximately equal to the gap width. Figure 2.14 includes a schematic of the streamfunction for the even solution of one fluid Taylor-Couette flow.

The odd solution has two rows of vortices with a minimum wavenumber, α, of 5.365. Each vortex is approximately square, with length equal to half the gap width. The odd solution is also the solution for two-fluid Taylor-Couette flow with two identical fluids. Figure 2.14 includes a schematic of the odd solution for one fluid Taylor-Couette flow.

For the case of counterrotating cylinders, the Taylor vortex does not extend the full gap between the cylinders, but rather only from the inner cylinder to a nodal surface at $r = R_n$, where the effective rotation rate Ω_n is zero.

Taylor's subsequent experiments showed remarkable agreement with his predictions for the even solution [106]. His experimental apparatus was a vertical assembly 90 centimeters long bolted to the laboratory walls and floor to minimize vibrations. Both cylinders could rotate in either direction. The outer cylinder, $R_2 = 4.035 \pm 0.01$ cm, included at 20 centimeter long glass section for visual observation. The inner cylinder consisted of a turned paraffin wax cylinder mounted on a $\frac{3}{4}$ inch steel shaft. The inner cylinder radii investigated ranged from $2.93 \leq R_1 \leq 3.80$ cm. To reduce end effects, the cylinders were supported on steel balls to retain alignment without runout. Both cylinders were driven by an electric motor with a governor and heavy plane bearings provided smooth cylinder rotation. The ratio of angular velocities could be varied continuously

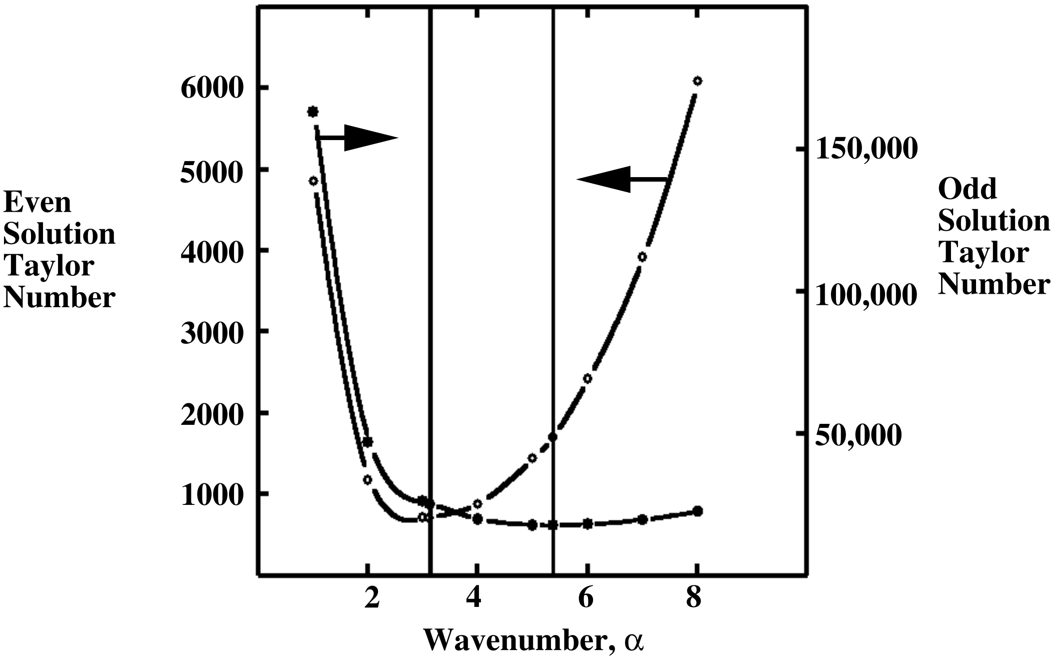

Figure 2.13: The neutral curve for the even and odd solutions of one fluid Taylor-Couette flow.

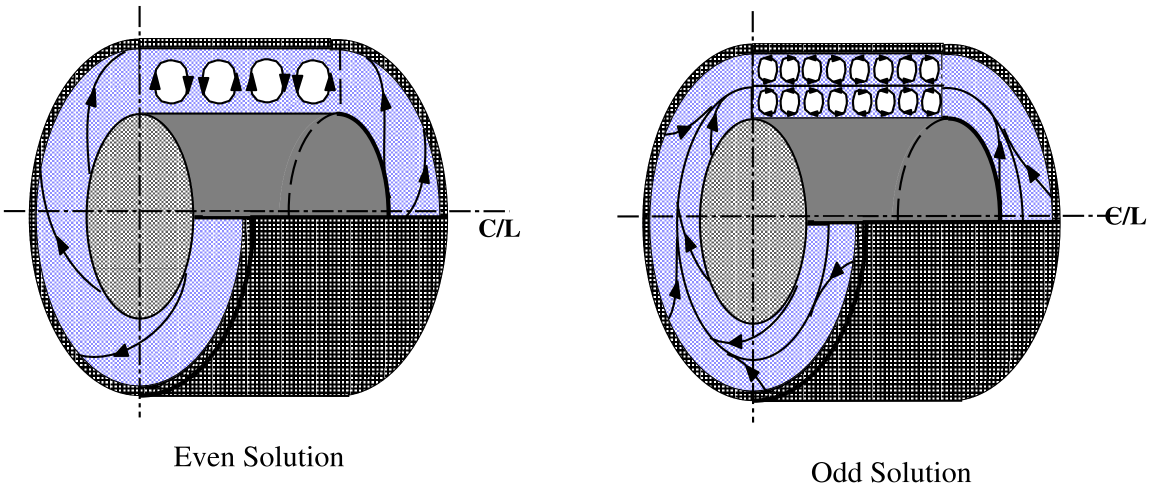

Figure 2.14: Schematic of the even and odd solution flow patterns in one fluid Taylor-Couette flow.

with a variable speed gear. The rotation rates were controlled to ±0.5%. Boiled water was the experimental fluid with the temperature controlled to ±0.2°C. Dye injections through ports in the inner cylinder provided flow visualization. Below the critical Taylor number, the dye remained near the inner cylinder. At the critical Taylor number, the dye was swept towards the outer cylinder at intervals equal to the axial spacing of the vortex outflow boundaries [106].

Variations on One Fluid Taylor-Couette Flow. Since Taylor's paper [106], subsequent work has focused on variations of the base case studied by Taylor and on its potential applications. These have included the onset of non-axisymmetric and time dependent flow patterns [4, 30, 69], end effects [65], hysteresis [4, 65], cylinders with axes parallel but offset [65], imposed axial flow [14, 49], axial dispersion [32, 83], mass transport characteristics [62, 63, 71], and centrifugal stratification [103]. The one fluid results applicable to the development of a two-fluid Taylor-Couette extractor are outlined below.

Subsequent Bifurcations and Hysteresis. As the Taylor number is increased past its critical value, the stationary, axisymmetric vortices become non-axisymmetric and eventually doubly periodic. Further increases lead to turbulent vortices and eventually featureless turbulence. The odd solution is never observed experimentally. The ramp rate used to reach the critical point influences the axial wavenumber achieved. High ramp rates lead to a higher wavenumber and thinner vortices [4, 65]. Once the vortices are formed, further changes to the cylinder rotation rates do not affect the wavenumber.

Eccentricity. Cylinder alignment can be measured by eccentricity which is defined as the ratio of the distance between the two parallel cylinder axes to the mean gap width ($ecc. = e/d$). Eccentricity stabilizes Taylor-Couette flow and decreases the critical wavenumber; a higher Taylor number is required for the onset of instability and wider vortices are formed. Figure 2.15 illustrates the influence of eccentricity on the critical Taylor number and wavenumber[66].

End Effects. The number of vortices filling the gap must be an integer. As a result, when the aspect ratio (length of cylinders/gap width) of the cylinders is sufficiently small, the aspect ratio and not the hydrodynamics determines axial wavenumber. Therefore, large aspect ratios are used to minimize these geometry effects, but they never completely eliminate end effects. Taylor vortices form prematurely at the ends and propagate down the annulus as the Taylor number increased [65] as illustrated in Figure 2.16. When the end plates rotate with the outer cylinder, the end vortices are slightly larger than the vortices further from the endplates and their size is independent of further increases in the Taylor number. The radial component of the flow next to the end plate is inward. In contrast, when the end plate rotates with the inner cylinder, the size of the end vortex is proportional to $\sqrt{T/T_c}$. As the Taylor number increases, the end

Figure 2.15: The effect of eccentricity on the critical Taylor number and wavenumber in one fluid Taylor-Couette flow. Eccentricity is defined as the offset distance of the cylinder axes to the average gap width. T_c is the critical Taylor number with eccentric cylinders; T_{co} is the critical Taylor number with concentric cylinders ($ecc = 0$). [66]

Figure 2.16: Schematic of the premature formation and propagation of vortices at the cylinder ends in one fluid Taylor-Couette flow. The outer cylinder is stationary and the endplates are rotating with the inner cylinder. Therefore, the radial flow is directed outwards at the ends. Length/gap width $= 10$, $R_{12} = 0.933$ and $R = \Omega_1 R_2^2/\nu$. [65]

vortex expands and the internal vortices are compressed. The radial component of the flow near the end plate is outward. The preferred configuration is typically endplate rotation with the outer cylinder [65].

One Fluid Taylor-Couette Flow with Axial Flow. The approach to the one fluid Taylor problem with a small superimposed axial flow is similar to the one fluid problem without axial flow [14]. The flow is described by (1) Couette flow, $V(r)$, (2) a constant axial pressure-driven flow, $W(r)$, and (3) the disturbance flow, $\mathbf{v}$. The equations of motion and continuity are solved for the base flow with no slip boundary conditions to determine V and W. The disturbance velocities are again assumed to have the form $(v_r, v_\theta, v_z)e^{i\alpha(z-ct)}$. At low flow rates, experimental results and full numerical analyses support that the flow pattern is axisymmetric [14, 85, 104]. The total flow pattern is substituted into the equations of motion and continuity. The resulting equations are linearized and combined into two differential equations. To solve these equations with the no-slip boundary conditions, the following simplifications are made: (1) the gap width is assumed small compared to the cylinder radii, (2) the base flows (V, W) are approximated by their radially averaged values $(\bar{V}, \bar{W})$, (3) the rotation rates are assumed to be nearly rigid ($\Omega_{21} \approx 1$), and (4) the axial flow rate is assumed small. The simplified equations are:

$$\{[D^2 - \alpha^2 + i(\alpha c - Re_{ax}\alpha)](D^2 - \alpha^2) - 12iRe_{ax}\alpha\}v_r = v_\theta, \tag{2.7}$$

$$[D^2 - \alpha^2 + i(\alpha c - Re_{ax}\alpha)]v_\theta = -\bar{T}\alpha^2 v_r, \tag{2.8}$$

where $\bar{T}$ is the Taylor number,

$$\bar{T} = -\frac{1}{2}(1+\mu)\frac{4A\Omega_1}{\nu^2}d^4,$$

Re_{ax} is the axial Reynolds number,

$$Re_{ax} = \frac{\bar{W}d}{\nu},$$

and $\bar{W}$ is the mean axial velocity,

$$\bar{W} = -\frac{d^2}{12\rho\nu}\left(\frac{\partial p}{\partial z}\right)_0.$$

As in the case without axial flow, for a given wavenumber, α, the characteristic equation determines the critical Taylor number, $\bar{T}_c$. Chandrasekhar [14] finds that the imposition of axial flow stabilizes the Taylor-Couette flow, or for a given geometry and fluid properties, higher Taylor numbers are required to obtain the Taylor-Couette instability in the presence of axial flow. In addition, the axial wavenumber increases with increasing axial flow which indicates that the vortices become thinner and more rectangular.

Ng and Turner computationally observe similar effects; increasing the axial flowrate is stabilizing and increases the axial wavenumber [85]. In the axisymmetric case, at very high axial Reynolds numbers, they find that a second bifurcation dominates and is reported to be a Tollmien-Schlichting shear instability in the boundary layer and not Taylor-Couette flow.

Howes and Rudman show numerically that for axisymmetric flows, some streamlines (in a reference frame traveling with the wavespeed) “bypass” the vortices [48] and flow counter to the prevailing axial flow direction; the center of the vortex travels faster than the mean axial flow velocity. The stream function for Taylor-Couette flow with axial flow is in Figure 2.17.

At sufficiently high axial flowrates ($Re_{ax} > 20$), the flow patterns observed experimentally and predicted theoretically are non-axisymmetric [85, 104]. In a non-axisymmetric analysis, Ng and Turner still find that axial flow is stabilizing and the axial wavenumber increases, but both effects are less than in the axisymmetric case. Also, the Tollmien-Schlichting instability is not observed. Figures 2.18 and 2.19 compare the axisymmetric and non-axisymmetric predictions by Ng and Turner with the theoretical predictions of Chandrasekhar and experimental observations.

Radial Mass Transport in One Fluid Taylor-Couette Flow. Radial mass transport in Taylor-Couette flow has found commmercial applications in filtration and rotating electrodes. As a result, many researchers have experimentally and theoretically investigated the radial mass transfer in Taylor-Couette flow [16, 17, 34, 46, 77, 102]. The experimental results with a stationary outer cylinder approximately satisfy the relation

$$Nu_{avg} = A(geometry) Ta^c Sc^b, \tag{2.9}$$

Figure 2.17: The stream function for Taylor-Couette flow with axial flow. $Ta = 55.9, R_{12} = 0.952, Re_{ax} = 2.61$. **A.** In a reference frame moving with the wavespeed. The dotted lines indicate regions where the flow bypasses the vortices and is counter to the prevailing flow direction. **B.** In a stationary reference frame. [48].

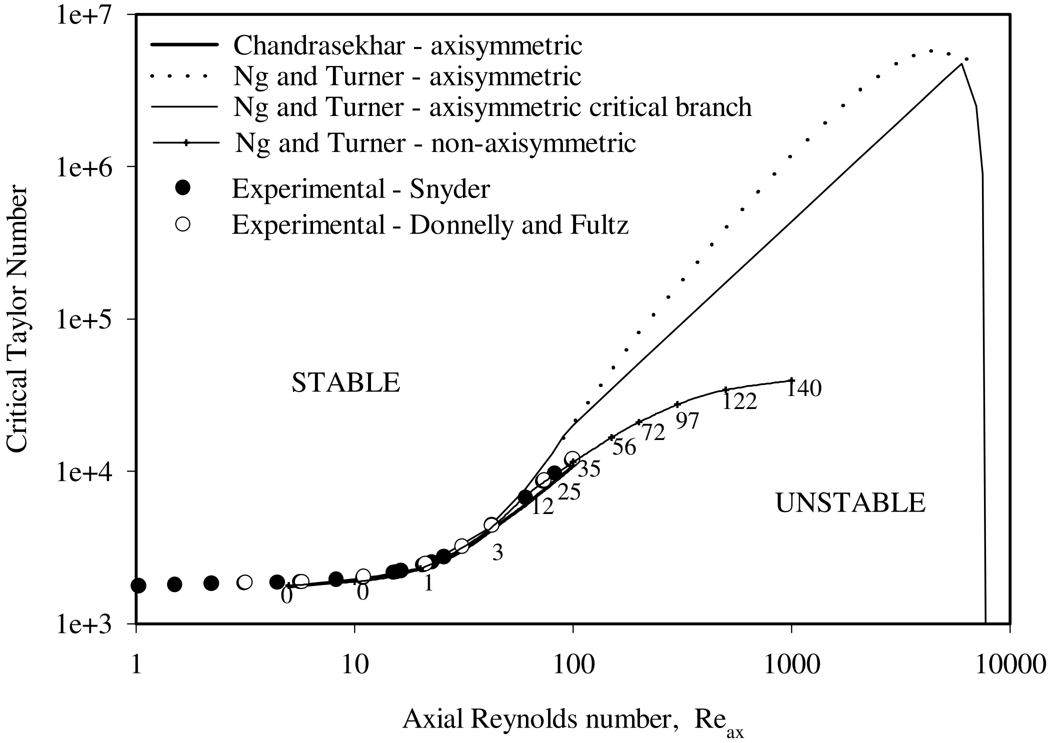

Figure 2.18: The stability curves for Taylor-Couette flow with axial flow. Ng and Turner's calculations are for $\Omega_2 = 0, R_{12} = 0.95$; the numbers represent the critical azimuthal wavenumber for non-axisymmetric flow. Snyder's data is for $\Omega_2 = 0, R_{12} = 0.949$. Donnelly and Fultz's data is for $\Omega_2 = 0, R_{12} = 0.949$.

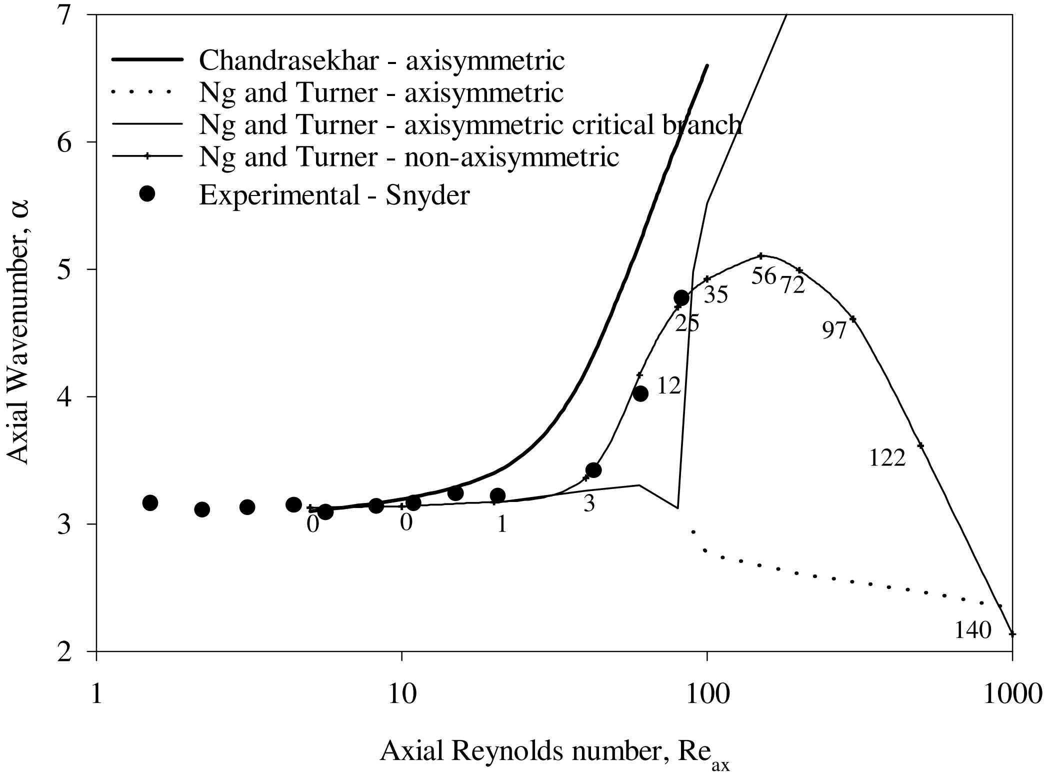

Figure 2.19: The axial wavenumbers of Taylor-Couette flow with axial flow. Ng and Turner's calculations are for $\Omega_2 = 0, R_{12} = 0.95$; the numbers represent the critical azimuthal wavenumber for non-axisymmetric flow. Snyder's data is for $\Omega = 0, R_{12} = 0.949$.

where $Nu = 2kd/D$, $Ta = \frac{\Omega_1 R_1 d}{\nu}(\frac{d}{R_1})^{1/2}$, and $Sc = \nu/D$. The empirically determined constants A, a, and b are summarized in Table 2.9. The majority of the experiments conclude that $A = 0.4 - 0.9$, $a = \frac{1}{2}$, and $b = \frac{1}{3}$. The Schmidt number dependence immediately suggests that the mass transfer is controlled by a boundary layer. Experiments have also shown that the mass transfer increases with increasing surface roughness [61, 43], also consistent with boundary layer theory where accelerated break-up of the boundary layer could increase the mass transfer. An axial Reynolds number, Re_{ax}, dependence can also appear in the Nusselt number relation, but this effect is observed only at high Reynolds numbers ($Re_{ax} > 300$) where the axial flow also significantly affects the critical Taylor number [16, 98].

Almost all of the theoretical studies have relied on approximations or empirical parameters. A weakly nonlinear stability analysis of Taylor-Couette flow predicts that the axial velocity gradient is proportional to the above defined Taylor number [21]. From boundary layer theory, the Nusselt number is then proportional to the Taylor number to the two-thirds power. This agrees surprisingly well with the experimental observations of one-half, considering that the weakly nonlinear analysis is valid only near the onset of the instability, which is not typically the region of experimental interest. Gu and Fahidy [44] also apply boundary layer theory to the mass transfer in Taylor-Couette flow, but used a parameter to fit the boundary layer equations with the empirical results. Kawase *et al.* [64] provide insight into the mass transfer characteristics of Taylor-Couette flow by comparing the numerical solution of mass transfer in a helical tube with published experimental results for Taylor-Couette flow. Flower and Macleod [35] propose a basis for a "Large Vortex Model", claiming the mass and momentum transport analogy is not valid for Taylor-Couette flow due to the dissimilar boundary conditions. Similarly, Eisenberg *et al.* [31] cautiously compare their experimental results with the Chilton-Colburn relation and Simmers and Coney [98] evaluate an analogy between heat and momentum transport.

Baier *et. al* (see also sections 4 and 5) demonstrated that the experimental results may be accurately predicted without empiricism by using a combination of computational fluid dynamics (CFD) and boundary layer theory [6]. They calculate that $Nu \propto Ta^{0.46}$, which agrees well with the experimental exponents of 1/2 for Taylor-Couette flow as well as experiments in other systems with laminar boundary layers. The predicted amplitude also agrees with the highest predicted Nusselt numbers and is within a factor of three of most of the experimental results, which include a wide range of geometries, systems, and measuring techniques. Figure 2.20 and Table 2.9 compare the CFD/boundary layer theory predictions with the experimental observations.

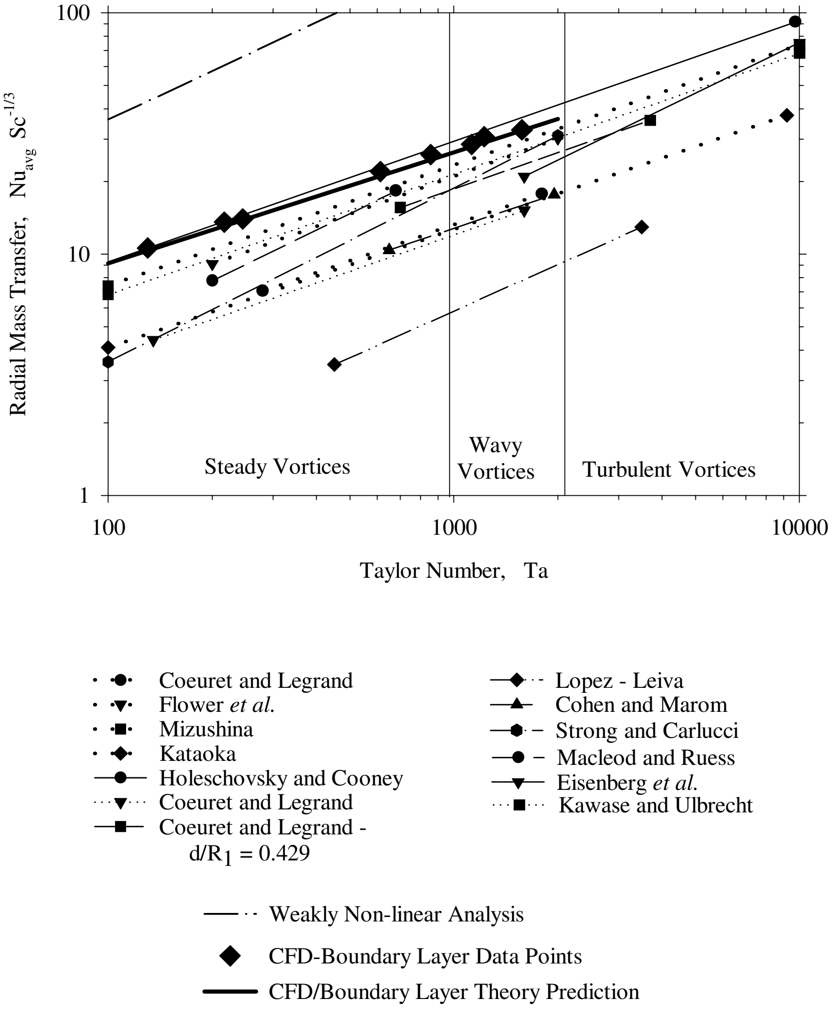

Figure 2.20: Comparison of the radial mass transfer Nusselt numbers observed experimentally and predicted by boundary layer theory combined with Computational Fluid Dynamics.

Authors	**Method**	**A**	**c**	**b**	**d/R_1**	**Re_{ax}**	**Ta**	**Sc**
Holeschov. [46]	Filtration	0.93	0.5	1/3	0.04-0.148	25-300	68-9740	21,600
Mizushina [46]	Electrode	0.74	0.5	1/3	0.62,0.82	0	59-19,500	3000-770,000
Kawase [64]	Helical Tube analogy	0.68	1/2	1/3	–	0	100-10,000	>10
Flower [34]	Falling film	0.70 ≈ 0.58 if $b = 1/3$	0.52	0	0.15	140-2600	200-2000	1.74
Coeuret [16]	Electrode	0.38	0.5	1/3	0.143, 0.286	30-300	135-1600	1380-6450
Legrand [70]		0.59	0.5	1/3	0.429	30-300	700 - 3700	1380-6450
		0.42	0.5	1/3	0.286	30-300	280-1800	1380-6450
Cohen [17]	Gas Reactor	$0.41/Pr^{1/3}$ $= 0.46$ if $Pr = 0.7$	0.482	1/3	0.62	0-50	650-1950	–
Kataoka [46]	Electrode	0.43	0.49	1/3	0.62	0	100-9200	3000-800,000
López-Leiva [46]	Filtration	0.07	0.64	1/3	0.143	150	450-3500	≈17,000
Macleod [77]	Falling Film	2.1 ≈ 0.19 if $b = 1/3$	0.7	0	0.312	33-100	200-680	1260
Grifoll [43]	Electrode	0.21	0.7	1/3	0.79	0	>48,500	770-8000
Strong [102]	Oxygenator	$0.0017/Ta_c^{0.72}$ ≈ 0.13 if $b = 1/3$	0.72	1.5	0.095	2-200	40-2000	350-420
Eisenberg [31]	Electrode	0.12	0.7	0.356	0.7-5.94	0	1600-160,000	835-11,490
Baier [6]	BL/Weakly non-lin.	1.65	2/3	1/3	-	-	-	$\gg 1$
Baier [6]	CFD/BL	1.1	0.46	1/3	0.143,0.286,0.429	0	130-1600	$\gg 1$

Table 2.9: Summary of the experimental observations and the CFD (FLUENT)/boundary layer theory predictions for the radial mass transfer in one fluid Taylor-Couette flow.

Axial Dispersion in One Fluid Taylor-Couette Flow. Many researchers have also investigated the axial mass transport (or axial dispersion) in Taylor-Couette flow. The experimental observations for one fluid Taylor-Couette flow indicate that axial dispersion decreases to a minimum near the onset of Taylor vortices and increases as the Taylor number increases [90]. When axial flow is absent, the dispersion is proportional to the square root of the diffusion coefficient [25], but when axial flow is present, the dispersion is independent of the diffusion coefficient [39, 83] and increases with increasing axial flow rates [32, 83]. These experimental results are modeled as one dimensional convection-diffusion plug flow [32, 83, 105] or as a mixing-tanks-in-series system [63, 71]. One research group has combined the plug flow and mixing tank models into a single overall model correlating the axial mass transfer to the position in the vortex [24]. Convection dominates near the vortex boundaries and diffusion dominates near the vortex center [24]. The results from the previous experimental studies are summarized in Table 2.11.

The corresponding theoretical work for predicting axial dispersion in one fluid Taylor Couette flow has included asymptotic and full numerical analyses. Rosenbluth *et. al* present results for axisymmetric Taylor-Couette flow without axial flow in an infinite annulus in both the high and low Peclet number limits [94]. The Peclet number is a measure of convective transport to diffusive transport and is defined as $Pe = ud/D = Re_\theta Sc$, where u is the characteristic flow velocity in a convective cell. When $Pe \ll 1$, the vortex has nearly uniform composition. In this case, Rosenbluth *et. al* find that $D^* \propto DPe^2$ or that axial dispersion increases as the flow velocity of the cell increases, but decreases as the diffusion coefficient increases. This is the same form as for Taylor-Aris convective dispersion [5, 107]. When $Pe \gg 1$, the effect of diffusion is small and boundary layers form along the vortex boundaries with little diffusion into the interior of the cell. This is the limit that is typically observed experimentally. Rosenbluth *et. al* find that $D^* = cDPe^{1/2} = c(Dud)^{1/2}$ or that axial dispersion increases as either the diffusion coefficient increases or the flow velocity of the cell (i.e. aziumthal Reynolds number) increases. The constant, c, depends on the system geometry and the flow velocity at the cell boundary. The dependence of the dispersion coefficient on the square root of the Peclet number reflects the existence of mass transfer boundary layers at the cell boundaries. Boundary layer theory is further discussed in section 5. From a weakly non-linear stability analysis [21], $u \propto Re_\theta$, which leads to the boundary layer theory relation $D^* \propto Re_\theta(Sc)^{1/2}$. This equation compares favorably with the experimental observations $D^* \propto Re_\theta^a$ where typically $0.69 < a < 1.05$. The agreement between the experiment and theory is somewhat surprising since the weakly non-linear analysis is strictly valid only near the onset of the vortex flow, whereas the experiments were generally in the turbulent vortex regime. At these higher Reynolds numbers, a numerical solution for the interface velocity should be used in the boundary layer equations instead of the weakly non-linear analysis result. The computational fluid dynamics package FLUENT was used to calculate the flow field to be used in combination with boundary layer theory to calculate the dispersion coefficient for $Re_\theta/Re_{\theta,c} \leq 10$. The boundary layer/FLUENT results are summarized in Table 2.10. The calculated axial dispersion coefficient is described by the relation $D^* \propto Re_\theta^{0.69}$, again agreeing with the experimental observations. However, the actual values of the predicted dispersion coefficient are an order of magnitude lower than observed values. Moore and Cooney also observed a large discrepancy when comparing their experimental results with Rosenbluth's prediction [83]. The experiments included axial flow, while the boundary layer/CFD theory and Rosenbluth's analysis did not and this discrepancy indicates the importance of convective transport.

$Re_\theta/Re_{\theta,c}$	D^*, cm^2/s
1.4	0.0008
2.8	0.0015
5.6	0.0024
8.3	0.003
11.5	0.0036

Table 2.10: Axial dispersion in Taylor-Couette flow as calculated by CFD (FLUENT)/boundary layer theory. $R_1 = 4$ cm, $d = 1$ cm, $\nu = 0.01$ cm^2/s, $Sc = 1000$.

Axial flow complicates the theoretical analysis of axial dispersion in Taylor-Couette flow. In Taylor-Couette flow with axial flow, some streamlines (in a reference frame moving with the wavespeed) bypass the vortices and the wavespeed is higher than the mean axial flow velocity, $\bar{W}$ (Chandrasekhar, 1961, Howes and Rudman, 1998). To calculate the long-time dispersion coefficient, Howes and Rudman use the method of moments developed by Brenner (1980). They assume that the dispersion can be described by two terms: (1) the vortex boundary transport where $D^* \propto D^{1/2}$, and (2) the axial transport due to axial flow where $D^* \propto \bar{W}^2 d^2/D$. Experimentally, increasing the axial flow rate does augment the axial dispersion, but with a weaker dependence than predicted here. This discrepancy may be a result of the assumptions of long-time and axisymmetry in the theoretical analysis of Howes and Rudman (1998). They did not study the effect of azimuthal Reynolds number on the axial dispersion.

In summary, although the qualitative trends are consistently observed and predicted, the quantitative dependence of dispersion on the azimuthal Reynolds number and axial Reynolds number varies widely. Several factors may contribute to these discrepancies:

- Do the results depend on the method of tracer introduction, such as direct injection into the annulus versus into the feed stream?

Research Group	R_1/R_2	Gap (cm)	$Re_\theta/Re_\theta^{crit}$	Re_{ax}	Model	D^*	Range Obs. (cm^2/s)
Enokida [32]	0.593 - 0.760	1.80 - 3.05	50-1000	60-250	1D disp.-conv.	$D^* \propto C_1 Re_\theta^{0.81}$ $+C_2 Re_\theta Re_z$	0.1-0.6
Moore [83]	0.73 - 0.96	0.04-0.38	4-200	0.5 - 30	1D disp.-conv.	$D^* \propto Re_\theta^{1.05} Re_z^{0.17}$	0.01 - 10
Kataoka [62]	0.75	1	0 - 27	0-90	PFR in lam. vortex regime	–	
Tam [105]	0.494-0.875	0.32-1.285	50-1000	0	1D disp.-conv.	$D^* \propto Re_\theta^{\beta}$ $\beta = 0.69 - 0.86$ $\beta_{thry} = 1.$	0.8 - 2.7
Kataoka [63]	0.6	2	4 - 12	0 -35	tanks-in-series	$D^* \propto Re_\theta^{0} Re_z^{1.7}$	0.06- 0.70
Desmet [24]	0.64	2.4	1 - 700	0	2 model	–	–
Pudijiono [90]	0.94	0.15	0 - 3	0.03 - 5.5	1D disp.-conv.	–	$\approx$ 0.001-2.4
Ohmura [86]	0.70	1.84	12-50	0	1D disp.-conv.	$D^* \propto Re_\theta^{2.8}$ - Lam. $D^* \propto Re_\theta^{1.5}$ - Wavy $D^* \propto Re_\theta^{0.9}$ - Turb.	0.1 - 1

Table 2.11: Experimental correlations for axial dispersion in one fluid Taylor-Couette flow.

- Does tracer injection into the annulus affect the flow pattern or preferentially select the vortex center where more diffusion time may be required to reach the vortex boundary?
- Does the number of vortices in the annulus vary? Does this affect fixed measurement points that should always measure the same part of the vortex?
- How much do end effects contribute?
- and, How important is the long time assumption?

Applications of Taylor-Couette Flow. Taylor-Couette flow has found several applications which include a filtration device that uses the vortices to reduce concentration polarization [46, 82, 84], a reactor with one cylinder supporting the catalyst [17, 45, 53], a reactor exploiting the plug flow properties of Taylor-Couette flow [17, 55], a rotating cylinder electrode [70], and countercurrent liquid-liquid extraction with the two phases emulsified [22, 75].

By far the most commercialized application has been the filtration unit, developed by MBR-Sulzer as a Dynamic Bio Pressure Filter and by Membrex as the Benchmark Vortex Flow Filtration System [83]. The MBR-Sulzer device is shown in Figure 2.21. The filter is based on one fluid Taylor-Couette flow with a small imposed axial flow. The inner cylinder is porous allowing a small radial flow of filtrate to pass. The advantages of Taylor-Couette flow in filtration are (1) The vortex motion of the Taylor vortices is continuously “sweeping” the filter surface to prevent the buildup of materials that may clog or foul the filter surface and (2) The axial and transmembrane pressure drops are decoupled. Increased filter performance of up to three times over crossflow filtration has been achieved [67, 68, 116]; however, the capital equipment and operation can be costly.

Min and Lueptow investigated the fluid mechanics of Taylor-Couette filtration and found that in addition to the axial flow effects, strong outward or inward radial flow stabilizes the flow; whereas weak radial outflow destabilizes the flow. In addition, the vortex positions are shifted in the direction of the radial flow. In all cases, the transition to higher modes of instability are stabilized and some helical waveforms are prevented altogether [82].

Taylor-Couette flow has also been evaluated as a means to improve reactor performance. Model systems investigated include partial oxidation of isopropanol [17], acetone to ketene conversion [17], and culturing of bioproducts [55]. With a reactant or catalyst on or supplied through one of the cylinder walls, the concentration, temperature, and residence time of the various species may be better controlled. When used as an axial reactor, nearly ideal plug flow may be achieved with the reacting and flowing directions decoupled. This

Figure 2.21: The MBR-Sulzer Taylor-Couette filtration system.

provides the potential for the conversion rate through the reactor to be independent of the production rate. The increase in reactor performance may be as high as 100% in the Taylor-Couette region over the Couette flow region [17]. For bioreactors, Taylor-Couette flow may be especially beneficial as lower oxygen sparge rates are required than with other types of reactors. High sparge rates are damaging since they reduce culture growth and form disruptive crust layers [55]. The preliminary studies for a bioreactor were promising, but apparently not pursued.

Countercurrent liquid-liquid extraction using Taylor-Couette flow has also been evaluated and has reportedly been used as a laboratory separation device for over 50 years [75]. The principle is for a heavy liquid to flow cocurrently or countercurrently with a light fluid in an annulus. The inner cylinder rotation rate is high enough to emulsify the two fluids and to form Taylor vortices of the emulsion. The emulsion produces a high mass transfer surface area between the two phases. The axial flow provides continuous contacting and the Taylor vortices reduce axial dispersion. Again the extraction efficiency and the total flow rate through the reactor can be decoupled and separately controlled by the cylinder rotation rate and the axial flow rate. This type of liquid-liquid extraction is particularly effective for two fluid phases that easily de-emulsify at the exit ports and for sensitive or hazardous materials that require high efficiencies. The control parameters to optimize the extraction efficiency include the volume ratio of the two phases, the rotation rate, the axial flow rate, the feed nozzle design to facilitate droplet formation, and the extractor geometry [22, 100, 109]. This type of extractor is similar to the Argonne National Laboratories (ANL) and Savannah River Laboratories (SRL) extractors discussed in section 2.2.

Other Centrifugal Instabilities. Other types of centrifugal instabilities, similar in origin to Taylor-Couette flow, result from flow through a curved channel (Dean flow) or flow in a concave wall boundary layer (Görtler flow). Similar vortices develop and have also been advanced as less expensive alternatives to the Taylor-Couette applications, particularly in filtration. Dean vortices continuously "sweep" the membrane surface and thereby reduce foulant buildup. Belfort and coworkers designed a filtration system utilizing curved channel Poiseuille flow with a flow rate above the critical one required for the Dean instability [11]. For a given wall flux through the filter, they optimize the filter system curvature to continuously balance the stabilizing effect of the wall flux against the destabilizing effect of increasing curvature. The channel curvature increases with distance down the filter and the system is not limited to narrow gap designs. Belfort reports increased filtration performance, up to 30-500%, in the presence of Dean vortices [15, 116]. Figure 2.22 is a schematic of filtration utilizing Dean vortices [116].

Figure 2.22: Schematic of filtration utilizing Dean vortices [116]

2.4 Two-Fluid Taylor-Couette Flow

To achieve two-fluid Taylor-Couette flow, the odd solution (previously illustrated in Figure 2.14) of the one fluid Taylor-Couette flow can be exploited. The odd solution has two identical layers of Taylor vortices filling the annular gap. Although the odd solution is never observed experimentally, it suggests that two-fluid Taylor-Couette flow is possible. The liquid interface introduces six additional boundary conditions: matching velocities and shear stresses at the interface and the normal stress balanced by surface tension. In addition, the interface position is unknown. These interfacial boundary conditions require that vortex motion in one phase be balanced by vortex motion in the other phase. High rotation rates are required to first centrifugally stratify the two fluids, and then a subsequent increase in the inner cylinder rotation rate produces vortices. Alternatively, a very viscous fluid or fluids physically attracted to their respective cylinder wall may eliminate the requirement for stratification by centrifugal force [57]. The experimental apparatus is horizontal, unlike the vast majority of one fluid vertical systems, to prevent the axial separation of the two fluids. The dimensionless groups to describe two-fluid Taylor-Couette flow are: a Taylor (or Reynolds) number for each phase, a Froude number for gravitational effects in each phase, Joseph's J factor for interface stability (discussed below), and viscosity, density, and radii ratios to describe the fluid layers.

The work that has been done on two fluid Couette flow, the base flow for two-fluid Taylor-Couette flow, is very limited and most consider only inner cylinder rotation where emulsion is a likely outcome. Motivated by gaseous core nuclear rockets, Schneyer reports a linear stability analysis of two incompressible, immiscible stratified fluids [97]. Schneyer limits his analysis to stably stratified fluids (heavy fluid at the periphery), a stationary outer cylinder, and negligible surface tension and gravitational effects. He finds two eigenvalues, one a result of the Taylor instability and another of the Kelvin-Helmholtz viscous stratification instability [97].

Based on an energy analysis neglecting gravity, Joseph predicts a linearly stable rigid interface between the two fluids at rigid rotation when $J > 1$ and a globally stable rigid interface when $J > 4$ [57]. The dimensionless group J is a measure of centrifugal to surface tension forces: $J = (\rho_2 - \rho_1)\Omega^2 R_i^3/S$, where S is the interfacial tension, ρ_1 is the density of the inner fluid, Ω is the rigid body rotation rate, and R_i is the interface position [57]. For the conditions required in a Taylor-Couette liquid extractor, $J \gg 4$.

Renardy and Joseph theoretically explored the stability of two fluid Couette flow with only inner cylinder rotation [93]. They expand the disturbance velocities and pressure in Chebyshev polynomials and numerically solve the linear eigenvalue problem for the growth rate of Taylor vortices. Their results are primarily for the one fluid Taylor-Couette axial wavenumber, which is probably not the critical wavenumber. They find: (1) A thin layer of less viscous fluid near either cylinder is linearly stable. This does not agree with the theory that viscous dissipation should be minimized. (2) Two-fluid Taylor-Couette flow may be stabilized (destabilized) by the less (more) viscous fluid in a lubrication layer near the inner cylinder. (3) The denser fluid may be located at the inner cylinder when stabilized by surface tension and a favorable viscosity difference.

In their corresponding experimental work, Joseph and coworkers report several modes for two fluid Couette flow [56, 58]. The experimental apparatus is horizontal with sealed ends and only inner cylinder rotation. The fluids investigated are viscous oils (silicone, STP, SAE40, vegetable) and water, or two viscous oils. With only inner cylinder rotation, they measure the torque as a function of rotation rate and identify changes in the fluid flow modes. The fluid regimes observed include (1) an emulsion undergoing one fluid Taylor-Couette flow, (2) rollers of oil and vortex motion of the water phase, and (3) an emulsion in bands separated by pure fluid. Rollers are defined as axisymmetric blobs attached to the inner cylinder. Banded flow is the large amplitude limit of rollers, where the interface breaks through to touch both cylinders. Campero and Vigil observed similar patterns in their experiments [12].

Toya and Nakamura studied Taylor-Couette flow of two fluids in a vertical annulus; the fluids are axially stratified. They observe that at the interface, the bottom vortex in the less dense phase can co-rotate with the top vortex in the denser phase; the flow is countercurrent at the boundary between the two fluids [110].

In addition to the Taylor-Couette instability in two fluid Couette flow, several studies have investigated the shear instabilibity due to fluid layers with different viscosities. Gallagher *et. al* observed azimuthal waves in a vertical Couette cell filled with two radially stratified fluids of matched density, but different viscosity [36]. Only the outer cylinder was rotated to avoid the Taylor-Couette instability. The experimentally observed wavelength and onset of the instability agree well with the linearized theory as represented by the Orr-Sommerfield equation for viscous shear flows of two fluids.

Chapter 3

Stability of Two-Layer Couette Flow: Theory

3.1 Formulation

As in the standard one fluid problem, a linear stability analysis for two-fluid Taylor-Couette flow explains the experimental observations. The equations of motion and continuity are first solved for the base flows: Couette flow, which has only an azimuthal velocity component and countercurrent axial flow, which has only an axial component. A form for the disturbance flow is then assumed and the equations of motion and continuity are solved for the total flow pattern. In general, an analytical solution is impossible, so either simplifying assumptions or a full numerical analysis is required. A simple inviscid analysis without countercurrent axial flow is first presented, followed by more detailed viscous linear stability analyses which can include countercurrent flow.

3.1.1 Base Velocities

The geometry for two-fluid Taylor-Couette flow is a pair of coaxial cylinders of infinite length. The outer cylinder with radius R_2 rotates with an angular velocity of Ω_2. The outer (denser) fluid contacts only the outer cylinder and has density ρ_2, kinematic viscosity ν_2, and dynamic viscosity $\mu_2 = \nu_2\rho_2$. The flow field for the outer fluid is represented by V_2 for the base state Couette flow and W_2 for the base state axial flow. The total base flow is then described by $\mathbf{V_2} = V_2(r)e_\theta + W_2(r)e_z$. The inner fluid is described similarly, but with subscripts 2 replaced with 1. The interfacial tension between the two fluids is represented by S. The undisturbed flat interface between the two fluids is located at R_i and rotates with an angular velocity of Ω_i. As high rotation rates are required for two-fluid Taylor-Couette flow, gravity is neglected in the following analyses. The velocities are scaled with $\Omega_1 R_1$, time with d^2/ν_1, pressure with $2\Omega_1^2 R_1^2 \rho_1/\epsilon$, and spatial variables with $d = R_2 - R_1$. The narrow gap parameter is $\epsilon = d/R_2$. The importance of interfacial tension is measured by the quantity $J_2 = (\rho_2 - \rho_1)\Omega_2^2 R_2^3/S$, which is slightly modified from Joseph's J since his is for rigid rotation [58]. The radial direction, r, is transformed into a new variable, $y = (r - R_1)/d$, which has a value of zero at the inner cylinder and one at the outer cylinder.

Since the axial counterflow is driven by the axial pressure drop for the respective phase, the interface is slightly tapered rather than cylindrical. A perturbation analysis of the normal stress boundary condition, neglected surface tension, reveals that at rigid rotation the taper is approximately determined by,

$$\Delta P = \left(\frac{(\rho_2 - \rho_1) g_{\text{eff}} \delta}{L} + (\frac{\partial P_2}{\partial z} - \frac{\partial P_1}{\partial z}) \right) = 0,$$

where $g_{\text{eff}} = \Omega_2^2 R_2$ and $\delta + R_i$ is the maximum radius of the tapered interface. The maximum taper is then

$$\frac{\delta}{d} = \frac{4\Gamma R_{12} Re_{ax,2} Ek_2^2}{(1 - \rho_{12})} \left(\frac{\mu_{12}^2}{\rho_{12}} \frac{Re_{ax,1}}{Re_{ax,2}} + 1 \right),$$

where $\Gamma = Z/R_1$ is the aspect ratio, Z is the extractor length, $R_{12} = R_1/R_2$, $Re_{ax,j} = \bar{W}_j d/\nu_j$, $Ek_j = \frac{\mu_j}{2\rho_j \Omega_2 d^2}$ is the Ekman number, $\mu_{12} = \mu_1/\mu_2$ and $\rho_{12} = \rho_1/\rho_2$. The taper increases with increasing axial flow or an increasing difference in the flow rates, but decreases with increasing centrifugal force or increasing density difference. When δ is small, the solutions below that assume a cylindrical interface at y_i are good approximations. For the results presented here, $\delta/d < 0.03$ with $\Gamma = 6$.

The azimuthal component of the base flow is two-fluid Couette flow with the standard boundary conditions of no-slip at the cylinder walls, and continuity of the velocity and shear stress at the interface:

$$\begin{array}{ll} y=1 & V_2=\Omega_{21}R_{21} \\ y=0 & V_1=1 \\ y=y_i & V_2=V_1 \\ & \tau_{r\theta,2}=\tau_{r\theta,1}. \end{array}$$

The resulting solution has only an azimuthal velocity component for each phase $(j=1,2)$:

$$V_j = A_j(y+\frac{R_{12}}{\epsilon}) + \frac{B_j}{(y+\frac{R_{12}}{\epsilon})}, \tag{3.1}$$

where

$$A_1 = \frac{\epsilon}{R_{12}} - \frac{\mu_{21}(\Omega_{21}-1)\epsilon/R_{12}}{R_{12}^2-\mu_{21}+R_{1i}^2(\mu_{21}-1)} = \frac{(R_{1i}^2-\Omega_{i1})\epsilon/R_{12}}{R_{1i}^2-1},$$

$$B_1 = \frac{\mu_{21}(\Omega_{21}-1)R_{12}/\epsilon}{R_{12}^2-\mu_{21}+(\mu_{21}-1)R_{1i}^2} = \frac{(\Omega_{i1}-1)R_{12}/\epsilon}{R_{1i}-1},$$

$$A_2 = \Omega_{21}\frac{\epsilon}{R_{12}} - \frac{(\Omega_{21}-1)\epsilon/R_{12}}{1-\mu_{21}R_{21}^2+R_{2i}^2(\mu_{21}-1)} = \frac{\Omega_{i1}(R_{i2}^2-\Omega_{2i})\epsilon/R_{12}}{R_{i2}-1},$$

$$B_2 = \frac{1}{\mu_{21}}B_1 = \frac{\Omega_{i1}R_{i1}^2(\Omega_{2i}-1)R_{12}/\epsilon}{R_{i2}-1},$$

and Ω_i is determined by the first form of the Couette solution (equation 3.1). Here, $R_{1i}=R_1/R_i$, $\Omega_{21}=\Omega_2/\Omega_1$, etc.

The countercurrent axial base flow is also determined by the usual boundary conditions of no-slip at the cylinder walls and continuity of velocity and shear stress at the interface:

$$y = 1 \qquad W_2 = 0$$

$$y = 0 \qquad W_1 = 0$$

$$y = y_i \qquad W_2 = W_1$$

$$\tau_{rz,2} = \tau_{rz,1}.$$

The resulting solution has only an axial velocity component for each phase ($j = 1, 2$):

$$W_j = F_j(y + \frac{R_{12}}{\epsilon})^2 + G_j \ln(y + \frac{R_{12}}{\epsilon}) + H_j, \tag{3.2}$$

where

$$F_1 = \frac{\Delta P_{z,1}}{4\Gamma\Omega_{21} E k_1 \epsilon}$$

$$F_2 = \frac{\Delta P_{z,2}}{4\Gamma\Omega_{21} E k_2 \epsilon \mu_{21}}$$

$$G_1 = -2(\frac{R_{12}}{\epsilon} + y_i)^2 (F_1 - \mu_{21} F_2) + \mu_{21} G_2$$

$$H_1 = -F_1 \left(\frac{R_{12}}{\epsilon}\right)^2 - G_1 \ln(\frac{R_{12}}{\epsilon})$$

$$G_2 = -\frac{[(F_1 - F_2)(\frac{R_{12}}{\epsilon} + y_i)^2 - F_1(\frac{R_{12}}{\epsilon})^2 + F_2(1 + \frac{R_{12}}{\epsilon})^2 - 2(F_1 - \mu_{21} F_2)(\frac{R_{12}}{\epsilon} + y_i)^2 [\ln(\frac{R_{12}}{\epsilon} + y_i) - \ln(\frac{R_{12}}{\epsilon})]]}{\ln(1 + \frac{R_{12}}{\epsilon}) + (\mu_{21} - 1)\ln(\frac{R_{12}}{\epsilon} + y_i) - \mu_{21}\ln(\frac{R_{12}}{\epsilon})}$$

$$H_2 = -F_2(1 + \frac{R_{12}}{\epsilon})^2 - G_2 \ln(1 + \frac{R_{12}}{\epsilon}).$$

The axial pressure drops, $\Delta P_{z,1}$ and $\Delta P_{z,2}$ are determined by the volumetric flowrates.

A typical velocity profile for countercurrent axial flow is shown in Figure 3.1. The axial velocity at the interface is generally non-zero and backflow in one of the fluid phases results. Furthermore, Rayleigh's theorem for inviscid flow profiles with inflection points suggests that the flow could be unstable at sufficiently high axial Reynolds numbers [30].

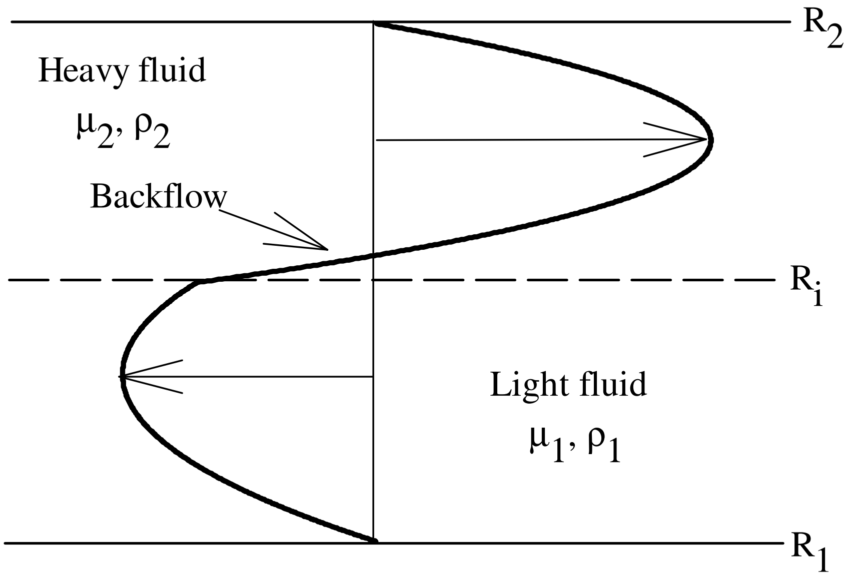

Figure 3.1: Velocity profile for the countercurrent axial base flow. Here $R_{12} = 0.826$, $R_2 = 5.05$, $\epsilon = 0.174$, $Q_1 = Q_2$, $\mu_{21} = 0.22$, and $y_i = 0.5$.

3.1.2 Linear Stability Analysis

In the linear stability analysis, small disturbance velocities are added to the base flow solution. These velocities are solved for using the equations of motion and continuity with the corresponding boundary conditions. The total flow is then described by $\mathbf{V}_j = \begin{pmatrix} \hat{v}_{r,j} \\ \hat{v}_{\theta,j} + V_j \\ \hat{v}_{z,j} + W_j \end{pmatrix}$. The boundary conditions require no-slip at the cylinder walls, mathcing velocity components and shear stresses in the two phases at the interface, and the normal stress to be balanced by surface tension at the interface. The disturbance flow is assumed to have the following normal mode form:

$$\hat{\mathbf{v}}_j = \begin{pmatrix} v_{r,j}(y) \\ v_{\theta,j}(y) \\ v_{z,j}(y) \end{pmatrix} e^{i\alpha(z-ct)+in\theta} + c.c. \tag{3.3}$$

The interface deforms from y_i as $\hat{h} = he^{i\alpha(z-ct)+in\theta} +$ its complex conjugate. Pressure also has the form $\hat{p} = p(y)e^{i\alpha(z-ct)+in\theta} + c.c.$ In addition to the boundary conditions, the kinematic condition requires that particles on the interface move with the interface $\frac{D}{Dt}(y - \hat{h} - y_i) = 0$, where $\hat{h} + y_i$ is the perturbed interface and the substantial derivative operator $\frac{D}{Dt} = \frac{\partial}{\partial t} + \mathbf{V} \cdot \nabla$.

The resulting equations from the boundary conditions and the equations of continuity and momentum are linearized by eliminating terms containing the products of the disturbance quantities. Domain perturbation is used to apply the interfacial boundary conditions at the unperturbed interface position, y_i, rather than at the actual unknown interface position.

The linearized governing equations are for:

Radial momentum:

$$[-i\alpha c - \mu_{j1}\rho_{1j}(\tfrac{\partial^2}{\partial y^2} + \tfrac{1}{(y+R_{12}/\epsilon)}\tfrac{\partial}{\partial y} - \tfrac{(1+n^2)}{(y+R_{12}/\epsilon)^2} - \alpha^2) + in\tfrac{R_{12}}{2Ek_1\Omega_{21}\epsilon}\tfrac{V_j}{(y+R_{12}/\epsilon)} +$$

$$i\alpha\tfrac{R_{12}}{2Ek_1\Omega_{21}\epsilon}W_j]v_{r,j} + [-2\tfrac{R_{12}}{2Ek_1\Omega_{21}\epsilon}\tfrac{V_j}{(y+R_{12}/\epsilon)} + \mu_{j1}\rho_{1j}\tfrac{2in}{(y+R_{12}/\epsilon)^2}]v_{\theta,j}$$

$$+\rho_{1j}\tfrac{2}{\epsilon}\tfrac{R_{12}}{2Ek_1\Omega_{21}\epsilon}\tfrac{\partial p_j}{\partial y} = 0$$

Azimuthal momentum:

$$[-i\alpha c - \mu_{j1}\rho_{1j}(\tfrac{\partial^2}{\partial y^2} + \tfrac{1}{(y+R_{12}/\epsilon)}\tfrac{\partial}{\partial y} - \tfrac{(1+n^2)}{(y+R_{12}/\epsilon)^2} - \alpha^2) + in\tfrac{R_{12}}{2Ek_1\Omega_{21}\epsilon}\tfrac{V_j}{(y+R_{12}/\epsilon)} +$$

$$i\alpha\tfrac{R_{12}}{2Ek_1\Omega_{21}\epsilon}W_j]v_{\theta,j} + [2A_j\tfrac{R_{12}}{2Ek_1\Omega_{21}\epsilon} - \mu_{j1}\rho_{1j}\tfrac{2in}{(y+R_{12}/\epsilon)^2}]v_{r,j}$$

$$+in\rho_{1j}\tfrac{2}{\epsilon(y+R_{12}/\epsilon)}\tfrac{R_{12}}{2Ek_1\Omega_{21}\epsilon}p_j = 0$$

Axial momentum:

$$[-i\alpha c - \mu_{j1}\rho_{1j}(\tfrac{\partial^2}{\partial y^2} + \tfrac{1}{(y+R_{12}/\epsilon)}\tfrac{\partial}{\partial y} - \tfrac{n^2}{(y+R_{12}/\epsilon)^2} - \alpha^2) + in\tfrac{R_{12}}{2Ek_1\Omega_{21}\epsilon}\tfrac{V_j}{(y+R_{12}/\epsilon)} +$$

$$i\alpha\tfrac{R_{12}}{2Ek_1\Omega_{21}\epsilon}W_j]v_{z,j} + \tfrac{R_{12}}{2Ek_1\Omega_{21}\epsilon}\tfrac{\partial W_j}{\partial y}v_{r,j}$$

$$+i\alpha\rho_{1j}\tfrac{2}{\epsilon}\tfrac{R_{12}}{2Ek_1\Omega_{21}\epsilon}p_j = 0$$

Continuity:

$$\frac{v_{r,j}}{(y+R_{12}/\epsilon)} + \frac{\partial v_{r,j}}{\partial y} + \frac{in}{(y+R_{12}/\epsilon)}v_{\theta,j} + i\alpha v_{z,j} = 0.$$

The linearized interfacial boundary conditions require that at $y = y_i$:

$$v_{r,1} = v_{r,2}$$

$$v_{\theta,1} - v_{\theta,2} - h[\tfrac{2(B_1 - B_2)}{(y + \frac{R_{12}}{\epsilon})^2}] = 0$$

$$v_{z,1} - v_{z,2} + h[2(y + \tfrac{R_{12}}{\epsilon})(F_1 - F_2) + \tfrac{(G_1 - G_2)}{(y + \frac{R_{12}}{\epsilon})}] = 0$$

$$\tfrac{\partial v_{z,1}}{\partial y} - \mu_{21}\tfrac{\partial v_{z,1}}{\partial y} + i\alpha(1 - \mu_{21})v_{r,2} + h[2(F_1 - \mu_{21}F_2) - \tfrac{(G_1 - \mu_{21}G_2)}{(y + \frac{R_{12}}{\epsilon})^2}] = 0$$

$$\tfrac{\partial v_{\theta,1}}{\partial y} - \tfrac{v_{\theta,1}}{(y + \frac{R_{12}}{\epsilon})} - \mu_{21}\tfrac{\partial v_{\theta,2}}{\partial y} + \mu_{21}\tfrac{v_{\theta,2}}{(y + \frac{R_{12}}{\epsilon})} + \tfrac{in(1 - \mu_{21})}{(y + \frac{R_{12}}{\epsilon})}v_{r,2} = 0$$

$$\tfrac{1}{1 - \rho_{21}}[(p_1 - p_2)(1 - \epsilon) - 2\Omega_{21}Ek_1\epsilon^2(\tfrac{\partial v_{r,1}}{\partial y} - \mu_{21}\tfrac{\partial v_{r,2}}{\partial y})]$$
$$+h[\tfrac{d}{2R_i}(1 - \epsilon)\epsilon V_2^2 - \tfrac{\Omega_{21}}{4Ek_1J_2\epsilon}(\alpha^2 - \left(\tfrac{d}{R_i}\right)^2(1 - n^2))] = 0$$

with the linearized kinematic condition $h(\frac{-i\alpha c}{Re_1} + \frac{d}{R_i}inV_2 + i\alpha W_2) = v_{r,2}$.

3.2 Results.

3.2.1 Inviscid Analysis.

In the inviscid analysis for two-fluid Taylor-Couette flow without countercurrent flow, each fluid layer is considered inviscid but with the base Couette flow velocity profile. So although this is an inviscid analysis, the viscosity *ratio* remains important because it determines the velocity profile. Each phase is subject to a Rayleigh criterion similar to the one fluid problem; the inner fluid is unstable when $\Omega_{i1} < R_{1i}^2$ and the outer fluid is unstable when $\Omega_{2i} < R_{i2}^2$. Since the rotation rate of the interface is known from the base flow solution, $\Omega_i = V_1/R_i = V_2/R_i$, these Rayleigh criteria can be expressed in experimentally controllable quantities. The instability occurs in the inner fluid when

$$\Omega_{21} < \Omega_{21,c,1} = \frac{R_{12}^2 + (\mu_{21} - 1)R_{1i}^2}{\mu_{21}}$$

and in the outer fluid when

$$\Omega_{21} < \Omega_{21,c,2} = \frac{R_{12}^2}{\mu_{21} - (\mu_{21} - 1)R_{1i}^2}.$$

As $\mu_{21} \to \infty$, fluid 2 is stable and fluid 1 obeys a single fluid criterion based on R_{1i}. As $\mu_{21} \to 0$, fluid 1 is stable and fluid 2 obeys the criterion based on R_{i2}. When $\mu_{21} = 1$ both expressions reduce to the expression for a single fluid. This is the only point where the $\Omega_{21,c,j}$ vs. μ_{21} curves cross; thus a necessary but not sufficient criterion for both phases to be "Rayleigh unstable" is for the single fluid problem in the same geometry to be Rayleigh unstable. For a given interface position, increasing μ_{21} stabilizes the outer fluid (in the sense that Ω_{21} for instability decreases) and destabilizes the inner fluid. Additionally, since for $\mu_{21} > 1, \Omega_{21c,2} < \Omega_{21c,1}$ and vice versa when $\mu_{21} < 1$, the less viscous fluid is always more susceptible to instability. As shown in Figure 3.2 the Rayleigh curves always cross at $\mu_{21} = 1$, but moving the interface away from equal fluid depths, shifts and expands the region where both fluids are unstable.

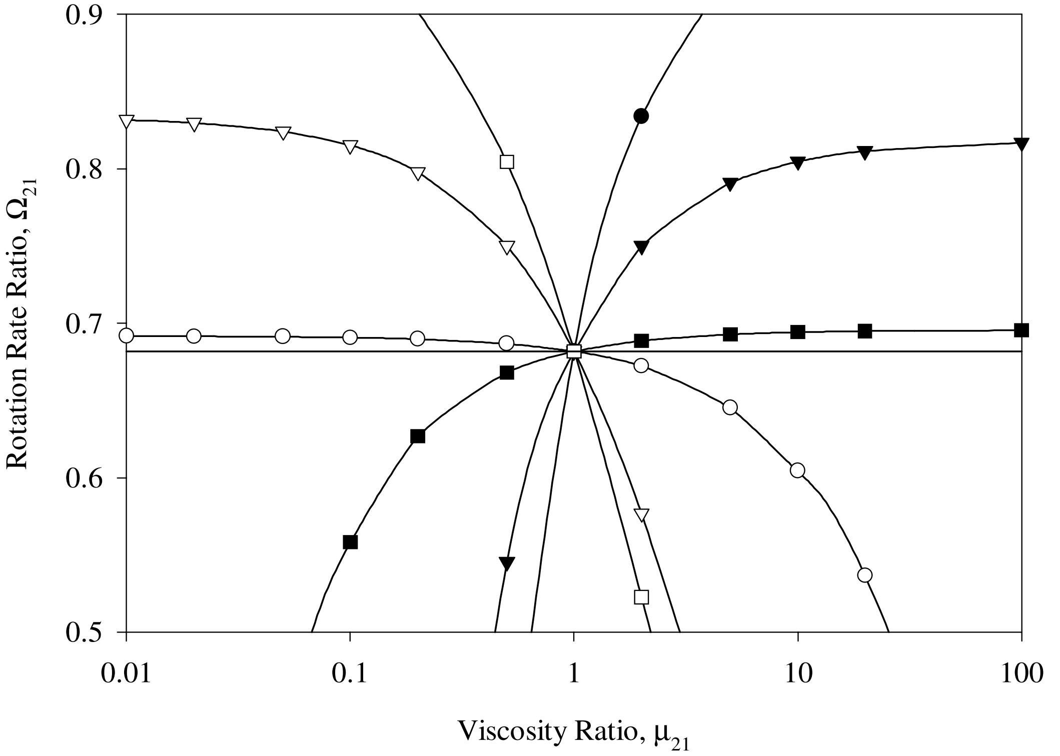

Figure 3.2: The Rayleigh criteria for two-fluid Taylor-Couette flow for $R_{12} = 0.826$ and $R_2 = 5.05$ cm. The Rayleigh criterion for one fluid Taylor-Couette flow is represented by the line without symbols. The lines with hollow (filled) symbols represent the Rayleigh criterion for the outer (inner) fluid. The circles (◯) correspond to the interface near the inner cylinder ($y_i = 0.03$); the triangles (▽) correspond to the interface in the center ($y_i = 0.5$); and the squares (□) correspond to the interface near the outer cylinder ($y_i = 0.94$).

3.2.2 Viscous Analysis without Counterflow.

When countercurrent axial flow is absent, two-fluid Taylor-Couette flow can be approached with the same method as in the one fluid problem. The equations and boundary conditions are simplified by assuming that the flow is axisymmetric at onset ($n = 0$), the gap is narrow compared to the cylinder radii ($d/R_2 \to 0$), and the bifurcation occurs near rigid rotation ($\Omega_2/\Omega_1 \to 1$). These assumptions are consistent with the experimental observations for two-fluid Taylor-Couette flow (Figure 6.13). When the equations of momentum and continuity are combined to eliminate explicitly the radial and axial velocity components and the pressure, the resulting differential equations are:

$$\begin{aligned} (D^2 - \alpha^2 + i\alpha c)^2 (D^2 - \alpha^2) v_{\theta,1} &= -\alpha^2 T_1 v_{\theta,1}, \quad 0 < y < y_i \\ (D^2 - \alpha^2 + i\alpha \mu_{12} \rho_{21} c)^2 (D^2 - \alpha^2) v_{\theta,2} &= -\alpha^2 T_2 v_{\theta,2}, \quad y_i < y < 1 \end{aligned}$$

where

$$D = \partial/\partial y,$$

$$T_1 = \frac{-4A_1\Omega_1 d^4}{\nu_1^2} = -\frac{4\Omega_1^2 d^4 [R_{1i}^2 - \Omega_{i1}]}{\nu_1^2 (R_{1i}^2 - 1)} = \frac{[R_{1i}^2 - \Omega_{i1}]}{1 - R_{1i}^2} \frac{\Omega_{12}^2}{Ek_1^2}$$

and

$$T_2 = \frac{-4A_2\Omega_i d^4}{\nu_2^2} = -\frac{4\Omega_i^2 d^4 [R_{i2}^2 - \Omega_{2i}]}{\nu_2^2 (R_{i2}^2 - 1)} = \frac{[R_{i2}^2 - \Omega_{2i}]}{1 - R_{i2}^2} \frac{\Omega_{i2}^2}{Ek_2^2}.$$

The terms in the square brackets in these definitions of Taylor numbers are the Rayleigh criteria that determine the stability for the inviscid case, as discussed above. The other velocity components can be found from the relations

$$v_{r,j} = Ek_j(D^2 - \alpha^2 + i\alpha\mu_{1i}\rho_{j1}c)v_{\theta,j}$$

$$v_{z,j} = -\frac{1}{i\alpha}Dv_{r,j}.$$

After using the linearized kinematic boundary condition

$$i\alpha ch + Re_1 v_r = 0,$$

the boundary conditions become:

$y = 0 \quad v_{r,1} = v_{\theta,1} = v_{z,1} = 0$

$y = 1 \quad v_{r,2} = v_{\theta,2} = v_{z,2} = 0$

$y = y_i \quad v_{r,1} = v_{r,2}$

$v_{\theta,1} = v_{\theta,2}$

$v_{z,1} = v_{z,2}$

$Dv_{z,1} + i\alpha v_{r,1} = \mu_{21}(Dv_{z,2} + i\alpha v_{r,2})$

$Dv_{\theta,1} = \mu_{21}Dv_{\theta,2}$

$-i\alpha c[p_1 - p_2 - \frac{2}{Re_1}(2Dv_{r,1} - \mu_{21}Dv_{r,2})] + [\epsilon Re_1(1 - \rho_{21} - S\alpha^2]v_{r,2} = 0$

where $Re_1 = \Omega_1 R_1 d/\nu_1 = O(1/\epsilon)$. The viscous analysis is then restricted to stationary bifurcations (pitchforks due to the problem symmetry) where $c = 0$ at the bifurcation point. This simplification is justified because in the single fluid problem, axisymmetric modes always appear through pitchfork bifurcations. As a result, at the bifurcation point, the radial velocity, v_r, and the interface deformation amplitude, h, are identically zero. In effect, this analysis predicts a flat interface at the onset of the vortex motion, which is again consistent with the experimental observations (Figure 6.14). The general solution to the governing equations at $c = 0$ is

$$v_{\theta,1} = a_1 \cosh q_0 y + b_1 \sinh q_0 y + c_1 \cosh qy + d_1 \sinh qy + e_1 \cosh q^* y + f_1 \sinh q^* y$$

$$v_{\theta,2} = a_2 \cosh p_0 y + b_2 \sinh p_0 y + c_2 \cosh py + d_2 \sinh py + e_2 \cosh p^* y + f_2 \sinh p^* y$$

where q_0, q, q^* are roots to $(q^2 - \alpha^2)^3 = -T_1 \alpha^2$. Similarly, p_0, p, p^* are roots to $(p^2 - \alpha^2)^3 = -T_2 \alpha^2$. With these simple equations for $v_{\theta 1}$ and $v_{\theta 2}$, the homogenous boundary conditions reduce to twelve equations and twelve unknowns of the form, $Ax = 0$, where A is the matrix of equation components for the disturbance velocities and x is the vector of undetermined coefficients $(a_1, b_1, c_1, d_1, e_1, f_1, a_2, b_2, c_2, d_2, e_2, f_2)$. This analysis will not give information about the Rayleigh-Taylor instability that occurs when $\rho_1 > \rho_2$, because in this case c is never zero. Also, this analysis will not predict viscous shear instabilities since they would be non-axisymmetric. For a given wavenumber, α, the critical Taylor numbers are those Taylor numbers for which a non-trivial solution to $Ax = 0$ exists. Numerical determination of the nullspace of A is straightforward.

The inviscid analysis predicts the basic features of the two-fluid Taylor-Couette instability, and the viscous linear stability analysis provides more detailed predictions. Since the Taylor numbers are awkwardly large for two-fluid Taylor-Couette flow, the simpler bifurcation parameter of the inviscid analysis,

Ω_{21}, is also used. Figure 3.3 shows the linear stability predictions for several Ekman numbers. The wavenumber is fixed at $\alpha = 5.365$ for all these calculations; Ω_{21c} is rather insensitive to the value used. The flow is stabilized as the Ekman number increases, which occurs when the viscosity increases, the rotation rate (Ω_2) decreases or the gap width decreases ($R_{12} \to 1$). When Ek_2 is small, the linear stability results lie just below the uppermost inviscid curve. As Ek_2 increases, the most significant deviation from the inviscid curves is when $\mu_{21} < 1$. This is because when $\mu_{21} < 1$, the inviscid analysis predicts that instability occurs first in the outer phase, so this is the phase that determines stability. Any increase in the relative importance of viscosity of that phase will suppress instability. The effect of Ek_2 on stability when $\mu_{21} \gg 1$ should be small because here instability occurs in the inner phase, whose properties are unaffected by Ek_2. Several contour plots of the stream function for various viscosity ratios are in Figure 3.4. From these figures it is apparent that although motion occurs in both phases, the motion appears to be driven by the Rayleigh unstable phase. The asymmetry between phases at $\mu_{21} = 1$ is due to the finite gap width, whose effect remains in the Taylor numbers.

Figure 3.5 shows the effect of density ratio on the viscous linear stability predictions. There is no effect in the inviscid limit and the effect remains small in the presence of viscosity. One interesting observation, however, is that the minimum in Ω_{21c} vs. μ_{21} (when $\alpha = 5.365$) evidently always occurs at $T_1 = T_2 =$

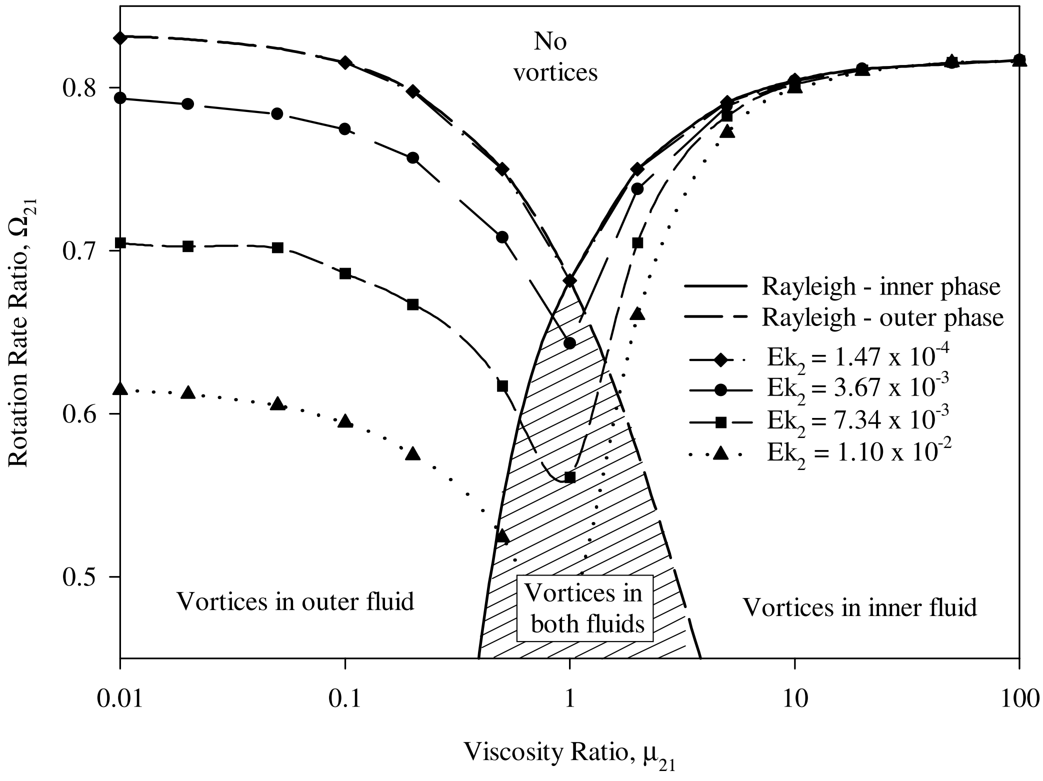

Figure 3.3: The inviscid and viscous theoretical predictions for various viscosity ratios. The two curves are the Rayleigh criterion for the outer fluid and the inner fluids. The shaded area indicates when vortices occur in both phases. The points represent the viscous analysis predictions for various outer phase viscosities. Here $\rho_{21} = 1.11$, $\rho_2 = 1.15$ g/ml, $R_{12} = 0.826$, $R_2 = 5.05$ cm, $\epsilon = 0.174$, $\Omega_2 = 7$ rev/s, $Q_1 = Q_2 = 0$, $n = 0$, $\alpha = 5.365$, and $y_i = 0.5$.

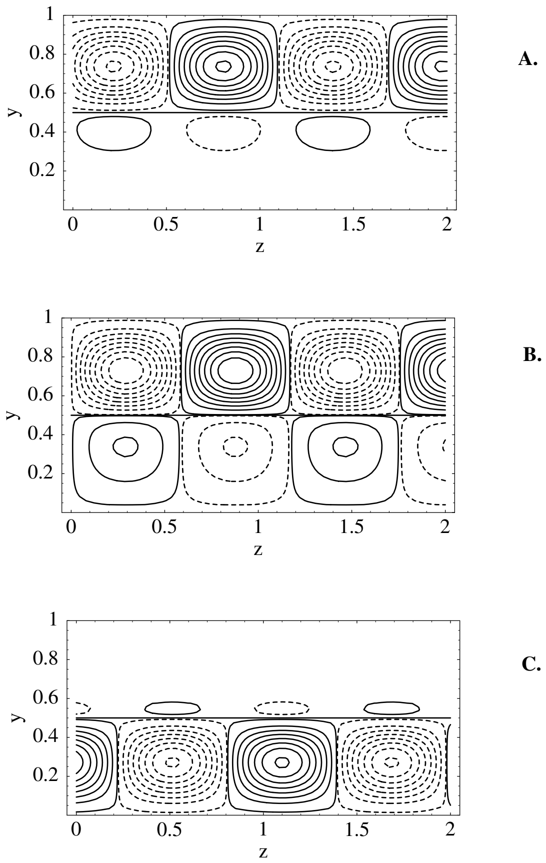

Figure 3.4: Stream functions for two-fluid Taylor-Couette flow with various viscosity ratios. Here $\rho_{21} = 1.36$, $\rho_2 = 1.15$ g/ml, $R_{12} = 0.826$, $R_2 = 5.05$ cm, $\epsilon = 0.174$, $\Omega_2 = 8$ rev/s, $Ek_2 = 8.48 \cdot 10^{-4}$, $y_i = 0.5$, $Q_1 = Q_2 = 0$, $n = 0$, and $\alpha = 5.365$. The vortices represented by the solid lines rotate in the opposite direction to those represented by the dashed lines. **A.** $\mu_{21} = 0.2$, $\Omega_{21} = \Omega_{21c} = 0.7955$, **B.** $\mu_{21} = 1.0$, $\Omega_{21} = \Omega_{21c} = 0.6794$, **C.** $\mu_{21} = 5.0$, $\Omega_{21} = \Omega_{21c} = 0.7908$.

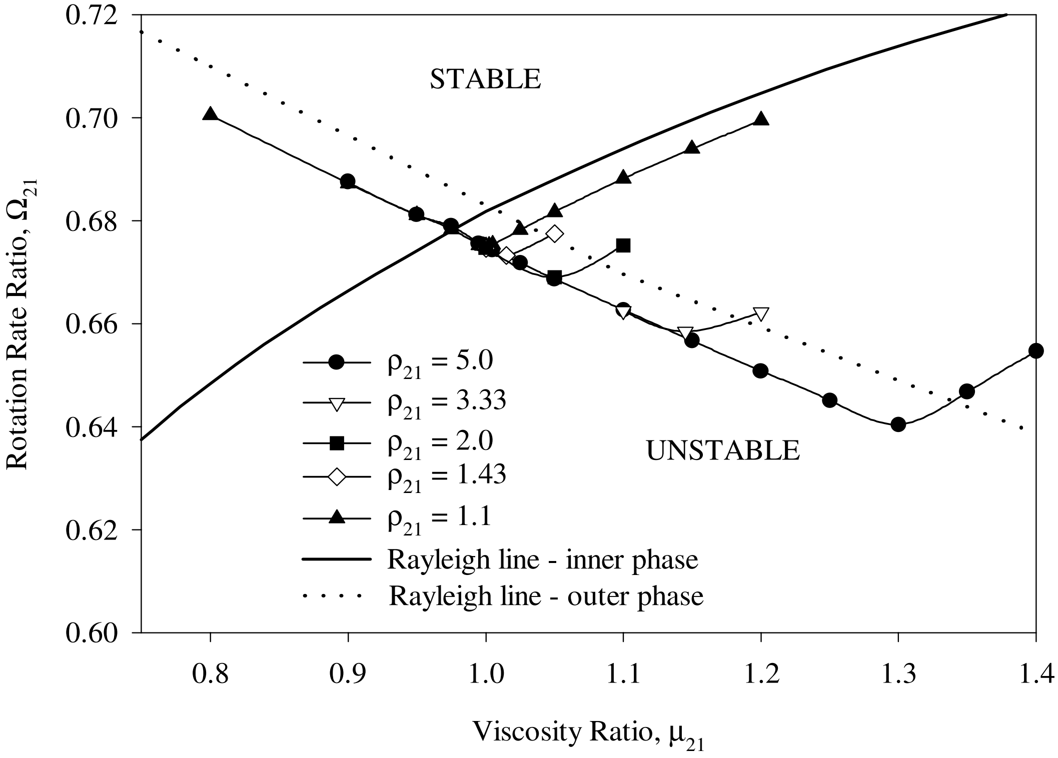

Figure 3.5: The effect of density ratio on the onset of two-fluid Taylor-Couette flow with $R_{12} = 0.826$, $R_2 = 5.05$ cm, $\epsilon = 0.174$, $\Omega_2 = 7$ rev/s, $Ek_2 = 1.47 \cdot 10^{-3}$, $y_i = 0.5$, $Q_1 = Q_2 = 0$, $n = 0$ and $\alpha = 5.365$.

$17,610$ the critical Taylor number of the odd solution in the one fluid problem.

When the fluids are of equal depth, the viscous analysis predicts no qualitative differences from the inviscid anlysis. However, when the less viscous fluid layer is sufficiently thin (i.e., where y_i or $1 - y_i$ is small), viscous effects become more important and can cause the *more viscous, thicker* layer to be the least stable. Figure 3.6 shows the effect of interface position for $\mu_{21} = 0.69$ and various Ekman numbers. The Rayleigh criteria for the inner and outer fluids and the critical axial wavenumber, α_c, are also shown. From this figure, it is observed that (1) increasing the Ekman number is stabilizing, and (2) the less viscous phase is unstable until a critical layer thinness, at which point the more viscous, thicker phase becomes the unstable phase. The vortices remain approximately square and the axial wavenumber indicates which phase is unstable. The abrupt change in wavenumber identifies the critical thinness where the unstable phase switches to the other. After the switch, the stability is given, to a good approximation, by the Rayleigh criterion for the thicker, more viscous layer. As the effective viscosity (Ekman number) increases, the critical thinness required approaches equal fluid depths. Figure 3.7 plots the stream functions for several interface positions at the corresponding critical wavenumbers.

As the radius ratio approaches unity, the Rayleigh criterion predicts that the rotation rate ratio also approaches unity. However, the viscous analysis again finds that viscous effects become important as the layers become thinner. Figure

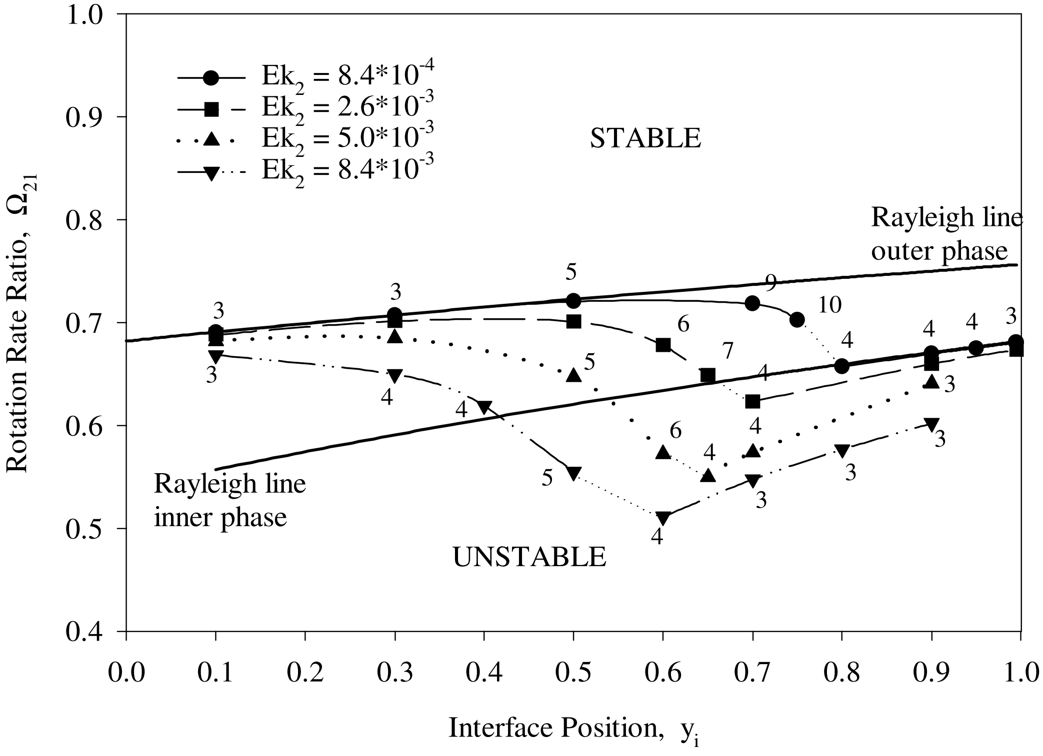

Figure 3.6: The effect of interface position on the critical rotation rate ratio. Here $\mu_{21} = 0.69$, $Ek_2 = 8.48 \cdot 10^{-4}$, $\rho_{21} = 1.35$, $\rho_2 = 1.15$ g/ml, $R_{12} = 0.826$, $R_2 = 5.05$ cm, $\epsilon = 0.174$, and $\Omega_2 = 8$ rev/s. The numbers represent the critical axial wavenumber (to the nearest integer), α_c. These results are from the numerical analysis of section 3.2.3 with $J_2 = 1939$ and $Q_1 = Q_2 = 0$.

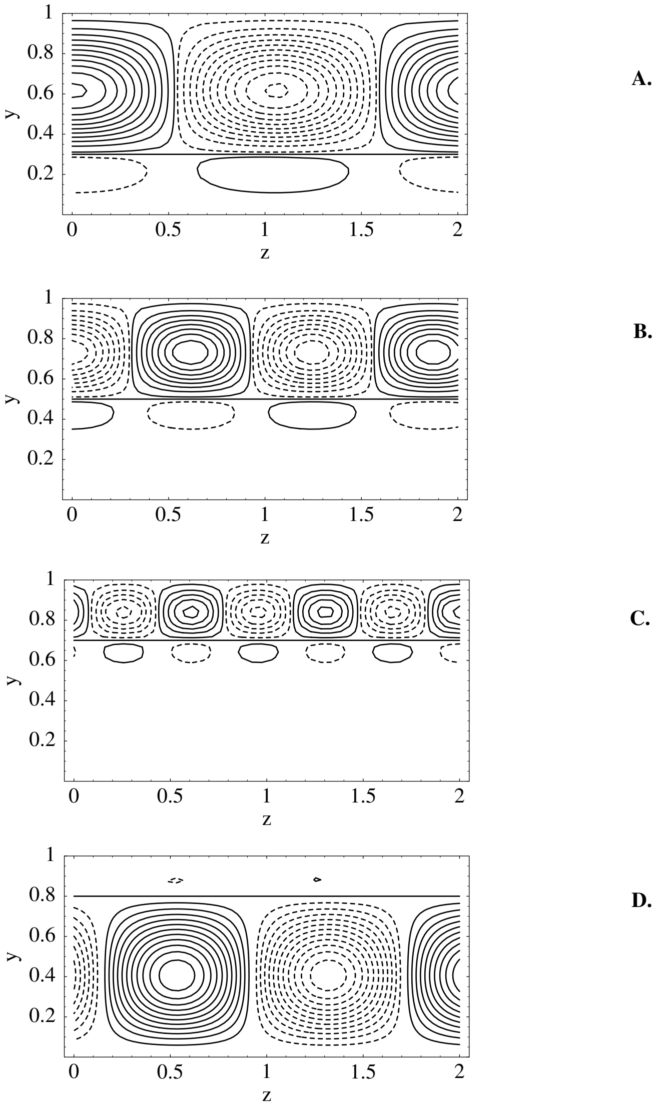

Figure 3.7: Stream functions for several different interface positions. Here $\mu_{21} = 0.69$, $\rho_{21} = 1.35$, $\rho_2 = 1.15$ g/ml, $R_{12} = 0.826$, $R_2 = 5.05$ cm, $\epsilon = 0.174$, $\Omega_2 = 8$ rev/s, $Ek_2 = 8.4 \cdot 10^{-3}$, and $n = 0$. These results are from the numerical analysis of section 3.2.3 with $J_2 = 1939$ and $Q_1 = Q_2 = 0$. The vortices represented by the solid lines rotate in the opposite direction to those represented by the dashed lines. **A.** $y_i = 0.3$, $\Omega_{21} = \Omega_{21c} = 0.7070$, $\alpha = 3$, **B.** $y_i = 0.5$, $\Omega_{21} = \Omega_{21c} = 0.7206$, $\alpha = 5$, **C.** $y_i = 0.7$, $\Omega_{21} = \Omega_{21c} = 0.7183$, $\alpha = 9$. **D.** $y_i = 0.8$, $\Omega_{21} = \Omega_{21c} = 0.6572$, $\alpha = 4$.

3.8 shows this stabilizing effect for several Ekman numbers.

In addition to the stabilizing effects of the Ekman number, increasing surface tension slightly stabilizes the system. Surface tension has a greater effect at higher Ekman numbers, although the effect remains small. This is because the dimensionless group measuring the surface tension term in the normal stress boundary condition is small for the conditions studied here ($\frac{\Omega_{21}}{4J_2 E k_1 \epsilon (1-\rho_{21})} < 1$).

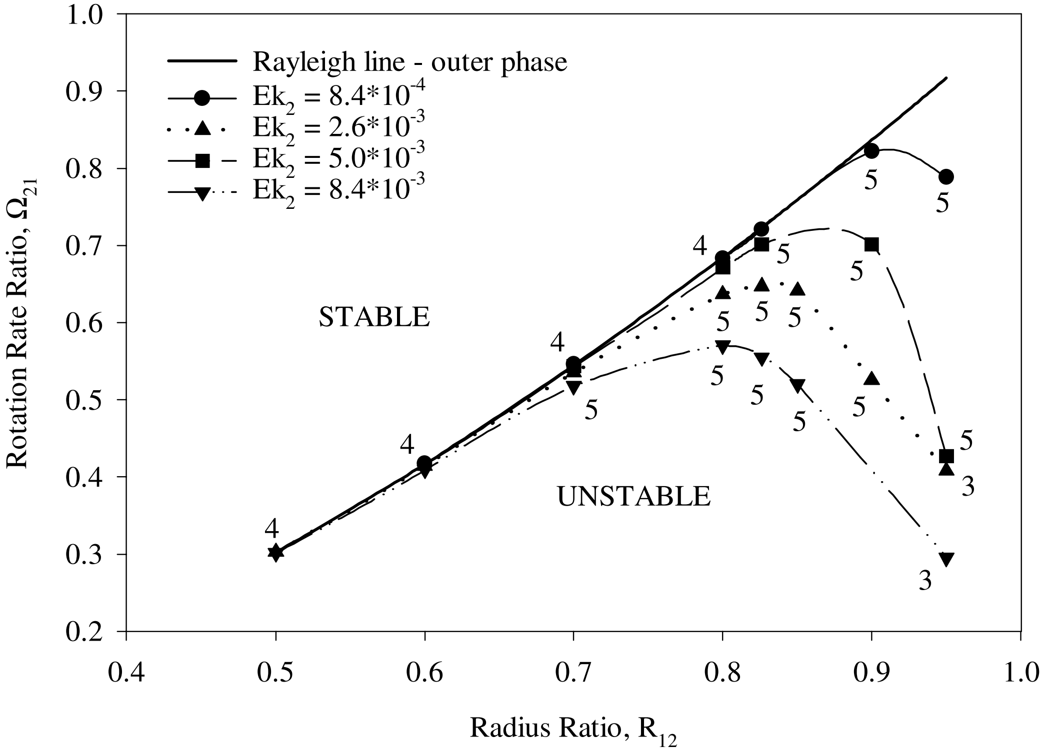

Figure 3.8: The effect of radius ratio on the critical rotation rate ratio. Here $\mu_{21} = 0.69$, $\rho_{21} = 1.35$, $\rho_2 = 1.15$ g/ml, $R_2 = 5.05$ cm, $\Omega_2 = 8$ rev/s, and $y_i = 0.5$. The numbers represent the critical axial wavenumber (to the nearest integer), α_c. These results are from the numerical analysis of section 3.2.3 with $J_2 = 1939$ and $Q_1 = Q_2 = 0$.

3.2.3 Viscous Analysis with Counterflow

For the theoretical analysis of two-fluid Taylor-Couette with countercurrent axial flow, a full numerical analysis is used. The governing equations and boundary conditions were discretized using Chebyshev collocation: Chebyshev-Gauss-Lobatto integration points were used for the velocities and Chebyshev-Gauss points for pressure [13]. In each phase, 16 collocation points were used for the velocities and 15 for pressure; the results reported here are independent of the number of points. The resulting algebraic generalized eigenvalue problem is solved with a public-domain subroutine that uses QZ factorization [37]. Instability occurs when $Im(c) \geq 0$.

With this numerical analysis, no simplifying assumptions were used, as they were in the initial analysis without counterflow (section 3.2.2). In the limit of no axial counterflow, the results from this numerical analysis agree well with both the analysis above and the analysis of Renardy and Joseph [93]. Therefore, the assumptions of narrow gap ($d/R_2 \rightarrow 0$), near rigid rotation ($\Omega_{21} \approx 1$), and axisymmetry ($n = 0$) are in fact very good for the conditions reported in section 3.2.2.

The effects of countercurrent axial flow are summarized in Figures 3.9 and 3.10. From these graphs the following observations may be made: (1) At low flow rates there is no effect on the onset of the vortex flow or on the structure

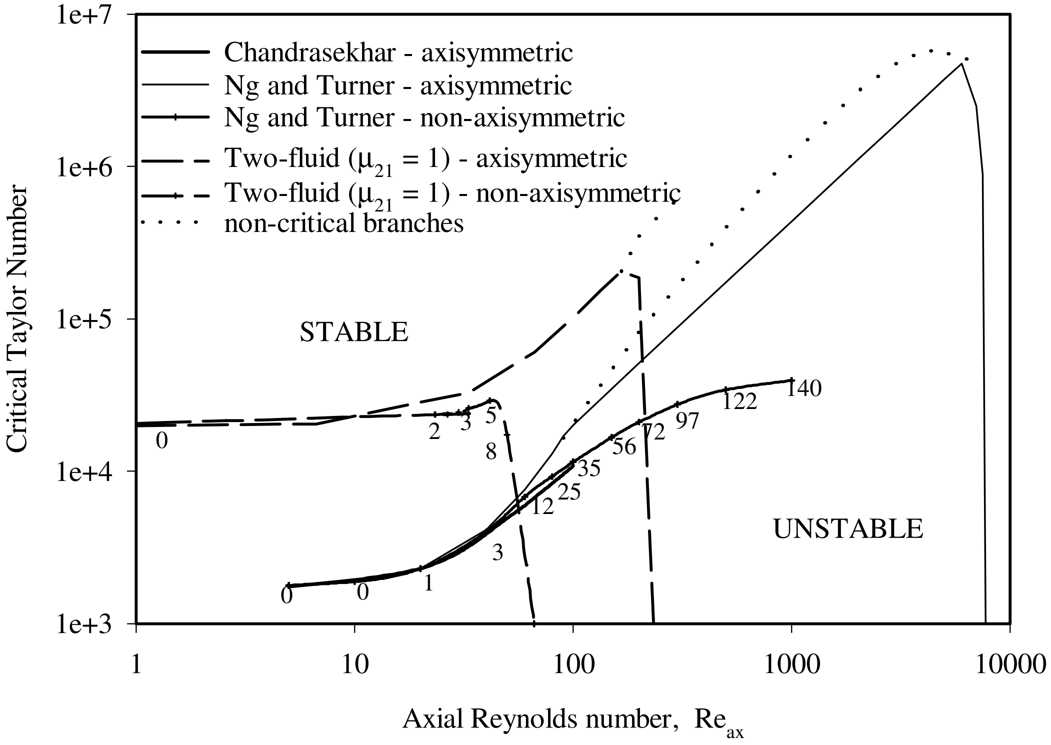

Figure 3.9: The critical Taylor number for one fluid Taylor-Couette flow with axial flow and two-fluid Taylor-Couette flow with countercurrent axial flow. For the two fluid case $\mu_{21} = 1.0$, $\rho_{21} = 1.35$, $\rho_2 = 1.15$ g/ml, $R_{12} = 0.826$, $R_2 = 5.05$ cm, $\epsilon = 0.174$, $\Omega_2 = 8$ rev/s, $Ek_2 = 8.48 \cdot 10^{-4}$, $y_i = 0.5$, $Q_1 = Q_2$, and $J_2 = 1939$. For the non-axisymmetric cases, the numbers represent the critical azimuthal wavenumber, n_c. Both Chandrasekhar's and Ng and Turner's one fluid results are for $R_{12} = 0.95$, $\Omega_2 = 0$.

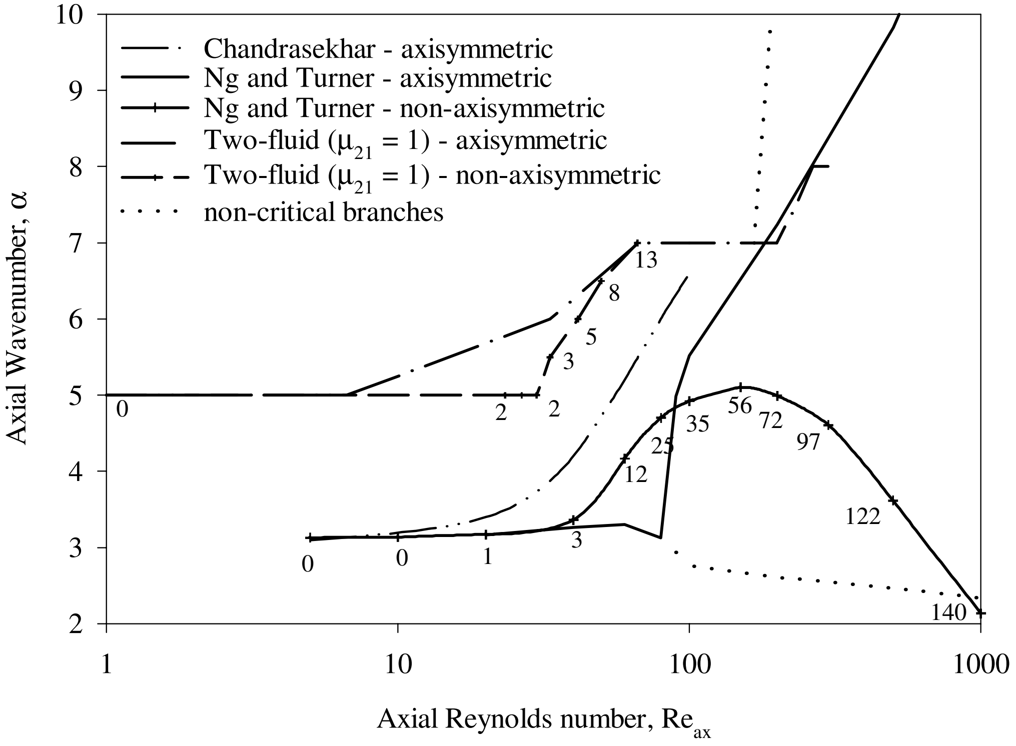

Figure 3.10: The critical axial wavenumber for one fluid Taylor-Couette flow with axial flow and two-fluid Taylor-Couette flow with countercurrent axial flow. For the two fluid case $\mu_{21} = 1.0$, $\rho_{21} = 1.35$, $\rho_2 = 1.15$ g/ml, $R_{12} = 0.826$, $R_2 = 5.05$ cm, $\epsilon = 0.174$, $\Omega_2 = 8$ rev/sec, $Ek_2 = 8.48 \cdot 10^{-4}$, $y_i = 0.5$, $Q_1 = Q_2$, and $J_2 = 1939$. For the non-axisymmetric cases, the numbers represent the azimuthal wavenumber, n_c. Both Chandrasekhar's and Ng and Turner's one fluid results are for $R_{12} = 0.95$, $\Omega_2 = 0$.

of the vortices as described by the axial and azimuthal wavenumbers. (2) At moderate flowrates the flow is slightly stabilized and both wavenumbers increase; the vortices become thinner and form helices. (3) At very high flowrates, the flow is strongly destabilized indicating the appearance of another instability. (4) Axisymmetric modes are less destabilizing than non-axisymmetric modes. These results all agree qualitatively with similar observations for one fluid Taylor-Coeutte flow, which are included in Figures 3.9 and 3.10. For both the one and two fluid cases the relation $T \propto Re_{ax}$ holds for the axisymmetric case at moderate flowrates. The second instability that appears in the one fluid problem at high axial flowrates is believed to be the Tollmien-Schlichting instability in the boundary layer [85]; for the two-fluid case the second instability is a Kelvin-Helmholtz mode (discussed further below). When the flow is not forced to be axisymmetric, the one and two fluid flows show less agreement with each other. For two-fluid Taylor-Couette flow, countercurrent axial flow weakly stabilizes when $Re_{ax,2} < 50$. In contrast, axial flow is quite stabilizing for single fluid Taylor-Couette flow for $Re_{ax} < 7000$. The difference between the one and two fluid problems is the appearance of the Kelvin-Helmholtz instability in the two fluid case at relatively low axial Reynolds numbers. The Kelvin-Helmholtz instability continues to dominate at even higher axial Reynolds numbers and at sufficiently high axial flow occurs at rigid rotation. The Tollmien-Schlichting instability was not observed in either the axisymmetric or non-axisymmetric two fluid problem.

Several stream functions for the axisymmetric flow with $Q_{12} = 1$ and $\mu_{21} = 0.69$ are shown in Figure 3.11. With the linear stability analysis, the amplitude of the disturbance velocities is determined only within a multiplicative factor. Therefore, the stream functions (which are a sum of the base and disturbance flows) are representative only and not exact. The wavespeed direction generally corresponds to the fluid flow direction where the vortices are stronger. The vortices in both phases travel in that same direction, although the flow overall is countercurrent. As seen in the figures, some streamlines "bypass" the vortex structure, and a characteristic pattern of stagnation points develops. With increasing axial Reynolds numbers, the vortices become thinner and one vortex appears to be drawn under its neighbor. At the very high Reynolds numbers, a completely different pattern appears. Particularly, the stagnation pattern shifts to that characteristic of the Kelvin's "cat's eye" pattern that arises in the Kelvin-Helmholtz instability. For the viscosity ratios explored ($\mu_{21} = 0.69, 1.0, 1.46$), when the axial flow rate is higher in the inner phase ($Q_{21} < 1$), this Kelvin-Helmholtz mode is strongly destabilized and the flow pattern very non-axisymmetric. Figure 3.12 shows this effect for matched viscosity fluids. The most stable flow occurs as the viscosity ratio approaches unity; the flow is noticeably stabilized in the moderate Reynolds number region and is nearly axisymmetric as shown in Figure 3.13 for $Q_{21} = 1$. As μ_{21}

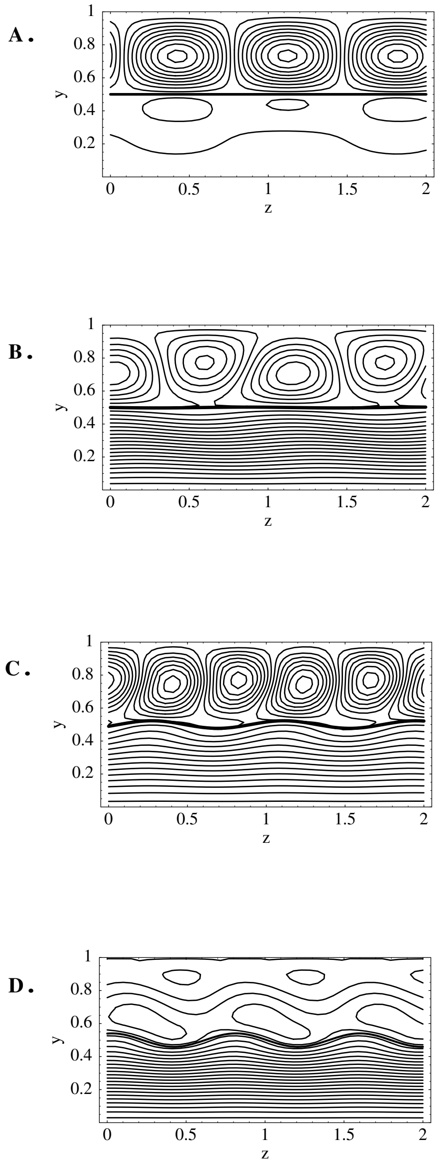

Figure 3.11: Stream functions, in a reference frame traveling with the wavespeed $Re(c)$, for two-fluid Taylor-Couette flow with countercurrent axial flow. Here $\mu_{21} = 0.69$, $\rho_{21} = 1.35$, $\rho_2 = 1.15$ g/ml, $R_{12} = 0.826$, $R_2 = 5.05$ cm, $\epsilon = 0.174$, $\Omega_2 = 8$ rev/s, $Ek_2 = 8.48 \cdot 10^{-4}$, $n = 0$, $Q_1 = Q_2$, and $J_2 = 1939$. The darker lines indicate the interface. **A.** $Re_{ax,2} = 0.33$, $\alpha = 4.5$, $\Omega_{21} = \Omega_{21c} = 0.6793$, **B.** $Re_{ax,2} = 33$, $\alpha = 5.5$, $\Omega_{21} = \Omega_{21c} = 0.6776$, **C.** $Re_{ax,2} = 100$, $\alpha = 7.5$, $\Omega_{21} = \Omega_{21c} = 0.6689$, and **D.** $Re_{ax,2} = 232$, $\alpha = 8$, $\Omega_{21} = \Omega_{21c} = 0.6866$.

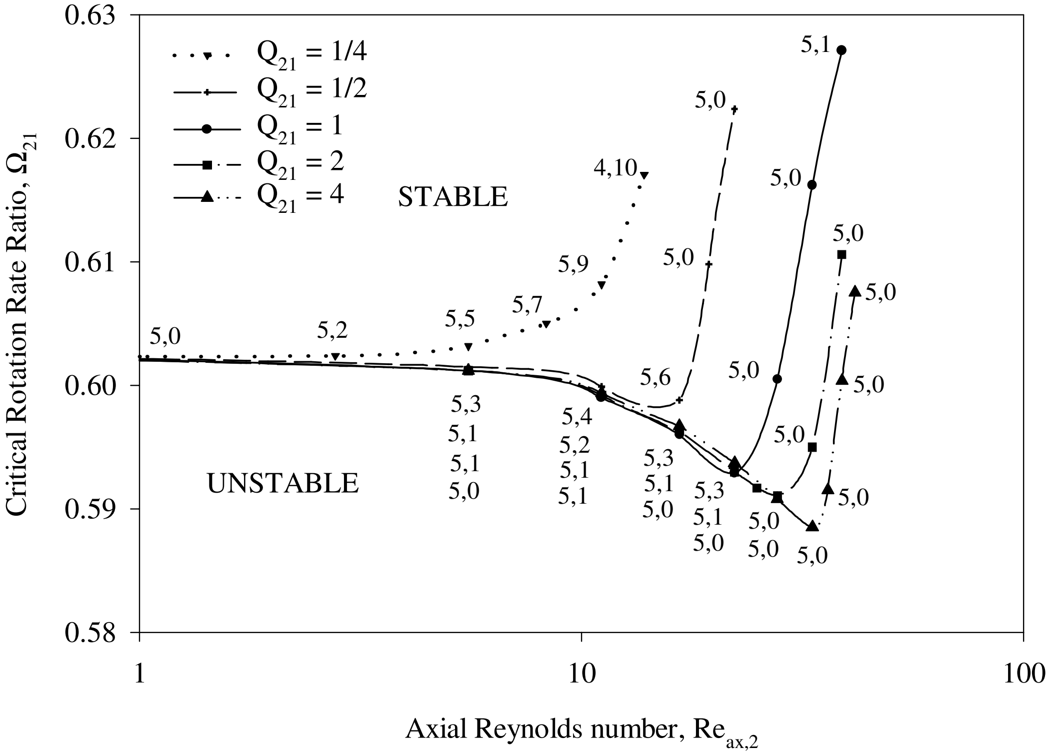

Figure 3.12: The effect of unmatched countercurrent flowrates. Here $\mu_{21} = 1.0$, $\rho_{21} = 1.35$, $\rho_2 = 1.15$ g/ml, $R_{12} = 0.826$, $R_2 = 5.05$ cm, $\epsilon = 0.174$, $\Omega_2 = 8$ rev/s, $y_i = 0.5$, $Ek_2 = 5.04 \cdot 10^{-3}$, $J_2 = 1939$, and $\Omega_{21,Reax,2=0} = 0.6024$. The numbers represent the axial wavenumber (to the nearest integer) and the aximuthal wavenumber (α_c, n_c).

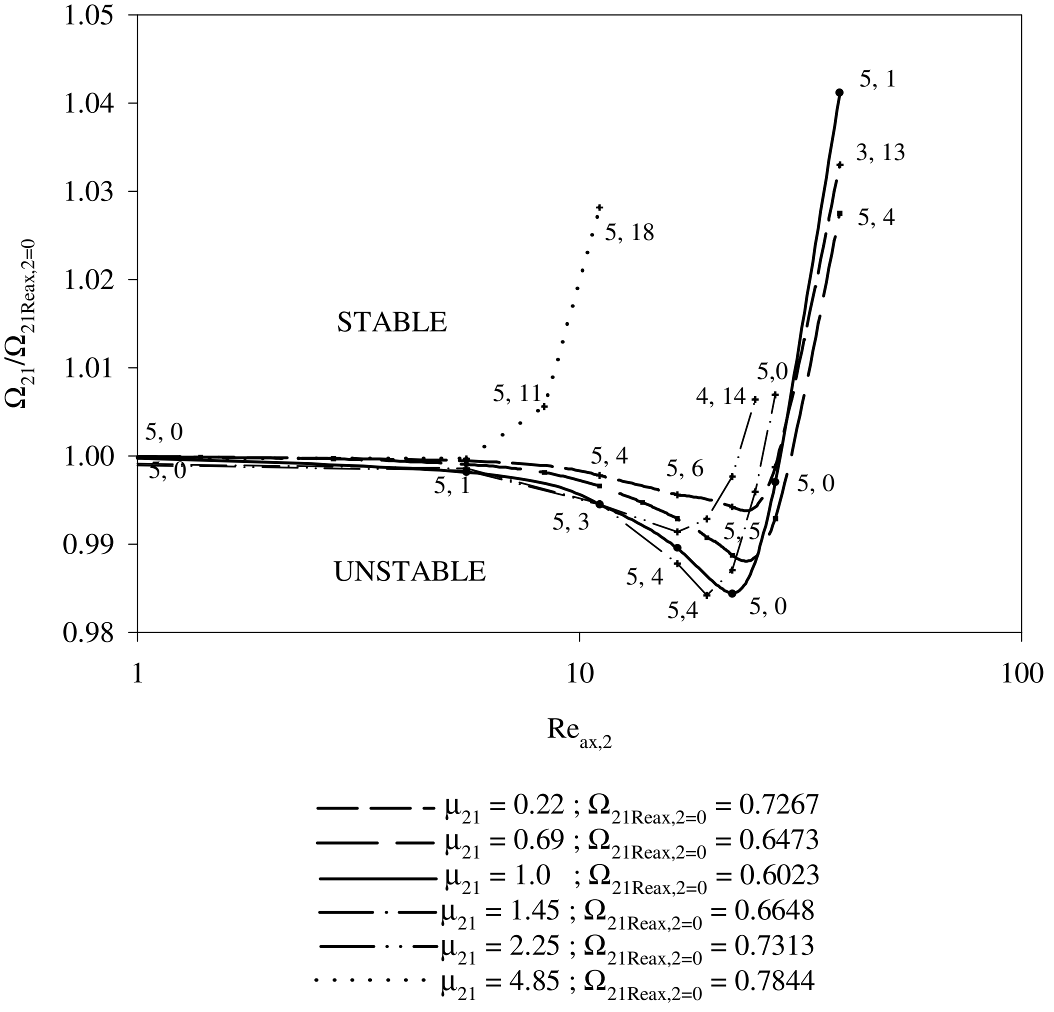

Figure 3.13: The effect of viscosity ratio on the critical rotation rate with countercurrent flow. Here $\rho_{21} = 1.35$, $\rho_2 = 1.15$ g/ml, $R_{12} = 0.826$, $R_2 = 5.05$ cm, $\epsilon = 0.174$, $\Omega_2 = 8$ rev/s, $y_i = 0.5$, $Ek_2 = 5.04 \cdot 10^{-3}$, $Q_1 = Q_2$, and $J_2 = 1939$. The numbers represent the axial wavenumber (to the nearest integer) and the aximuthal wavenumber (α_c, n_c).

increases the Kelvin-Helmholtz mode is destabilized and the flow again very non-axisymmetric. In general, the first derivative of base axial flow is discontinuous at the interface and the flow profile does not have an inflection point elsewhere. However, the change in concavity may be measured by the jump in the second derivative $(d^2W_1/dy^2 - d^2W_2/dy^2)|_{y=y_i}$. As either Q_{21} decreases (for $\mu_{21} = 0.69, 1.0, 1.46$) or μ_{21} increases (for $Q_{21} = 1$), this jump increases and the flow is destabilized, consistent with Rayleigh's inflection point theorem.

Figure 3.14 shows that surface tension stabilizes the Kelvin-Helmholtz instability as expected from other studies [14, 30]. Also apparent, from the values of $\Omega_{21Reax,2=0}$ in the legend, is the slight stabilizing effect of surface tension on two-fluid Taylor-Couette flow.

The effect of Ekman number is shown in Figures 3.15 and 3.16. With increasing viscosity, the second instability occurs at a higher average axial velocity, but at a lower axial Reynolds number (the average axial velocity scaled by viscosity). The flow is also less asymmetric with higher viscosity fluids.

For all of the cases studied, there was no evidence of the interfacial instability due to the azimuthal shear of fluid layers with different viscosities [36]. Furthermore, the Taylor-Couette instability always appeared with vortices counterrotating across the interface; i.e., points just across the interface from one another have very similar velocities. Both of the computational fluid dynamics packages, FLUENT and FIDAP (sections 4.1 and 4.2), predict that above the

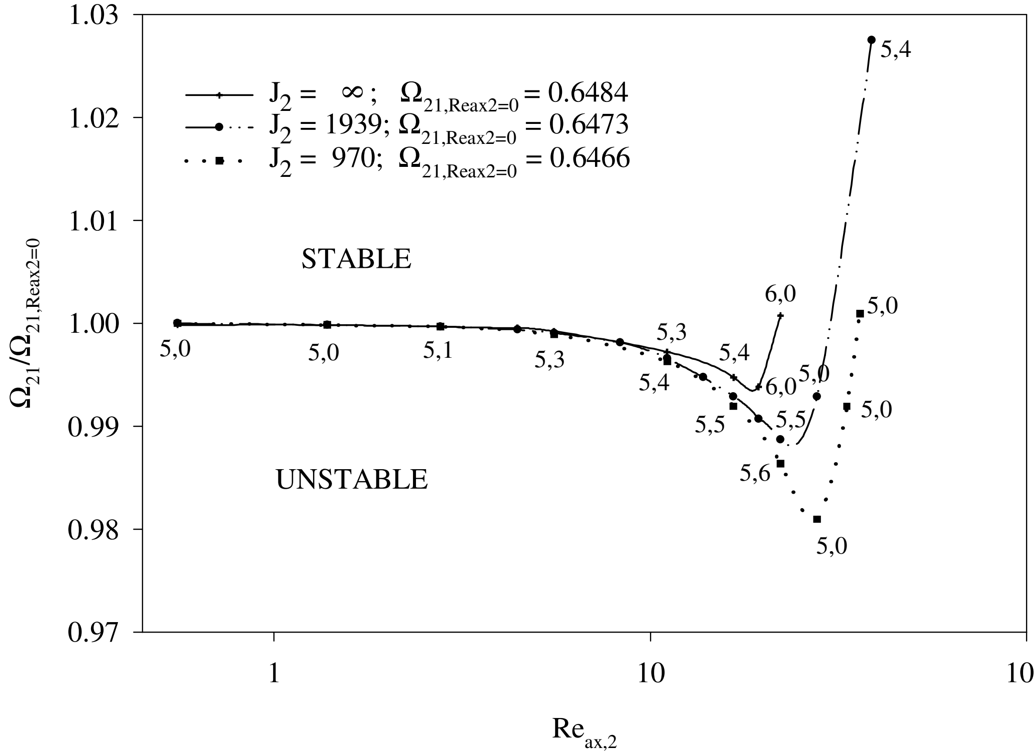

Figure 3.14: The effect of surface tension on the onset of the Kelvin-Helmholtz instability. Here $\mu_{21} = 0.69$, $\rho_{21} = 1.35$, $\rho_2 = 1.15$ g/ml, $R_{12} = 0.826$, $R_2 = 5.05$ cm, $\epsilon = 0.174$, $\Omega_2 = 8$ rev/s, $y_i = 0.5$, $Q_1 = Q_2$. The numbers represent the axial wavenumber (to the nearest integer) and the aximuthal wavenumber (α_c, n_c).

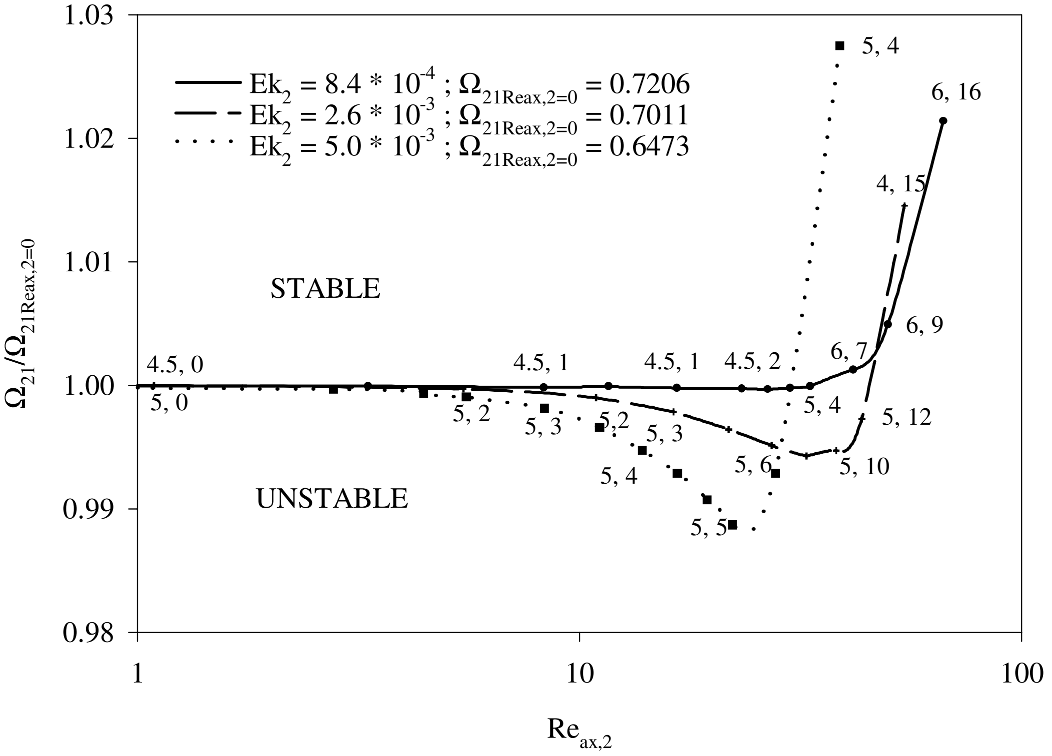

Figure 3.15: The effect of viscosity on the critical rotation rate with counter-current flow measured by axial Reynold numbers. Here $\mu_{21} = 0.69$, $\rho_{21} = 1.35$, $\rho_2 = 1.15$ g/ml, $R_{12} = 0.826$, $R_2 = 5.05$ cm, $\epsilon = 0.174$, $\Omega_2 = 8$ rev/s, $y_i = 0.5$, $Q_1 = Q_2$, and $J_2 = 1939$. The numbers represent the axial wavenumber (to the nearest integer) and the aximuthal wavenumber (α_c, n_c).

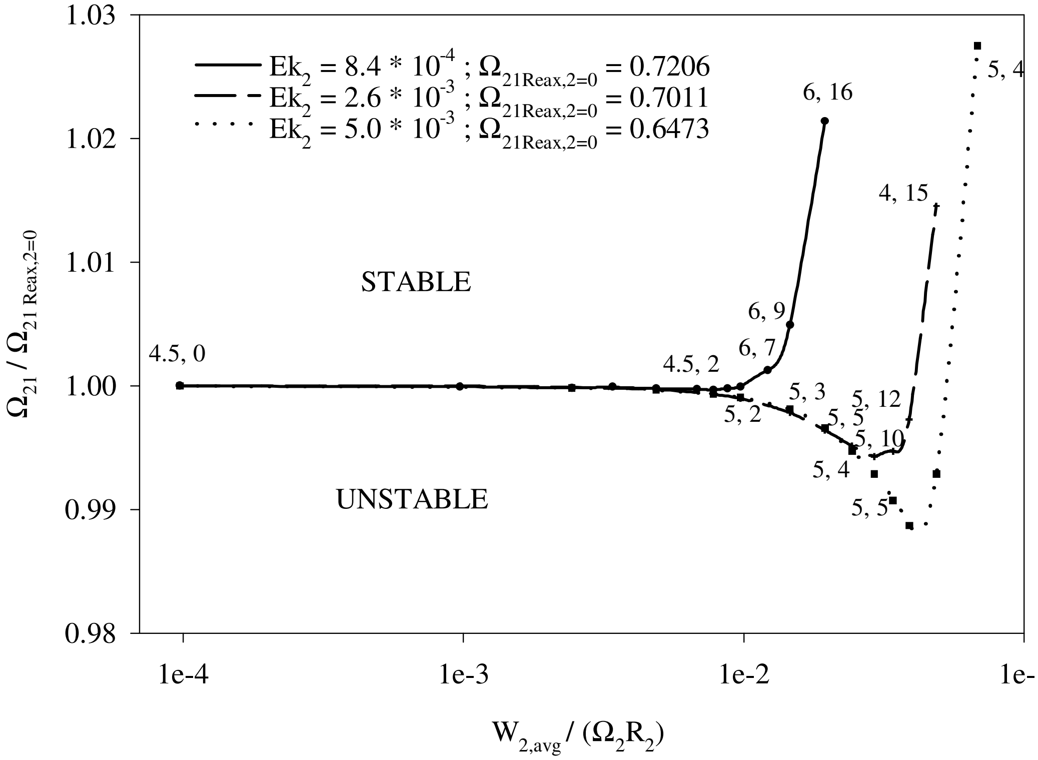

Figure 3.16: The effect of viscosity on the critical rotation rate with counter-current flow as measured by scaled axial velocity. Here $\mu_{21} = 0.69$, $\rho_{21} = 1.35$, $\rho_2 = 1.15$ g/ml, $R_{12} = 0.826$, $R_2 = 5.05$ cm, $\epsilon = 0.174$, $\Omega_2 = 8$ rev/s, $y_i = 0.5$, $Q_1 = Q_2$, and $J_2 = 1939$. The numbers represent the axial wavenumber (to the nearest integer) and the aximuthal wavenumber (α_c, n_c).

critical point the vortex pattern can change from counterrotation of vortex pairs across the interface to a stable corotation state. Since the linear stability analysis is valid only at the onset of two-fluid Taylor-Couette flow, it cannot directly determine supercritical flow behavior. However, the second mode to go unstable in the linear stability analysis can give an indication of other important flow patterns. When the two fluids are identically matched, with equal fluid depths, negligible curvature, and no countercurrent axial flow, the linear stability analysis predicts counterrotating vortices (the odd solution) as the primary unstable mode. A corotating vortex state is the second mode to be unstable. However, this corotating mode is significantly affected by counterflow, as shown in Figure 3.17. Once $Re_{ax} > 3$, the first mode resembles the second, the difference being which phase has stronger vortices. This suggests that countercurrent axial flow can sufficiently affect the problem symmetry to eliminate corotating vortices.

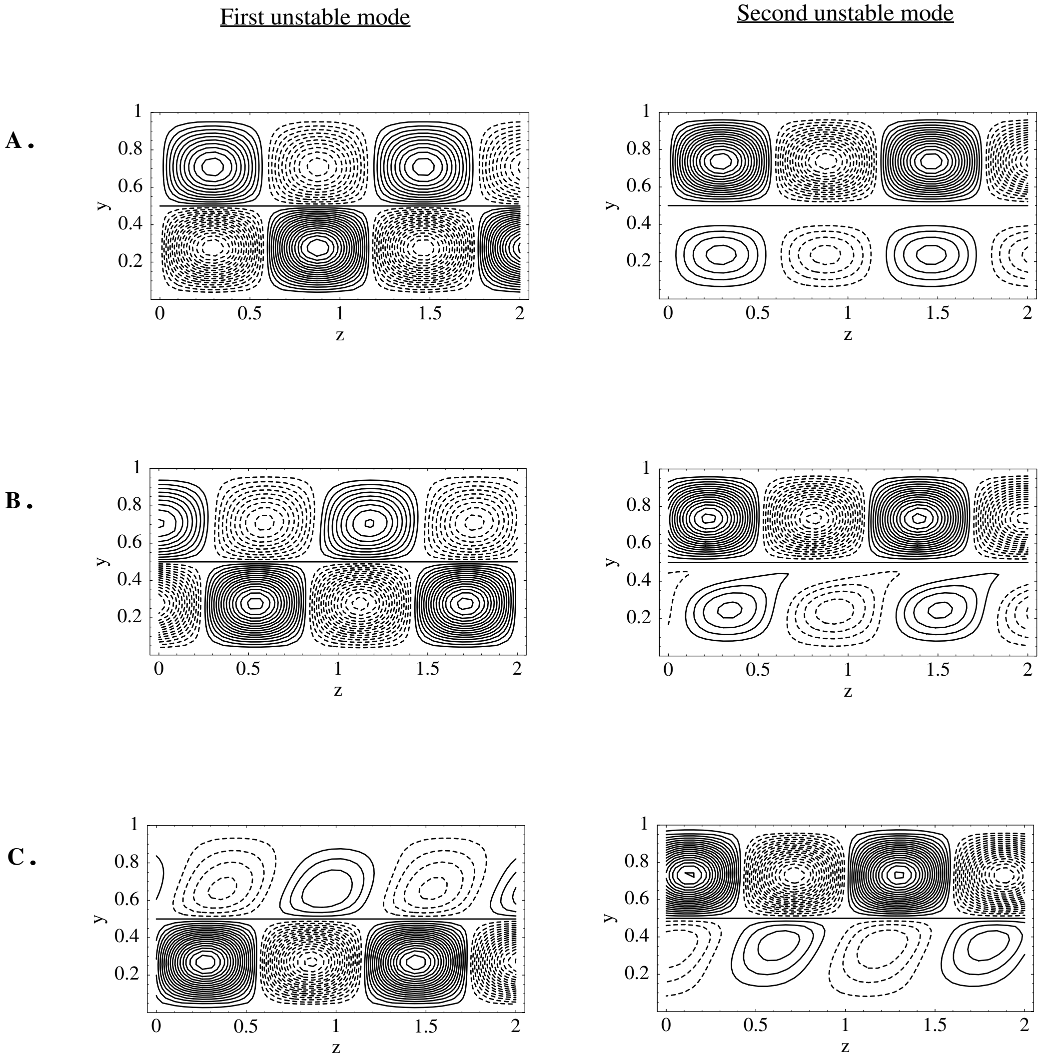

Figure 3.17: Stream functions, in a reference frame traveling with the wavespeed, $Re(c)$, for the first and second unstable modes with increasing countercurrent axial flow. Here $\mu_{21} = 1$, $\rho_{21} = 1.0145$, $\rho_2 = 1.14$ g/ml, $R_2 = 5.05$ cm, $\epsilon = 0.174$, $y_i = 0.5$, $Ek_2 = 8.4 * 10^{-4}$, $\Omega_2 = 8$ rev/s, $J_2 = 1939$, $\alpha = 5.365$ and $n = 0$. **A.** $Re_{ax,2} = 0.0$, **B.** $Re_{ax,2} = 0.33$, **C.** $Re_{ax,2} = 3.3$

Chapter 4

Computational Fluid Dynamics Studies

The linear stability analyses of sections 3.2.2 and 3.2.3 are useful in understanding the onset of the vortex flow, but do not predict either the magnitude of the vortex velocities or the behavior beyond the critical point. For this, computational fluid dynamics (CFD) may be used. These CFD results may also be combined with boundary layer theory to predict the mass transfer characteristics of the flow. Boundary layer theory (see section 5) is useful when the majority of the mass transfer occurs in a boundary layer region. For these situations, a full numerical analysis would require very high resolution in the boundary layer region and therefore would be computationally intensive.

Several commercial computational fluid dynamics software packages were used to simulate one and two-fluid Taylor-Couette flow: FLUENT and FIDAP, both products of Fluent, Inc (Lebanon, NH). Both packages solve the Navier-Stokes equations, but differ in their discretization schemes. FLUENT uses a control volume method with first order polynomials. As a result, FLUENT is a more general software package designed to handle laminar, turbulent, and mildly compressible flows. Each cell communicates with only its nearest neighbors and therefore fine grids are often required. For convergence, the error decreases as K^{-1}, where K is the number of grid elements. FIDAP is a finite element method which uses first or second order polynomials to discretize the flow problem. The second order polynomials allow more distant cells in the grid to communicate with each other and is preferred for laminar and free surface problems. The error decreases as K^{-N} relative to changes in the grid sizing and as $e^{-\alpha N}$ relative to changes in the order, N, of the interpolating polynomial. The number of grid elements is K and α is characteristic of the specific problem. In the FIDAP runs, second order polynomials were used. As with all computational fluid dynamics packages, the results should be independent of the grid and polynomial order. Data was collected at specified points to track the development of the flow and confirm that the asymptotic solution was reached and transient behavior had ceased.

With both FLUENT and FIDAP, all simulations were modeled as axisymmetric with swirl velocity and periodic boundary conditions in the axial direction, which is consistent with the fluid mechanics studies with low axial flowrates. The one fluid problem was reproduced, and then extended to the two fluid case. FLUENT was used for calculating the velocity field for one fluid Taylor-Couette flow which was then used with boundary layer theory to calculate the radial mass transfer coefficients. FIDAP was used for two-fluid Taylor-Couette flow and the calculated velocity field used with penetration theory to calculate interphase mass transfer. FIDAP was chosen for two-fluid Taylor-Couette flow since it can calculate the interface position rigorously; FLUENT uses a less accurate Volume of Fluid (VOF) method. Although both FLUENT and FIDAP were successful, the iterations required were time consuming even with good initial conditions. Therefore, CFD would be most effective in exploring only selected areas of the parameter space, such as equipment dimensions to design future prototypes.

4.1 FLUENT

4.1.1 One Fluid Taylor-Couette Flow

FLUENT correctly reproduced the one fluid Taylor problem at low rotation rates with the steady solver. The velocity fields from similar FLUENT runs agree qualitatively with the numerical analysis of Fasel and Booz [33] and with experimental results of Sobolik *et. al* [99] and Parker and Merati [88].

FLUENT was also able to correctly simulate the one fluid problem with a high outer cylinder rotation rate using the time dependent solver. In general, computational fluid dynamics packages do not easily solve flow problems with strong centrifugal components. When the azimuthal velocity was initialized to

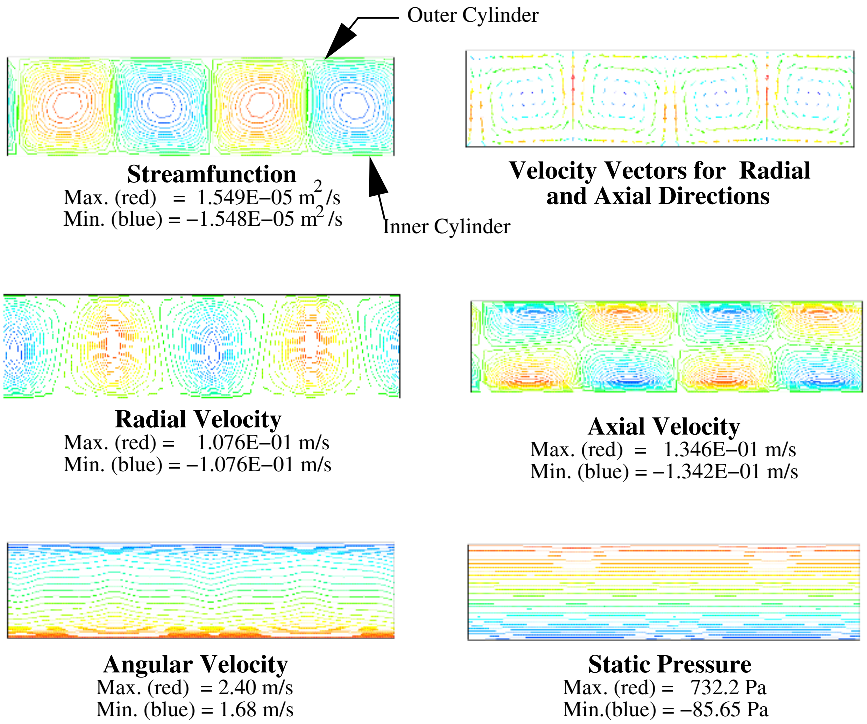

Streamfunction
Max. (red) = 1.549E−05 m^2/s
Min. (blue) = −1.548E−05 m^2/s

Velocity Vectors for Radial and Axial Directions

Radial Velocity
Max. (red) = 1.076E−01 m/s
Min. (blue) = −1.076E−01 m/s

Axial Velocity
Max. (red) = 1.346E−01 m/s
Min. (blue) = −1.342E−01 m/s

Angular Velocity
Max. (red) = 2.40 m/s
Min. (blue) = 1.68 m/s

Static Pressure
Max. (red) = 732.2 Pa
Min.(blue) = −85.65 Pa

Figure 4.1: FLUENT results for one fluid Taylor-Couette flow with a high outer cylinder rotation rate. $T = 29930$, $\Omega_{21} = 0.576$, $\Omega_{21,c} = 0.676$, $\alpha = \pi$, $\Omega_2 = 6$ rev/s, $R_2 = 5.35$ cm, $d/R_2 = 0.18$, $\rho = 1$ g/ml, $\mu = 10$ cp.

the analytical solution at rigid rotation and with slow continuous increases in the inner cylinder rotation rate, FLUENT maintained a solution. The FLUENT results for one fluid Taylor-Couette flow near the critical point with a high outer cylinder rotation rate are summarized in Figure 4.1. The velocities scale approximately linearly with the outer cylinder rotation rate. This FLUENT run corresponds to the point marked F on Figure 6.8 of the experimental results in section 6.3.1.

FLUENT was primarily used to calculate the velocity field for one fluid Taylor-Couette flow, which was then used in boundary layer theory to calculate the mass transfer from the inner cylinder wall to the bulk. Boundary layer theory is discussed in section 5.1 and a comparison of these calculated mass transfer rates rates with the reported experimental values are in section 2.3. For comparison with experimental data, the conditions for the CFD runs were chosen to match the experiments of Coeuret and Legrand [16, 70]: $R_1 = 1.75$ cm, $d = 0.25$ cm, 0.5 cm, or 0.75 cm, $\nu = 1.0$ cm^2/s, $\rho = 1.0$ g/ml. Axial flow was not included in the CFD calculations, since low axial flow rates hardly affect either the onset of Taylor-Couette flow or the axial wavenumber, $\alpha \approx 3.117$. However, axial flow is expected to increase axial dispersion and therefore add to discrepancies with the experiments. These effects are further discussed in section 2.3. In the FLUENT runs, the axial wavenumber is controlled by the aspect ratio. Here length/gap width = 2, so $\alpha = \pi$. As in the corresponding one fluid experiments, the outer cylinder remained stationary and only the inner cylinder rotated. In the boundary layer regions near the cylinder walls a fine grid was used with a gradual coarsening towards the center of the flow region. Typical CFD results for the stream function and the axial velocity component are included in Figure 4.2. As in Figure 4.2b, the axial velocity gradient is more uniform along the inner cylinder than along the outer cylinder and therefore the inner cylinder should provide a more uniform mass transfer surface.

At the critical Taylor number the velocity gradient at the wall is purely sinusoidal in the axial direction. At higher Taylor numbers, higher order harmonics become important as seen in Figures 4.2b and 4.3. Figure 4.3 is a graph of the axial velocity gradient for the inner cylinder versus axial position as calculated within FLUENT. A positive axial velocity gradient corresponds to counterclockwise rotation. Since the velocity gradient is identical in magnitude for clockwise and counterclockwise vortices, the average Nusselt number calculated for the counterclockwise vortices applies for all vortices. As the Taylor number is increased, the average axial velocity gradient increases, and the maximum velocity gradient shifts towards the vortex boundary where the flow is towards the inner cylinder. At sufficiently high Taylor numbers, the flow becomes non-axisymmetric and these axisymmetric CFD simulations are less representative of the experiments.

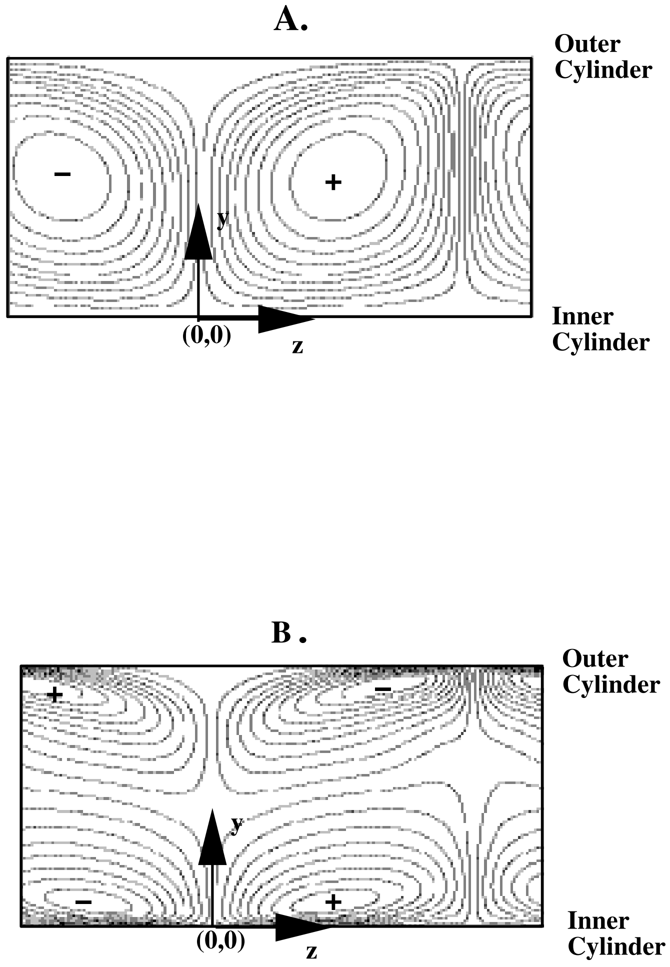

Figure 4.2: The stream function and axial velocity component of one fluid Taylor-Couette flow as calculated by FLUENT. The conditions are $d/R_1 = 0.286$, $Ta = 857$, $Ta_c = 40$, $Re_z = 0$. **A.** The streamfunction scaled by $\Omega_1 R_1 d^2$ with a maximum value of 0.163 and increment of 0.017. **B.** The axial velocity scaled by $\Omega_1 R_1$ with a maximum value of 0.187 and increment of 0.020.

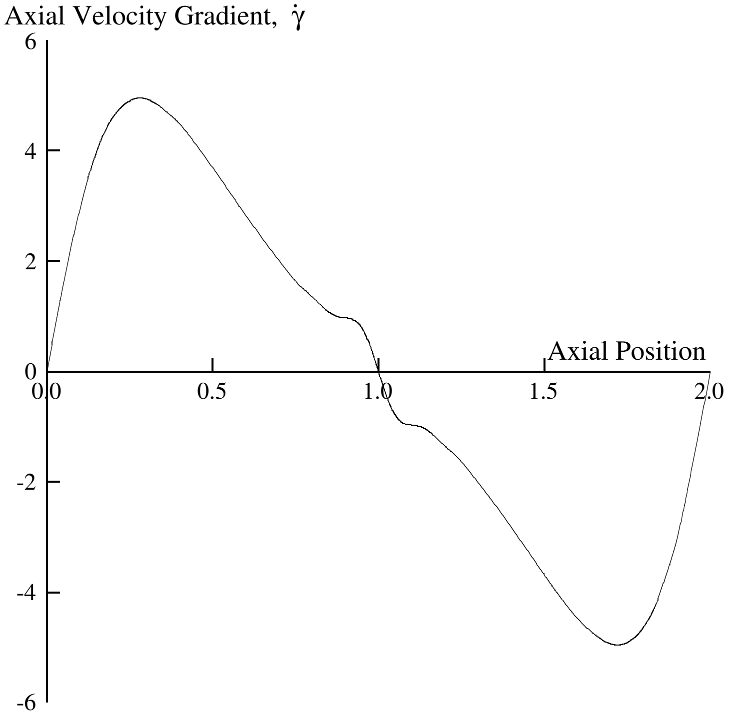

Figure 4.3: The axial velocity gradient at the inner cylinder in one fluid Taylor-Couette flow as a function of axial position along the inner cylinder. The axial velocity gradient is scaled by $d/(\Omega_1 R_1)$ and the axial position by d. The conditions are $d/R_1 = 0.286$, $Ta = 857$, $Ta_c = 40$, $Re_z = 0$.

4.1.2 Two-Fluid Taylor-Couette Flow.

FLUENT solved the two fluid Taylor problem using the Volume of Fluid (VOF) method. With VOF the local physical properties are based on volume averaging the pure component properties in the area surrounding the calculation points. The time dependent solver is required with the VOF method. The grid fineness was increased in the interface region for better detail on the interface behavior. As with the one fluid problem at high rotation rates, the initial condition was rigid rotation and the inner cylinder rotation rate was slowly and continuously increased. Droplet formation would occur at the interface with sudden changes in the cylinder rotation rates or at high shear rates. The surface tension option in VOF is not required, but the interface droplet formation seemed more controllable when it is activated. Therefore, the surface tension option was used in the subsequent runs. The FLUENT results for two-fluid Taylor-Couette flow are included in Figure 4.4. The vortices are weaker in the inner phase due to its higher viscosity. This FLUENT run corresponds approximately to the point marked F on Figure 6.16 of the experimental results. At Taylor numbers above the critical point, FLUENT predicts that a vortex in one phase would corotate with its counterpart in the other phase; the velocity at the interface would be countercurrent. This was surprising. Since FLUENT does not calculate the interface rigorously, further CFD runs were completed with FIDAP to support this finding.

The CFD runs with low viscosity fluids were inconclusive. Either an extremely fine grid may be required to observe Taylor vortices at high rotation rates, or another form of instability may occur which violates the axisymmetric assumption of these FLUENT runs. The absence of simple Taylor vortices in low viscosity fluids agrees with the laboratory experiments where Taylor vortices were not observed, but rather non-axisymmetric time dependent patterns (the barber pole pattern) or the rippled interface (section 6.3.1).

To use FLUENT to simulate liquid-liquid extraction, VOF cannot be used. Instead the two fluids and single diffusing species must be modeled as three interdiffusing species. In this case, the surface tension option is unavailable. In addition, a very fine grid will be required for the diffusion length scale.

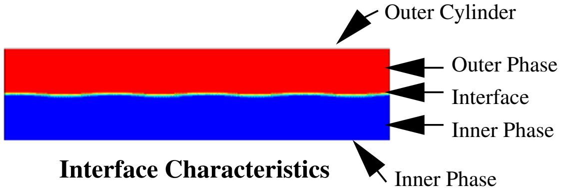

Interface Characteristics

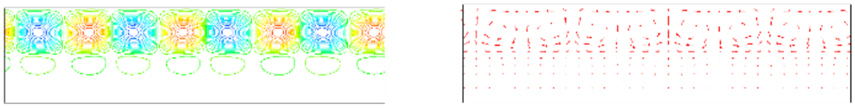

Streamfunction
Max. (red) = 3.138E−09 m^2/s
Min. (blue) = −3.137E−09 m^2/s

Velocity Vectors for Radial and Axial Directions

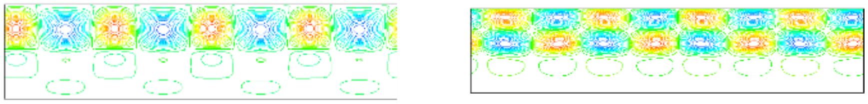

Radial Velocity
Max. (red) = 3.260E−02 m/s
Min. (blue) = −3.256E−02 m/s

Axial Velocity
Max. (red) = 3.640E−02 m/s
Min. (blue) = −2.975E−02 m/s

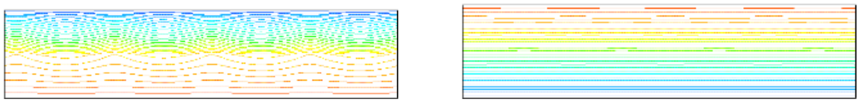

Angular Velocity
Max. (red) = 1.96 m/s
Min. (blue) = 1.68 m/s

Static Pressure
Max. (red) = 597.4 Pa
Min.(blue) = −9.34 Pa

Figure 4.4: FLUENT results for two-fluid Taylor-Couette flow. $\mu_2 = 10$ cp, $\rho_2 = 1$ g/ml, $\mu_{21} = 0.5$, $\rho_{21} = 1.23$, $y_i = 0.5$, $R_2 = 5.35$ cm, $d/R_2 = 0.18$, $\Omega_2 = 6$ rev/s, $\Omega_{21} = 0.706$, $\Omega_{21,c} = 0.745$, $J_2 = 1001$.

4.2 FIDAP

4.2.1 Two-Fluid Taylor-Couette Flow

Since FLUENT does not calculate the interface position rigorously, FIDAP was used to confirm the presence of corotating vortices at sufficiently high Taylor numbers. In addition, the results from FIDAP were used with penetration theory to calculate the interphase mass transfer rates in two-fluid Taylor-Couette flow. Penetration theory is discussed in section 5.2 and a comparison of the predictions and the experimental results are in 6.3.3.

FIDAP uses an adaptive finite element mesh to solve for the velocity fields and interface position. Finite elements are more flexible than finite volume schemes for complex or irregular geometries and boundary conditions. This includes problems with an interface, where the interface is a free surface whose position is an unknown that needs to be determined in addition to the velocity field. As a result, the nodes on the interface as well as nodes near the interface are allowed to move and deform the mesh. To solve for the interface position, FIDAP enforces at the interface the kinematic condition, the continuity of shear stress at the interface, the balance of normal stress and surface tension, and continuity of velocity. To speed convergence, initially the interface can be held fixed and the velocity field determined. The interface is then released and the total solution determined.

For comparision with experimental data, the conditions for the CFD runs were chosen to match the experiments of section 6: $R_2 = 5.05$ cm, $d/R_2 = 0.174$, $\Omega_1 = 12.5$ rev/s, $S = 50$ dynes/cm, and the remaining physical properties from Table 6.1 to match the specific experimental run. Axial flow could be included in the CFD calculations by requiring the ends to have the countercurrent axial profile calculated analytically in the absence of vortices. In the FIDAP runs, the axial wavenumber is controlled by the aspect ratio. Here length/gap width = 1, so $\alpha = 2\pi$, consistent with the linear stability analysis (section 3.2.3. As in the experiments, the FIDAP run was started at rigid rotation (12.5 rev/s) with the analytic solutions for the base flows as the initial conditions. The outer cylinder rotation rate was then continuously decreased to its final value. Typical CFD results for the stream function overlaid on the mesh and the velocity components are included in Figure 4.5. In the boundary layer regions near the cylinder walls and near the interface a fine grid was used with a gradual coarsening towards the center of the flow region. At the onset of the vortex flow, FIDAP predicts a flat interface, which deforms upon further increases past the critical point. This agrees with the experimental observations of section 6.3.1. The point of maximum interface deformation occurs where the flow is directed radially toward the interface in the Rayleigh unstable phase; the layer depth of that unstable phase is greatest at this point. This is visible in figures 4.5 and 4.6. These FIDAP runs are noted as F1 and F2 on Figures 6.16 and 6.17 in the experimental results section. For a given outer phase viscosity, the interface deformation increases with increasing viscosity difference between the two phases. These effects are illustrated in Figure 4.7 where the interfacial deformation is measured by the interfacial area per unit volume:

$$a = \frac{2}{(R_2^2 - R_1^2)} \int_a^b r_i(z)\sqrt{1 + (dr_i/dz)^2)}dz.$$

At the interface, the velocity component tangential to the interface was calculated from the FIDAP results and used in the penetration theory analysis; the normal component was confirmed to be zero.

As with FLUENT, FIDAP also predicts that at sufficiently high Taylor numbers, vortex pairs across the interface corotate with each other when axial counterflow is absent. This corotation is not an effect of interface deformation, but results from a secondary branch that bifurcates from the Couette flow solution and becomes stable only at higher relative rotation rates. The velocity field for corotating vortices is shown in Figure 4.6. For corotating vortices, the mass transfer would be better described by boundary layer theory with the linear velocity profile assumption rather than penetration theory. As a result, poorer mass transfer performance would be expected ($Nu \propto (Pe)^{1/3}$ instead of $Nu \propto (Pe)^{1/2}$). Corotation of vortices paired across the interface of axially stratified two-fluid Taylor-Couette flow was also observed by Toya and Nakamura [110]. When countercurrent axial flow is present, FIDAP does not predict corotating vortices, consistent with the fluid mechanics analysis in section 3.2.3.

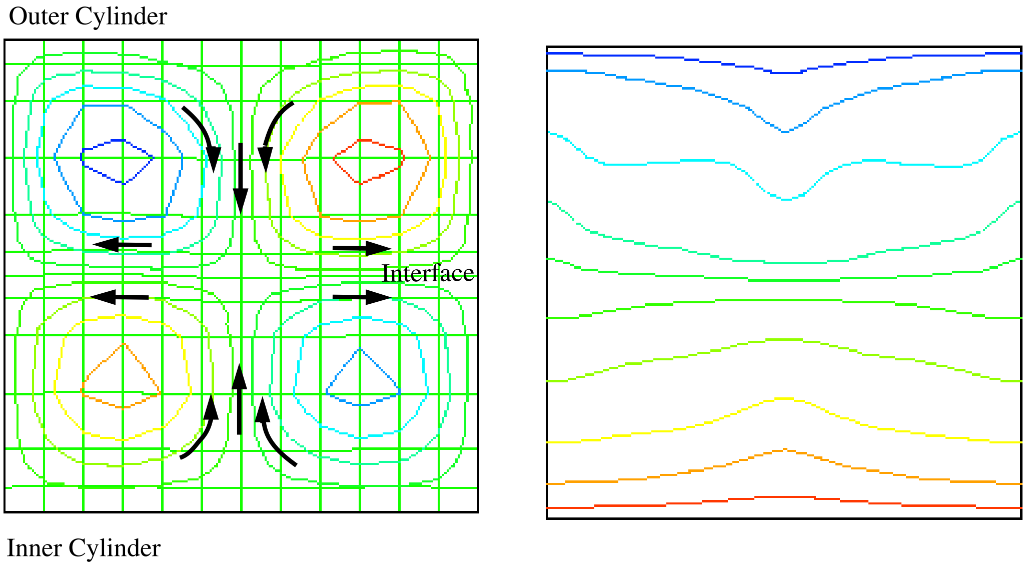

Stream function: 45.9 cm^2/s (red)
−46.0 cm^2/s (blue)

Angular Velocity: 323.3 cm /s (red)
248.5 cm /s (blue)

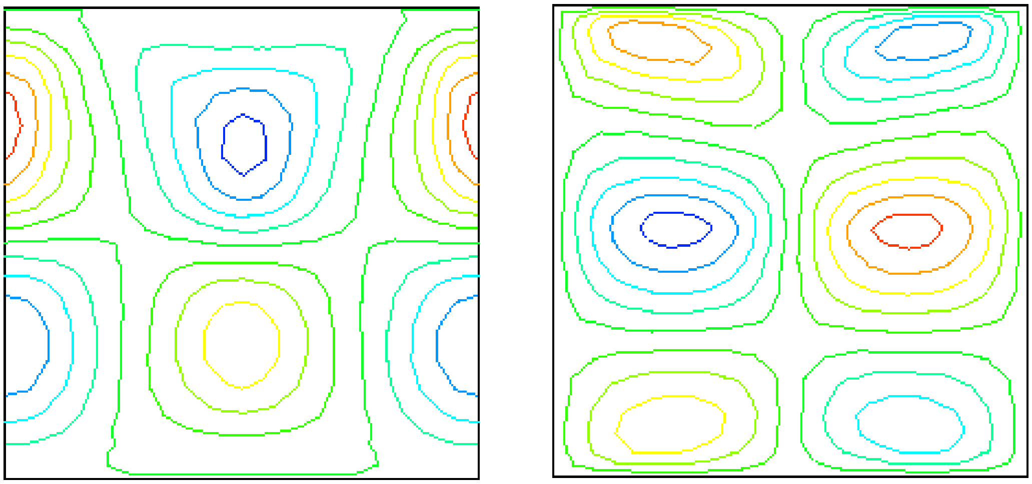

Radial Velocity: 15.4 cm /s (red)
−12.2 cm /s (blue)

Axial Velocity: 13.2 cm /s (red)
−13.3 cm /s (blue)

Figure 4.5: FIDAP results for the stream function and velocity components of two-fluid Taylor-Couette flow. The conditions are $d/R_2 = 0.174$, $\Omega_{21} = 0.62$, $\Omega_{21,c} = 0.73$, $Re_{2,ax} = 0.33$, $R_2 = 5.05$ cm, $\mu_{21} = 0.63$, Fluid pair 8-IL.

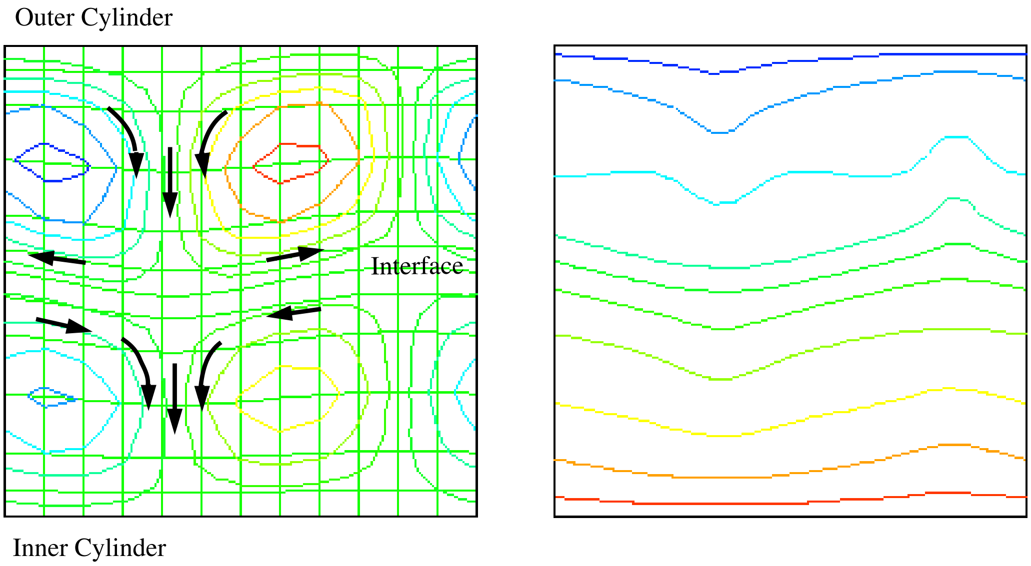

Stream function: 37.5 cm^2/s (red)

−35.8 cm^2/s (blue)

Angular Velocity: 323.3 cm /s (red)

248.5 cm /s (blue)

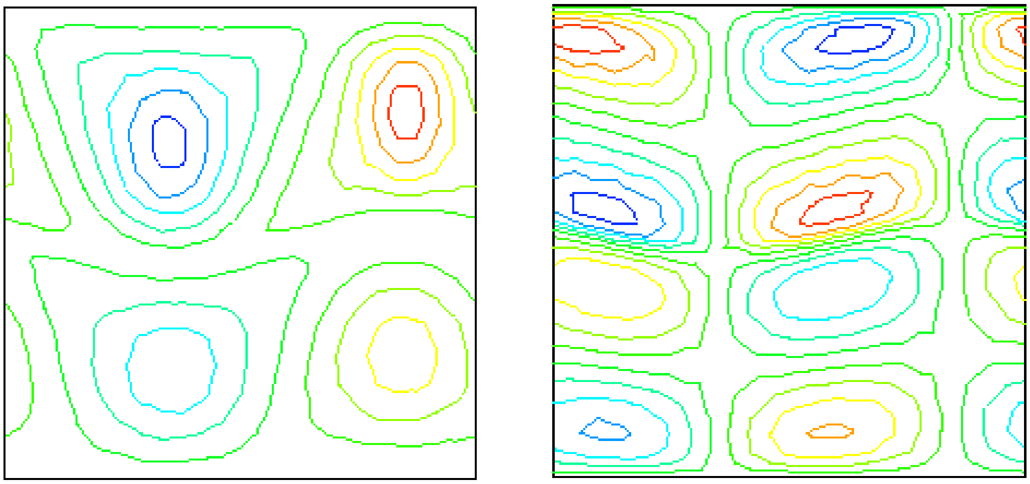

Radial Velocity: 11.8 cm /s (red)

−11.0 cm /s (blue)

Axial Velocity: 9.7 cm /s (red)

−9.4 cm /s (blue)

Figure 4.6: FIDAP results for the stream function and velocity components of two-fluid Taylor-Couette flow with corotating vortices. $d/R_2 = 0.174$, $\Omega_{21} = 0.62$, $\Omega_{21,c} = 0.73$, $Re_{2,ax} = 0$, $R_2 = 5.05$ cm, $\mu_{21} = 0.63$, Fluid pair 8-IL.

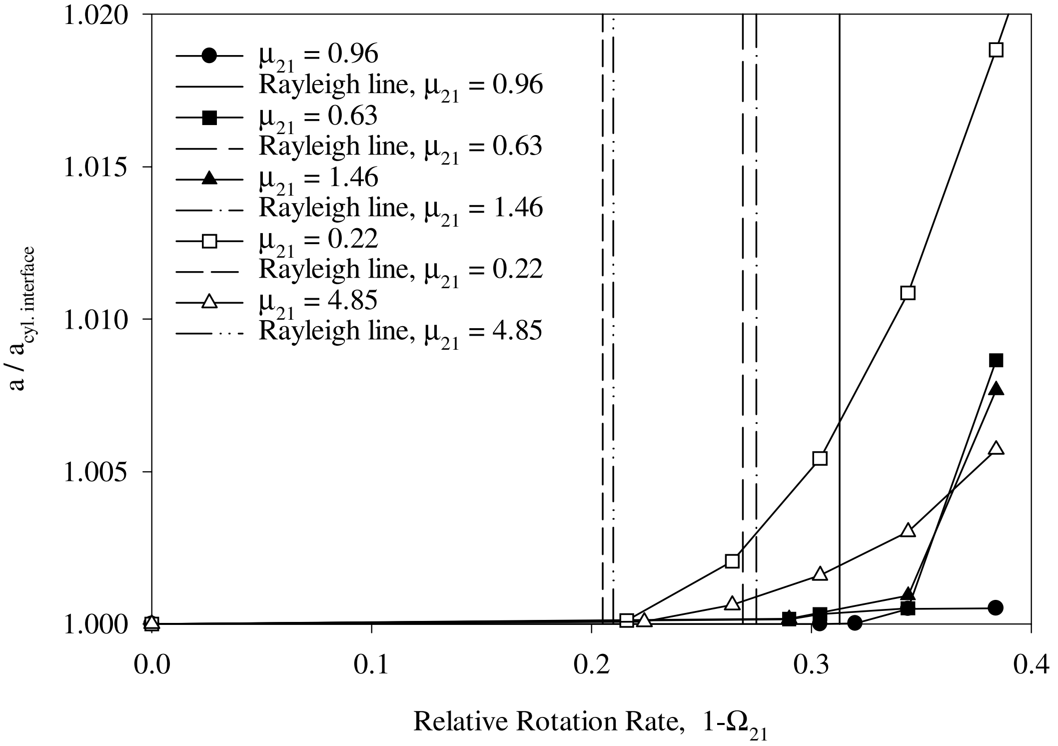

Figure 4.7: FIDAP predictions for the interface deformation with various viscosity ratios.

Chapter 5

Boundary Layer Theory

In general it can be quite difficult to accurately calculate mass transfer coefficients. Real systems are often complex and include physical property gradients, convective dispersion, and complicated geometries. Fortunately, in many situations the majority of mass transfer is limited to a thin boundary layer. In this case, boundary layer theory provides analytical solutions that can be accurate and are much less cumbersome than a full numerical analysis, which requires very high numerical resolution in the boundary layer region. Typically, boundary layer theory is useful under the following conditions: (1) the Schmidt number is sufficiently large that the concentration boundary layer thickness is small compared to both the velocity boundary layer and the local radius of curvature of the boundary, (2) the velocity in the concentration boundary layer is nearly parallel to the surface, (3) diffusion in the direction of the flow is negligible ($\partial^2 C/\partial z^2 \ll \partial^2 C/\partial y^2$) where, y and z represent the directions normal and tangent to the wall, respectively, (4) the concentration gradient is primarily confined to the concentration boundary layer, and (5) the physical properties are constant.

When the concentration boundary layer is thin compared to the velocity boundary layer, the velocity profile within the concentration boundary layer may be approximated either as (1) a linear profile, to approximate mass transfer from a solid surface such as flow past a flat plate, or as (2) a flat profile, to approximate the mass transfer across a fluid-fluid interface such as a falling film. The analysis with this flat velocity profile approximation is often also referred to as penetration theory. To use boundary layer theory, only the velocity gradient or the velocity at the mass transfer surface is required, depending on the specific approximation. In only a few cases is this velocity information obtainable analytically and in general numerical methods are required to determine the velocity field. A number of commercial computational fluid dynamics (CFD) packages are available for these calculations. In particular, FLUENT and FIDAP was used in combination with boundary layer theory to predict the mass transfer in one fluid and two-fluid Taylor-Couette flow, respectively. Section 4 further discusses these CFD packages. The flat profile approximation was used in the analysis for counterrotating vortices (cocurrent flow at the interface) and the linear velocity profile for corotating vortices (countercurrent flow at the interface).

The general two dimensional boundary layer solution (for dilute solutions in laminar flow) was developed by Acrivos [1] and extended to three dimensions by Stewart [101]. Here the development follows the discussion by Lightfoot [74]. For a two dimensional, Cartesian system the equation of continuity is

$$\frac{\partial v_z}{\partial z} + \frac{\partial v_y}{\partial y} = 0 \tag{5.1}$$

and the mass conservation equation of species A, neglecting diffusion in the z direction, is

$$ReSc\left(v_z\frac{\partial \Pi}{\partial z} + v_y\frac{\partial \Pi}{\partial y}\right) = \frac{\partial^2 \Pi}{\partial y^2} \tag{5.2}$$

where the scaled concentration is $\Pi = (C_A - C_{A,y=0})/(C_A - C_{A,y=\infty})$. The boundary layer starts to form at z_0, which in Taylor-Couette flow is the vortex boundary with flow towards the cylinder wall. The mass transfer surface is located at $y = 0$.

5.1 Linear Velocity Profile

When the velocity profile is approximated as linear within the concentration boundary layer

$$v_z = \dot{\gamma} y$$

the equation of continuity may be integrated to

$$v_y = -\frac{1}{2}\frac{\partial \dot{\gamma}}{\partial z} y^2.$$

With this substitution, equation 5.2 then becomes

$$ReSc\left(\dot{\gamma} y\frac{\partial \Pi}{\partial z} - \frac{1}{2}\frac{\partial \dot{\gamma}}{\partial z}\frac{\partial \Pi}{\partial y}\right) = \frac{\partial^2 \Pi}{\partial y^2}. \tag{5.3}$$

The standard boundary conditions require that at

$$\begin{array}{lll} \Pi = 0 & y = 0 & z > z_0 \\ \Pi \to 1 & y \to \infty & z > z_0 \\ \Pi = 1 & y > 0 & z < z_0. \end{array}$$

To solve this differential equation and boundary conditions, the concentration is assumed to be a function of the distance from the mass transfer surface and the boundary layer thickness

$$\Pi = \Pi(\xi)$$

where

$$\xi = y/\delta(z).$$

Equation 5.3 can then be rewritten as

$$ReSc\left(-\frac{\delta^3}{2}\frac{\partial\dot{\gamma}}{\partial z} - \dot{\gamma}\delta^2\frac{\partial\delta}{\partial z}\right)\xi^2\frac{\partial\Pi}{\partial\xi} = \frac{\partial^2\Pi}{\partial\xi^2}. \tag{5.4}$$

If

$$ReSc\left(-\frac{\delta^3}{2}\frac{\partial\dot{\gamma}}{\partial z} - \dot{\gamma}\delta^2\frac{\partial\delta}{\partial z}\right) = -3, \tag{5.5}$$

equation 5.4 reduces to

$$-3\xi^2\frac{\partial\Pi}{\partial\xi} = \frac{\partial^2\Pi}{\partial\xi^2} \tag{5.6}$$

with $\delta = 0$ at $z = z_0$ and the boundary conditions reduce to

$$\begin{array}{ll} \Pi = 0 & \xi = 0 \\ \Pi = 1 & \xi = \infty. \end{array}$$

The solution to equation 5.5 is

$$\delta = \frac{1}{\sqrt{\dot{\gamma}(z)}} \left(\frac{9}{ReSc} \int_{z_0}^{z} \sqrt{\dot{\gamma}(z)} dz^* \right)^{1/3}$$

and the solution to equation 5.6 is

$$\Pi = \frac{1}{\Gamma(4/3)} \int_0^{\xi} e^{-\nu^3} d\nu. \tag{5.7}$$

The local Nusselt number is defined as

$$Nu_{loc}(z) = \frac{d\Pi}{dy}|_{y=0} \tag{5.8}$$

and equals

$$Nu_{loc} = \frac{(ReSc)^{1/3}}{9^{1/3}\Gamma(4/3)} \frac{\sqrt{\dot{\gamma}(z)}}{\left[\int_0^z \sqrt{\dot{\gamma}(s)} ds\right]^{1/3}} \tag{5.9}$$

where Re is the Reynolds number. The empirical generalization of Equation 5.9 is

$$Nu_{loc} = g(geometry, Re) Re^c Sc^{1/3}.$$

The function g is typically only a weak function of the Reynolds number and is often taken to be independent of it. The Reynolds number exponent, c, depends on the flow conditions and is 1/3 for creeping flows ($Re \approx 0$) and 1/2 for most laminar boundary layer flow systems ($Re \gg 1$). The average Nusselt number, Nu_{avg}, is found by integrating the local Nusselt number over the desired length and dividing by that length.

5.2 Flat Velocity Profile (Penetration Theory)

When the velocity is approximately constant across the boundary layer, at the boundary

$$v_z = u_0(z)$$

so equation 5.1 reduces to

$$v_y = -\frac{\partial u_0}{\partial z} y.$$

Equation 5.2 then becomes

$$-ReSc\left(u_0\delta\frac{\partial\delta}{\partial z} + \delta^2\frac{\partial u_0}{\partial z}\right)\xi\frac{\partial\Pi}{\partial\xi} = \frac{\partial^2\Pi}{\partial\xi^2} \tag{5.10}$$

where again $\xi = y/\delta(z)$. The boundary conditions require that at

$$\Pi = 0 \quad \xi = 0$$

$$\Pi = 1 \quad \xi \to \infty$$

$$\Pi = 0 \quad z = z_0.$$

When

$$ReSc\left(u_0\delta\frac{\partial\delta}{\partial z} + \delta^2\frac{\partial u_0}{\partial z}\right) = 2$$

then

$$\delta = \frac{2}{\sqrt{ReSc}}\frac{\sqrt{\int_{z_0}^{z} u_0 dz^*}}{u_0}.$$

and the solution to equation 5.10 is

$$\Pi = \operatorname{erf}(\xi) = \frac{2}{\sqrt{\pi}}\int_0^{\xi} e^{-\nu^2} d\nu$$

so that the local Nusselt number is

$$Nu_{loc} = \left(\frac{ReSc}{\pi}\right)^{1/2} \frac{u_0}{(\int_{z_0}^{z} u_0(s)ds)^{1/2}} \tag{5.11}$$

which is often generalized to the empirical equation

$$Nu_{loc} = h(geometry, Re)Re^c Sc^{1/2}.$$

The function h is again typically only a weak function of the Reynolds number and is often taken to be independent of it.

The average Nusselt number, Nu_{avg}, is found by integrating the local Nusselt number over the desired length and dividing by that length. Since Taylor-Couette flow is periodic, the desired length here is the width of one vortex, which is approximately the gap width since the vortices are approximately square. Furthermore, since the flow is symmetric, the average Nusselt number for a vortex with clockwise rotation equals that of its axial neighbor with counter-clockwise rotation. The Peclet number is consistent with the scaling in the linear stability analysis $Pe = ReSc = \Omega_1 R_1 d/D_2$.

Chapter 6

Experimental Design

6.1 Equipment Design

The experimental apparatus, illustrated in Figures 6.1 and Figures 6.2, consists of a pair of horizontal coaxial cylinders with a weir system for countercurrent flow. The fluids must be added or removed from cylinder annulus while the cylinders rotate at a speed sufficient for centrifugal stratification, thus in effect creating an air seal. The sealless design offers the advantages of mechanical simplicity and easy access to the fluid filled annulus. The disadvantage is that experiments with very slowly rotating cylinders are not possible. This type of operation, however, is not of interest here.

The inner and outer cylinder rotation rates are independently controlled by two Compumotor stepper motors and drivers (Triphase Automation, Waukesha, WI). The larger motor (OEM-83-62) is directly coupled to the inner cylinder and the smaller motor (OEM-57-83) belt drives the outer cylinder. The motors are powered in series and controlled through two Compumotor OEM650X-M2-RC

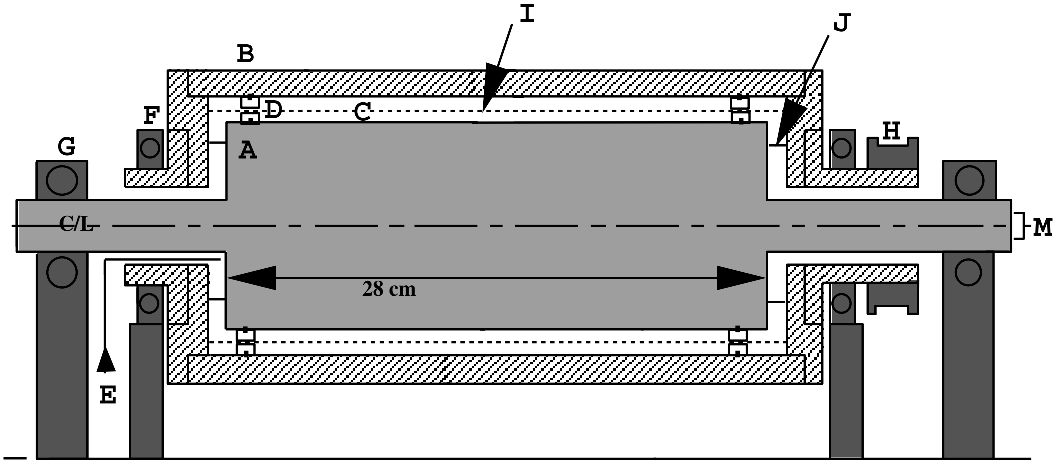

A – Aluminum inner cylinder (R1 = 4.2 cm)
B – Plexiglas outer cyinder (R2 = 5.1 cm)
C – Fluid filled gap (d = 0.9 cm)
D – Double end spacers
E – Fluid fill/empty tubing
F – Outer cylinder bearing
G – Inner cylinder pillow block bearing
H – Belt coupling to outer cylinder motor
I – Liquid−liquid interface
J – Liquid−air interface
M – Direct coupling to inner cylinder motor

Figure 6.1: The equipment design without the weir system.

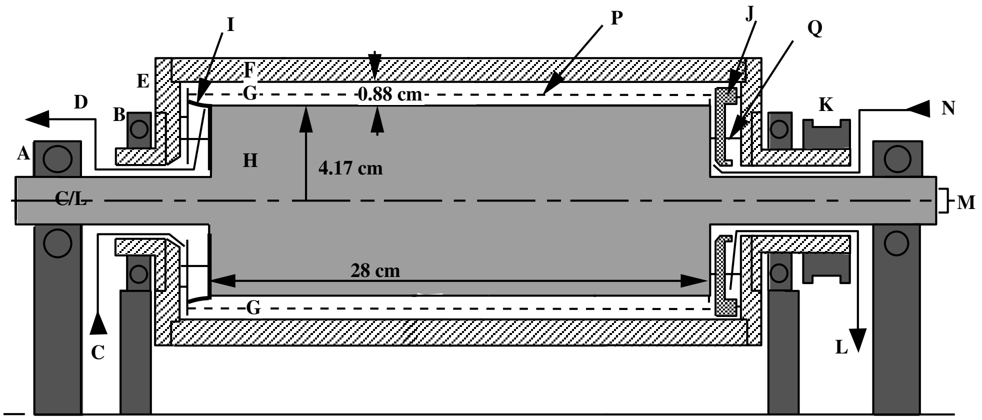

A – Inner cylinder pillow block bearing
B – Outer cylinder bearing
C – Heavy fluid inlet
D – Light fluid outlet
E – Plexiglas endplate with removable windows
F – Plexiglas outer cylinder Ri = 5.05 cm
G – 0.88 cm fluid filled gap
H – Stainless steel inner cylinder Ro = 4.17 cm
I – Underflow weir
J – Overflow weir
K – Flat belt coupling to outer cylinder motor
L – Heavy fluid outlet
N – Light fluid inlet
M – Direct coupled inner cylinder motor
P – Fluid–fluid interface
Q – Fluid–air interface

Figure 6.2: The equipment design with the weir system.

drivers with position controllers (25,000 steps/rev). The drivers are controlled from a PowerMac through a Zterm interface.

The outer cylinder is cast Plexiglas with inner diameter 10.098 ± 0.008 cm. The choice of the inner cylinder depends on the experiment: (1) a polished aluminum cylinder (diameter 8.349 ± 0.003 cm) is used for experiments without axial flow (2) a polished stainless steel cylinder (diameter 8.349 ± 0.003 cm) with a weir system is used for experiments with axial flow. The weir system is discussed in more detail below. The coaxial alignment of the two cylinders was measured and optimized through small removable, liquid-tight windows in the endplates attached to the outer cylinder. A telescoping gauge and micrometer were used to measure the gap thickness at three locations on each end. The alignment of the two cylinders is such that the gap on either end is 0.882 ± 0.017 cm (± 2%). This variation in the gap width is not expected to have a significant effect on the flow field [66, 112]. Measuring the alignment is possible only without the weirs and is assumed to be representative with the weirs. The annulus length is $Z = 29.5$ cm for an aspect ratio of $Z/d = 33.5$.

Without the weir system, three types of end spacers were investigated to minimize end effects: single spacers, double spacers, double-holed double spacers. The first pair of end spacers (single spacers) fit inside the outer cylinder with one spacer per end and were held in place by Viton O-Rings as illustrated in Figure 6.3. Each spacer reached within approximately a millimeter of the inner cylinder. This gap was required for filling, emptying, and removing air bubbles.

The second set of end spacers was a pair of spacers; one pair for each end. Of each pair, one spacer fit on the inner cylinder and one in the outer cylinder. Both were held in place by Viton O-ring segments. The gap between the pair of spacers was approximately half a millimeter and was located near the interface position. Four half-moons ($\frac{1}{2}$ cm in diameter) were cut in the inner spacer next to the inner cylinder for filling, emptying, and removing air bubbles. These double spacers provide a first approximation to a continuous transition between the inner and outer cylinder rotation rates. The double-holed double spacers closely resemble the double spacers, but with an additional four half-moons cut in the outer cylinder spacer next to the outer cylinder as depicted in Figure 6.4. This allowed aqueous injections during the cylinder operation and created symmetric end conditions for the two phases. The double-holed double spacers best minimized end effects.

For experiments with axial counterflow, the end spacers could not be installed effectively due to the weirs and therefore were not used. As a result, a wide variety of weir configurations were evaluated to reduce end effects. When the cylinders rotate at different speeds, structures that are attached to the inner cylinder (1) are coated with a film of light fluid and (2) provide strong outward radial pumping action of the light fluid that can strongly affect the interface

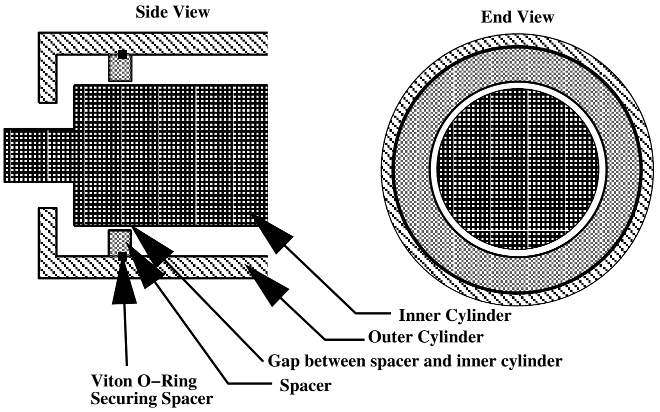

Figure 6.3: Illustration of the single spacers.

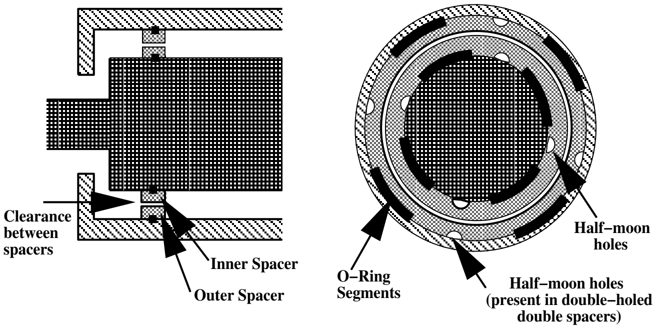

Figure 6.4: Illustration of the double-holed double spacers.

position. In contrast, structures that are attached to the outer cylinder introduce an opposite effect and heavy fluid can be drawn radially inward. Ultimately, the weir configuration illustrated in Figure 6.2 was chosen.

The light fluid inlet/heavy fluid outlet weir consists of:

1. a heavy fluid overflow weir attached to the outer cylinder. When this weir is attached to the inner cylinder, the above mentioned pumping action causes light fluid carryover into the heavy fluid outlet stream.
2. a small plate attached to the inner cylinder that has a slightly larger diameter than the inner cylinder. The plate diameter controls the interface position at this end and light fluid feed is introduced against this plate.

The heavy fluid inlet/light fluid outlet weir consists of:

1. a plate attached to the outer cylinder that has a slightly smaller diameter than the outer cylinder. Heavy fluid is introduced against this plate. When this plate is attached to the inner cylinder the resulting pumping action can cause light fluid carryover into the heavy inlet reservoir and severe mixing.
2. an underflow weir attached to the inner cylinder. This weir is a modified N-buna flared piston cup which also acts as a crude rotary seal against the heavy inlet plate to prevent heavy fluid that is drawn radially inward from entering the light fluid outlet reservoir.

The apparatus remains horizontal and the axial counterflow is driven by the axial pressure drop for the respective phase. As a result, the interface is slightly tapered rather than cylindrical. A perturbation analysis from section 3.1 reveals that at rigid rotation the maximum taper is approximately

$$\frac{\delta}{d} = \frac{4\Gamma R_{12} Re_{ax,2} Ek_2^2}{(1-\rho_{12})} \left(\mu_{12}^2 \rho_{21} \frac{Re_{ax,1}}{Re_{ax,2}} + 1 \right).$$

For the results presented here, $\delta/d < 0.03$ with $\Gamma = 6$.

In addition to the weir system, a bulk reservior and pumping accessories were required for countercurrent axial flow. To maintain a steady-state interface position in the annulus, the inlet flowrate has to precisely match the outlet flowrate for each phase. For the aqueous phase this was accomplished by using a liquid full reservior system consisting of a collection bag contained in a large flask. As the aqueous outlet flow was collected in the bag, the bag expanded, and caused fresh fluid surrounding the bag out of the flask, thus providing an inlet flow matched to the outlet flowrate. For the organic phase, however, the collection bag system was abandoned because the organic phase would leach plasticizer from the bag, interfering with the UV measurements. Instead a two flask system was used with an aqueous seal fluid. For the same reason, the organic fluids were stored in glass or coated metal containers and special Tygon (F-4040-A) or Viton tubing was used for all of the light fluid lines.

The pumping system was further simplified by only considering equal flow rates of the heavy and light fluids. Therefore only one Masterflex peristaltic pump was required with two coupled pump heads (one pump head for each phase). The flow rates were calibrated and controlled by the rotation rate of the pump head.

6.2 Experimental Techniques

6.2.1 Fluids Used in the Experiments

The physical properties of the fluids investigated are summarized in Table 6.1. The aqueous phase was glycerine in water and the organic phase was white mineral oil (Drakeol-35, Superior Lubricants, Tonawonda, NY) in kerosene (Middleton Farmer's Market, Middleton, WI). For the extraction and dispersion experiments a hydrotreated petroleum distillate (Isopar-L, Famous Lubricants, Chicago, IL) was used in place of kerosene (noted by -IL in Table 6.1) to provide an organic phase background with less UV absorbance. The kinematic viscosities were measured at 25°C on a Schott Geräte capillary viscometer calibrated with sucrose solutions. The densities were measured at room temperature on an Aton Parr DMA40 digital density meter calibrated with water and air. The dynamic viscosity was calculated from the measured values for density and kinematic viscosity.

Pair	Nominal wt. % glycerine	Nominal wt. % Drakeol-35	μ_2 (cp)	ρ_2 (g/ml)	μ_{21}	ρ_{21}	Barber Pole Obs
1	0	0	1.00	1.00	0.63	1.24	BP
2	15	23	1.42	1.03	0.44	1.26	BP
3	30	80	2.07	1.06	0.06	1.23	
4	30	60	2.05	1.07	0.18	1.25	BP
5	30	42	2.08	1.06	0.37	1.27	BP
6	30	0	2.08	1.07	1.33	1.32	BP
7-IL	60	80	7.52	1.15	0.22	1.36	
8-IL	60	60	7.52	1.15	0.63	1.40	
8	60	60	7.52	1.15	0.69	1.35	
9-IL	60	50	7.52	1.15	0.96	1.40	
9	60	50	7.52	1.15	1.01	1.36	
10-IL	60	40	7.52	1.15	1.46	1.43	
11-IL	60	0	7.52	1.15	4.85	1.50	
12	60	42	7.52	1.15	1.39	1.37	
13	70	42	13.57	1.17	2.43	1.40	
14	70	0	13.57	1.17	7.98	1.44	BP
15	70	60	14.00	1.18	1.22	1.39	
16	85	0	47.37	1.21	28.48	1.49	

Table 6.1: Physical properties of the fluids used in the experiments. IsoPar-L was used for the pairs identified as “-IL”; otherwise kerosene was used. The interfacial tension is approximately $S = 50$ dyne/cm. The barber pole pattern is observed with the fluid pairs identified “BP”.

6.2.2 Optics and Flow Visualization

Flow visualization was the primary technique in the fluid mechanics experiments to determine the onset of two-fluid Taylor-Couette flow. In addition, flow visualization was a powerful tool for optimizing the weir system. Several methods are available and include: anisotropic flakes, Laser Induced Fluorescence (LIF), and dye tracer experiments.

Small reflective anisotropic particles (such as Kalliroscope, titanium dioxide coated mica flakes, and stearic acid treated aluminum powder) align with flow, and light reflectance off the particles makes the flow field visible. The particles preferentially disperse in one phase: Kalliroscope and mica prefer the water phase; whereas aluminum and hydrophobic mica prefer the organic phase. At high concentrations the particles create an opaque and highly light scattering solution.

Kalliroscope. The small size (6x30x0.07 microns) and density (1.620 g/ml) of Kalliroscope (Kalliroscope Corporation, Groton, MA) [80] allows it to remain suspended in the glycerine solution, even under a strong centrifugal force, for several hours or the duration of an experiment. The gravitational settling time is estimated at 0.1 cm/h in water. In vertical Taylor-Couette experiments this rate of settling can effect the wavelength of the vortices over long times; the wavelength at the top of the cylinders increases relative to that at the bottom.

There is no effect in horizontal Taylor-Couette experiments [26]. As a biological product derived from guanine, Kalliroscope requires a biocide additive for extended use in solution. The effect of this additive on the fluid dynamics experiments is unclear. Kalliroscope also tends to form a film on the cylinders and physically sticks to the cylinders at the Taylor vortex boundaries after some time. Nonetheless, Kalliroscope is the preferred anisotropic flake for water phase flow visualization.

Titanium Dioxide Coated Mica Flakes. Coated mica flakes (Kalliroscope Corporation, Groton, MA) are approximately the same dimensions of Kalliroscope (4x32 microns), but have significantly higher density (3.1 g/ml). This high density is undesirable in the water/glycerine solutions under strong centrifugal forces. Similarly, if the mica flakes are treated to be hydrophobic, their high density causes them to collect on the hydrocarbon side of the interface.

Hydrophobic Aluminum Flakes. Stearic acid treated aluminum flakes (Alcan ATA 7300 Leafing Flake, Alcan-Toyo America, Inc., Lockport, IL) consistently prefers the hydrocarbon phase. The particle size (5x30x0.2 microns) is similar to Kalliroscope, but again with a higher density (2.62 g/ml). At rigid rotation, the treated aluminum flakes collect at the hydrocarbon side of the interface. As the relative rotation rate is increased, they are slowly drawn to the vortex boundaries and, once vortices form, are swept off the interface. Aluminum flake is preferred for hydrocarbon phase flow visualization.

Bulk dying of one phase allows any waviness in the interface to be visually observed as the color intensity of the fluid is related to the fluid depth. Pulsed injections of dye reveal information about the diffusion, convection, and end effects of the flow field. For interface visualization, the bulk dye may be chosen to be a Laser Induced Fluorescent (LIF) dye selective to one phase. With exposure to laser light, the LIF dye will fluoresce at a wavelength higher than the wavelength of the laser. By wavelength filtering or by visual observation, the LIF dyed phase appears as a solid color corresponding the fluorescing wavelength; the undyed phase remains clear. Excimer Oxazine 720 Chloride (Exciton, Inc., Dayton, OH) is a suitable LIF dye for HeNe lasers and is also selectively soluble in the water phase for short times (on the order of a day).

The 8mW HeNe laser light (Melles Griot) is formed into a laser sheet by a simple 60 degree line generating rod shaped cylindrical lens (Edmund Scientific). This lens expands the laser beam in one direction only, while the other direction retains the divergence characteristics of the laser. When the laser sheet is aligned with the axis of the cylinders, the interface is clearly visible. Without calculation of the actual optical path, the interface amplitude is only qualitatively determined. The interface wavelength, however, can be quantitatively

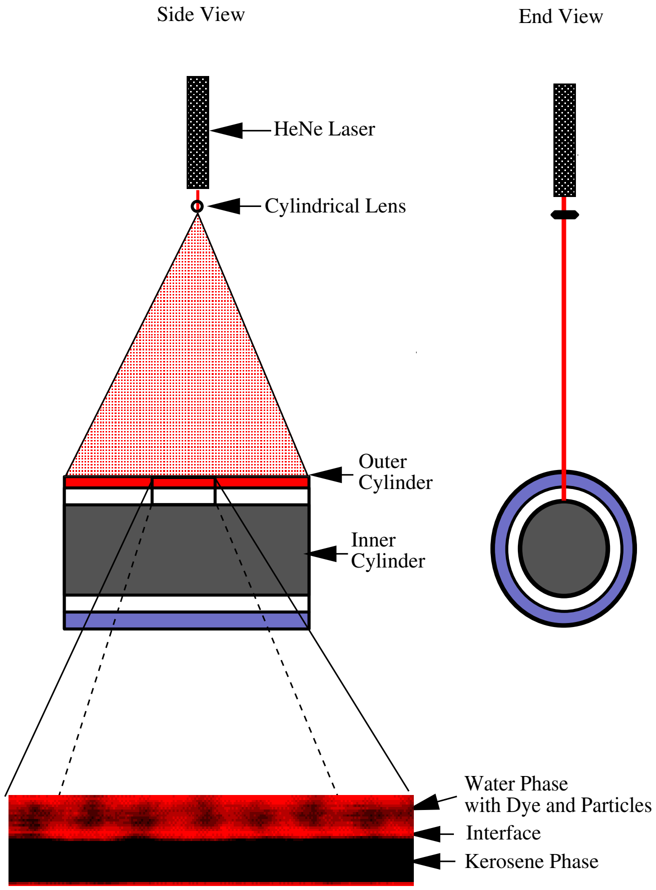

Figure 6.5: The optics for characterization of the interface using Laser Induced Fluorescence.

determined. With the addition of anisotropic flakes, qualitative detail about the fluid motion is also obtainable. Figure 6.5 illustrates the optics configuration for the interface characterization.

For a permanent record of the interface behavior, the interface highlighted by the laser sheet was videotaped with a betacam recorder. Specific still shots could then be frame grabbed and processed. The Silicon Graphics software Image Works was used to enhance the still frames.

6.2.3 Axial Dispersion and Extraction Experimental Design

For the mass transfer experiments a tracer was injected into an inlet stream and the outlet streams monitored. The properties of the various tracers are summarized in Table 6.2. For the dispersion experiments, the tracer is soluble only one phase. For the extraction experiments, the tracer is soluble in both phases as defined by the partition coefficient

$$m = \frac{C_2^*}{C_1^*}$$

where C_1^* and C_2^* are the equilibrium concentrations of the tracer in the light and heavy phases, respectively. The partition coefficient was measured spectroscopically and determined to be independent of the composition of the organic and aqueous phases for the ranges investigated. The outlet streams were both monitored with a Beckman DU65 UV-VIS Spectrophotometer using quartz flow-through cells (Fisher Scientific) and a multisample scanning system. Upstream of the light fluid UV cell was a small knock-out pot to prevent any small amount of heavy fluid carryover from collecting in the light fluid UV cell. The spectrophotometer was calibrated with standard samples of each tracer at the typical concentrations and flowrates of the experiments. The readings from the spectrophotometer were recorded to a PowerMac through a Kermit interface. Data analysis was done in Mathematica.

For all of the mass transfer experiments the volumes of the two phases were matched ($V_1 = V_2 = 400$ ml). After each series of runs, the fluid volumes collected from the annulus were measured and determined to be withing 10% of the initially loaded volume for each phase. Likewise, the volumetric flow rates were matched and were typically $Q_1 = Q_2 = 20$ ml/min for twenty minute average residence time with $Re_{ax,2} = 0.33$. The inner cylinder rotation rate, Ω_1, was constant at 12.5 rev/s, and the outer cylinder rotation rate, Ω_2, was varied from 7.5 to 12.5 rev/s. Lower values of Ω_2 would result in emulsion formation at the ends, and therefore were not pursued.

Axial Dispersion Experiments. Axial dispersion is characterized by the change in the tracer concentration curve from the inlet injection to the outlet response. When the injection of tracer is assumed to be an instantaneous pulse, as the experiments tried to achieve, the extent of axial dispersion is determined only by the shape of the outlet response curve, $C(t)$. This curve can be characterized by its moments:

$$M_0 = \int C(t)dt$$

$$M_1 = \frac{1}{M_0}\int tC(t)dt$$

$$M_2 = \frac{1}{M_0}\int (t - M_1)^2 C(t)dt.$$

The zeroth moment, M_0, is used for a mass balance on the tracer. The first moment, M_1, reflects the average residence time and with the second central moment, M_2, determines the dispersion.

Several models are available to describe axial dispersion. The simplest continuous model is simply

$$\frac{\partial < C >}{\partial t} + \bar{W}\frac{\partial < C >}{\partial z} = D^* \frac{\partial^2 < C >}{\partial z^2}$$

where D^* is an empirical dispersion coefficient and the angle brackets denote averages across the fluid layer [73]. This dispersion model is preferred when the outlet curves are Gaussian since its impulse response is Gaussian. Alternatively, the dispersion can be represented by a series-of-mixing-tanks model with the extent of dispersion corresponding to the number of mixing tanks. In this case the outlet concentration is

$$C(t) = \frac{N(N\Theta)^{N-1}}{(N-1)!}e^{-N\Theta}$$

where $\Theta = t/M_1$. The number of mixing tanks can be calculated by

$$N = \frac{M_1^2}{M_2}.$$

In this case, fewer mixing tanks indicate higher dispersion. The mixing tank model better represents situations where the output curve is not Gaussian [73]. For this study, the dispersion is better described by the mixing tank model and Figure 6.6 shows typical outlet response curves for pulse input. The number of mixing tanks was determined by first fitting the outlet response data with a Fourier series to reduce the contribution of noise. This curve was then integrated to find the moments and to characterize the dispersion. The mass balance and the average residence time were typically within 10% of the expected values.

Extraction Experiments. The extraction experiments consisted of injecting a pulse of tracer into the inlet stream of one phase and measuring its concentration in the outlet streams of both phases. Typically the tracer was introduced into the light stream and was therefore premixed with light fluid to provide a more homogeneous injection. Figure 6.7 shows a pair of typical outlet response curves for a pulse input. The extraction performance was determined by first fitting the outlet response data with a Fourier series to reduce the contribution of noise. The two outlet curves were then integrated to find the zeroth moment for each phase. A total mass balance and the percent of tracer extracted were then calculated. The mass balance was typically satisfied within 10%.

The overall mass transfer coefficient is defined by the one dimensional differential mass balance equation along the length of the extractor

$$u_{z,1} dC_1(z) = (aK_1)[C_1^*(z) - C_1(z)]dz \tag{6.1}$$

where $u_{z,1}$ is the linear velocity of the the light phase, C_1 is the concentration in the light phase, C_1^* is the concentration in the light phase that would be in equilibrium with the concentration in the heavy phase, a is the mass transfer surface area per unit volume, and K_1 is the overall mass transfer coefficient based on the light phase. The mass transfer area is usually unknown in systems that disperse one phase in the other. Here, however, the interfacial area per unit volume can be accurately calculated from the FIDAP runs. Since the interface deformation is small, the interfacial area may also be well estimated by assuming a cylindrical interface with radius R_i, so $a = 2R_i/(R_2^2 - R_1^2)$. This overall mass transfer coefficient is a sum of the individual mass transfer coefficients, which typically cannot be measured directly;

$$\frac{1}{K_1} = \frac{1}{k_1} + \frac{1}{mk_2}$$

where k_1 and k_2 are the individual mass transfer coefficients for the light and heavy phases, respectively. This definition of the mass transfer coefficient also includes the effects of dispersion; higher rates of dispersion result in lower mass transfer coefficients. Equation 6.1 can be integrated to find the mass transfer coefficient

$$aK_1 = \frac{u_{z,1}m}{(1-m)Z} ln \frac{(1-f)}{(1-f/m)} \tag{6.2}$$

where m is the partition coefficient, Z is the axial length of the extractor, and f is the fraction extracted as determined experimentally. The Nusselt number, Nu, is the dimensionless mass transfer coefficient $Nu = K_1 d/D_2$.

The number of theoretical stages, n, is the number of equilibrium batch separations that would be required to obtain a given separation and is calculated from the equation

$$n = \frac{ln \frac{E-f}{E(1-f)}}{lnE} \tag{6.3}$$

where $E = mQ_2/Q_1$ and Q_1 and Q_2 are the volumetric flowrate of the light and heavy phases, repectively [111]. The higher the number of theoretical stages, the better the separation.

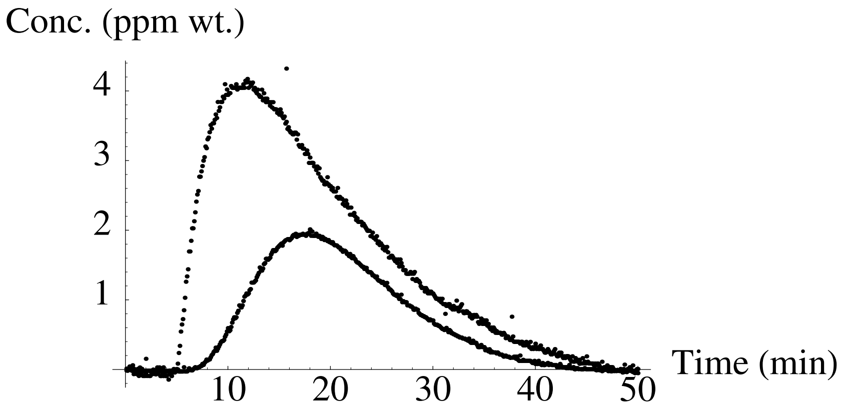

Figure 6.6: Typical outlet response curves for the axial dispersion experiments. The more symmetric (lower) curve corresponds to a higher number of mixing tanks, and in this case, the light phase. The other curve is for the heavy phase. $\Omega_{21} = 0.696$, $\Omega_{21,c} = 0.725$, $\mu_{21} = 1.46$, $Re_{ax,2} = 0.33$, $N_1 = 8.8$, $N_2 = 4.5$

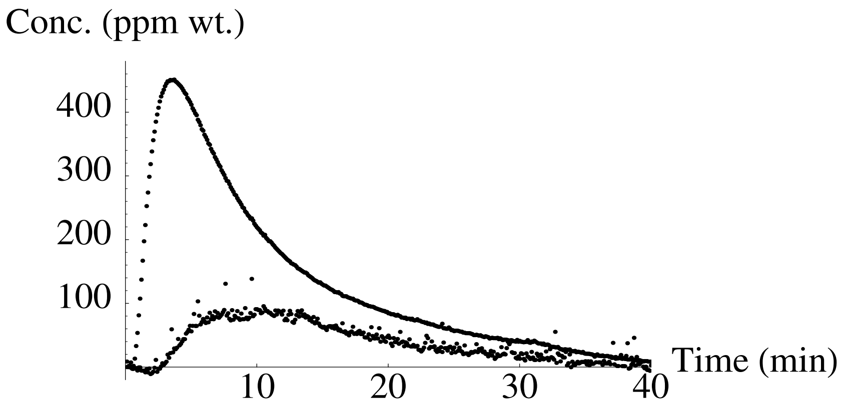

Figure 6.7: Typical outlet response curves for the extraction experiments. The upper curve corresponds to the extract (heavy) phase, the lower curve the raffinate (light) phase. $\Omega_{21} = 0.6$, $\Omega_{21,c} = 0.687$, $\mu_{21} = 0.96$, $Re_{ax,2} = 0.33$, $m = 2.7$, $f = 0.78$, $Nu = 440$.

Tracer	Partition Coefficient, m	Experiment	Monitoring Wavelength (nm)
Acetophenone	0.125	Extraction	255
sec-Phenethyl Alcohol	2.7	Extraction	255
Benzyl Alcohol	14.0	Extraction	258
Sudan-IV	0	Dispersion	520
Amarath Red	∞	Dispersion	520

Table 6.2: Properties of the tracers used in the axial dispersion and extraction experiments.

6.3 Experimental Results and Comparison with Theory

6.3.1 Fluid Mechanics

One fluid Taylor-Couette Flow. One fluid Taylor-Couette flow at high rotation rates was reproduced with the experimental apparatus. At high rotation rates, the one fluid theory predicts an asymptote corresponding to the inviscid Rayleigh solution $\Omega_2 = \Omega_1 R_{12}^2$. The experimental results for a 60 wt.% glycerine solution confirmed the Rayleigh asymptote is achieved as shown in Figure 6.8. Figure 6.9 is a photograph of one fluid Taylor-Couette flow at high rotation rates.

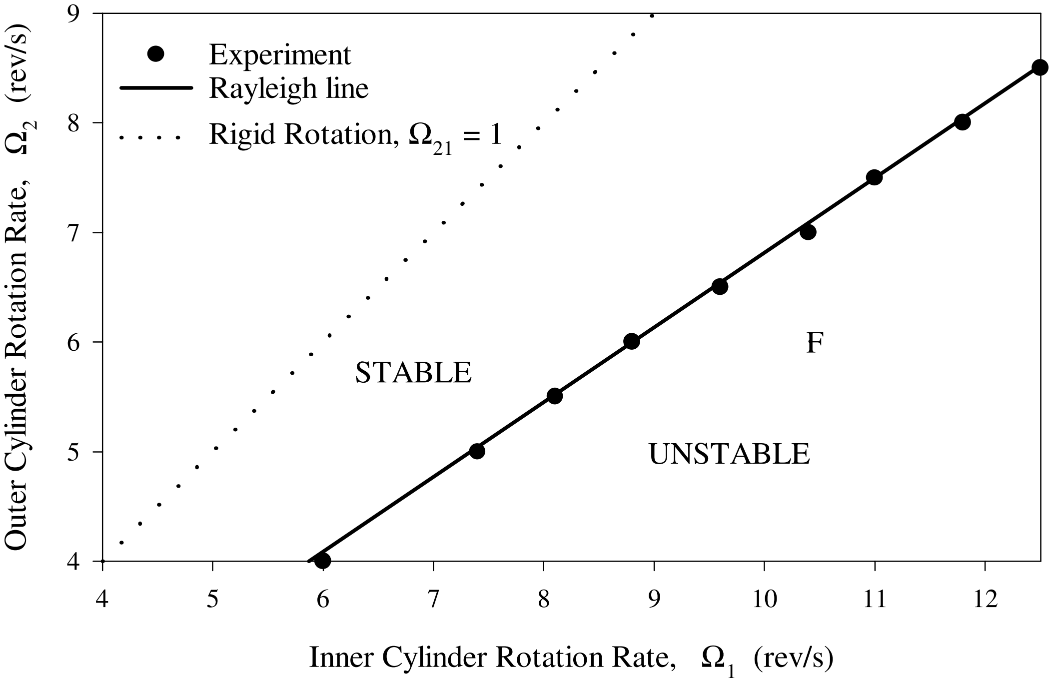

Figure 6.8: A comparison of the experimentally observed onset of one fluid Taylor-Couette flow and the Rayleigh asymptote. 60 wt% glycerine in water. The point marked F correponds to the FLUENT calculation point of Figure 4.1.

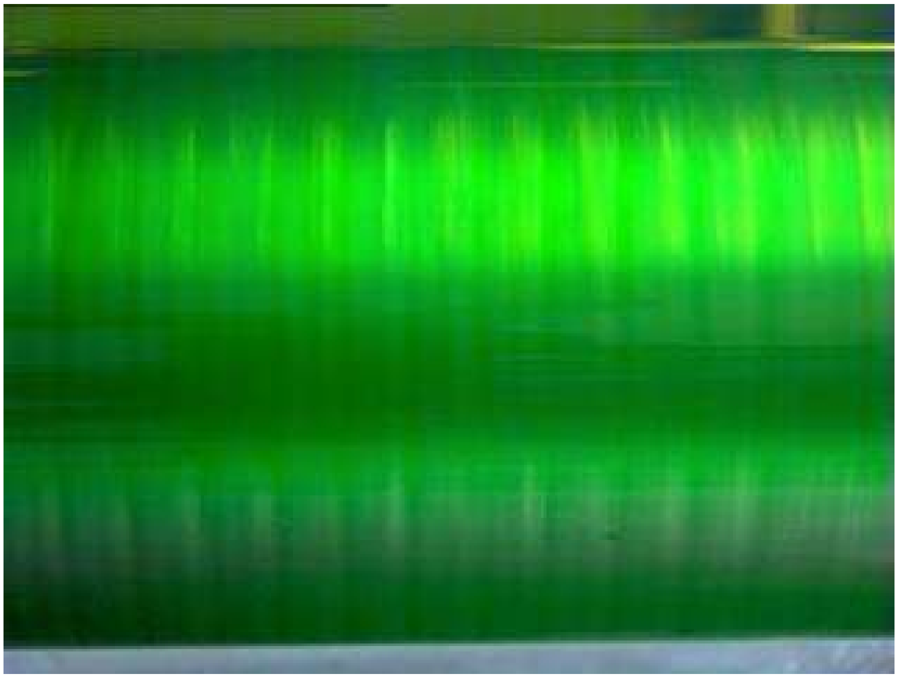

Figure 6.9: Photograph of one fluid Taylor-Couette flow at high rotation rates. 60 wt% glycerine in water.

Two-Fluid Couette Flow - the Barber Pole Pattern. When the gap is filled with two “low” viscosity fluids, a new flow pattern appears that is not predicted by the two-fluid Taylor-Coeutte analysis or by Joseph’s prediction of the interface behavior. At rigid rotation a wavy interface is observed at the lower rotation rates. When the inner cylinder is rotated faster than the outer cylinder two patterns can occur, either (1) at low outer cylinder rotation rates a time-dependent non-axisymmetric pattern (the barber pole), or (2) at high outer cylinder rotation rates a rippled interface that may correspond to very irregular Taylor vortices. In all cases, the fluids continue to be stratified over the length of the cylinders without breakthrough of the interface to touch either cylinder. Since the wavelength of the rigid rotation wavy interface and the barber pole pattern is significantly longer than that predicted for two-fluid Taylor-Couette flow, it appears to be quite dissimilar from two-fluid Taylor-Couette flow. At extreme inner cylinder rotation rates relative to the outer cylinder rotation rate, a loose emulsion forms, beginning at the ends.

The front and interface views of the fully developed barber pole pattern are shown in Figures 6.10 and 6.11. The fluid pairs for which the barber pole pattern is observed are listed in Table 6.1 and the experimental observations of the barber pole pattern and the wavy interface are summarized in Figure 6.12. As seen in Figure 6.12, the end conditions can influence the onset of the barber pole; however, a wavy interface is still observed at rigid rotation where

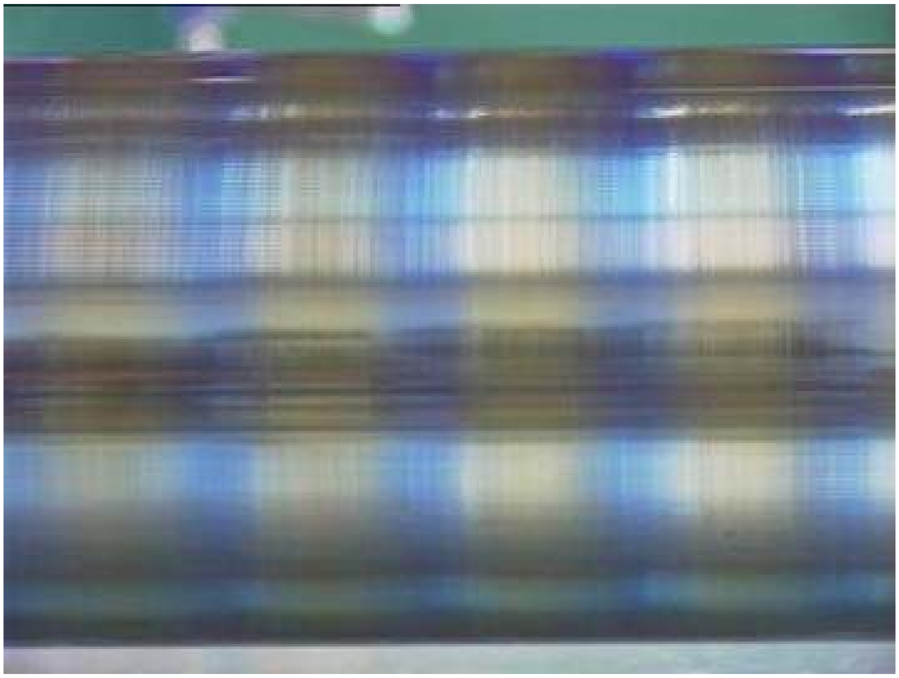

Figure 6.10: Photograph of the barber pole flow pattern. The fluids are equal volumes of water and kerosene.

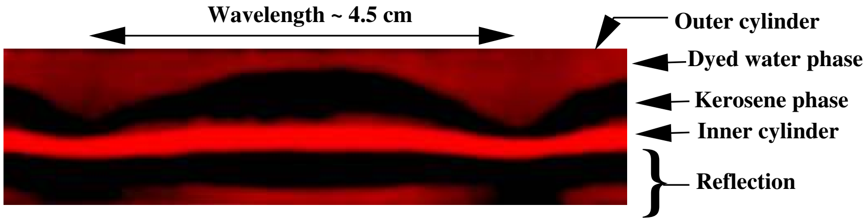

Figure 6.11: The barber pole pattern interface as highlighted by Laser Induced Fluorescence. The red region is the dyed aqueous phase and the black region is the undyed organic phase. The fluids are equal volumes of water and kerosene.

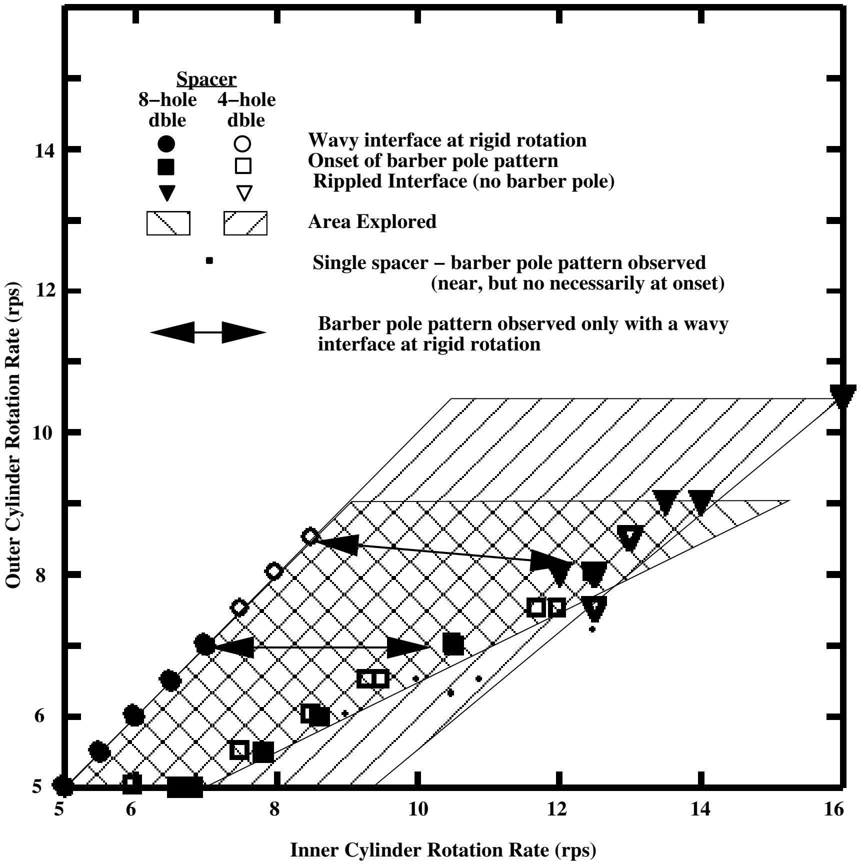

Figure 6.12: The experimental observations of the barber pole pattern including the effect of the type end spacer. The fluids are equal volumes of water and kerosene.

end effects are not important. This suggests that the barber pole pattern is influenced by, but not a result of, end conditions.

For these low viscosity pairs $J_2 > 100$. By Joseph's analysis when $J_i > 4$, surface tension effects are unimportant in the absence of gravity and a rigid interface is predicted, not the wavy interface that is observed. Therefore, the effect of surface tension on the barber pole pattern was investigated with some preliminary experiments. Two fluid pairs were prepared: (1) 15 wt.% glycerine in water and 23 wt.% Drakeol-35 in kerosene (2) water and butanol. For these pairs it was possible to match viscosities, while having significantly different interfacial tensions. The physical properties of these pairs are recorded in Table 6.3. The barber pole pattern for these pairs had no qualitative differences, although there were some quantitative differences. At rigid rotation at 300 rpm or less, a steady, wavy interface was found for both fluid pairs. The interface deformation was larger, however, for the high interfacial tension pair. This discrepancy in deformation amplitude persisted as the inner cylinder rotation rate was increased. The wavelength of the deformations was also consistently slightly shorter for the low interfacial tension pair; for example, at $\Omega_1 = 560$ rpm and $\Omega_2 = 330$ rpm, the low interfacial tension pair exhibited 11 wavelengths over the 29.5 cm length of the cylinders, while the other pair exhibited 10. Finally, the transition to time-dependence at a fixed outer cylinder rotation rate always occurred at a lower inner cylinder rotation rate for the low tension pair than the high.

In summary, the experimental factors that most affect the barber pole are viscosity, rotation rate, and to a smaller extent, interfacial tension. When combined, these factors have been observed to lead to interesting behavior in a single layer of liquid coating the inner surface of a rotating cylinder, sometimes called "rimming flow". Experimental observations have shown that at steady state, the two-dimensional film can have significant azimuthal variations in thickness and can become unstable to three-dimensional perturbations. Hosoi and Mahadevan have derive an evolution equation for the dynamics of the interface in an asymptotic limit where effect of inertia, capillarity, viscosity, and gravity are all retained. Using this equation, they find the azimuthal film profile and show that it can become unstable at sufficiently small rotation rate, and furthermore that the axial wavelength at instability increases with increasing surface tension [47]. Both of these trends are consistent with the above experimental results, which suggest the barber pole pattern is an analogue to the instability of single phase rimming flow.

Pair	μ_2 (cp)	ρ_2 (g/ml)	μ_{21}	ρ_{21}	I.T. (dyne/cm)
kerosene-water	1.42	1.03	0.44	1.26	50
butanol-water	1.43	0.99	0.44	1.17	8

Table 6.3: Physical properties of the fluids used in the barber pole experiments testing the effect of interfacial tension.

Two-Fluid Taylor-Couette Flow. As either the outer cylinder rotation rate or the viscosity of one of the fluids is increased, the barber pole pattern is suppressed and two-fluid Taylor-Couette flow appears. In the transition region a wide variety of flows patterns are possible, which include stratified two-fluid Couette flow, the barber pole, two-fluid Taylor-Couette flow, a combination of the barber pole and two-fluid Taylor-Couette flow. At the onset of two-fluid Taylor-Couette flow, the interface is visually flat and the wavelength of the vortices is very close the theoretically predicted value of twice the fluid depth. Figure 6.13 is a photograph of two-fluid Taylor-Couette flow near the onset. The approximately square vortices and a flat interface are visible in Figure 6.14. As the inner cylinder rotation rate is further increased, the vortices become stronger and the interface deforms with the wavelength of the vortex flow (Figure 6.15). At even higher Taylor numbers, the vortices become time dependent and erratically translate back and forth in the axial direction. At extreme Taylor numbers, an emulsion is formed, beginning at the ends, as a result of the very strong interface deformation and the mixing created at the ends. The higher modes of instability of the one fluid problem at low rotation rates (such as wavy or feathery (turbulent) vortices) were not visually apparent in these two-fluid experiments.

The experimentally observed onset of two-fluid Taylor-Couette flow and the

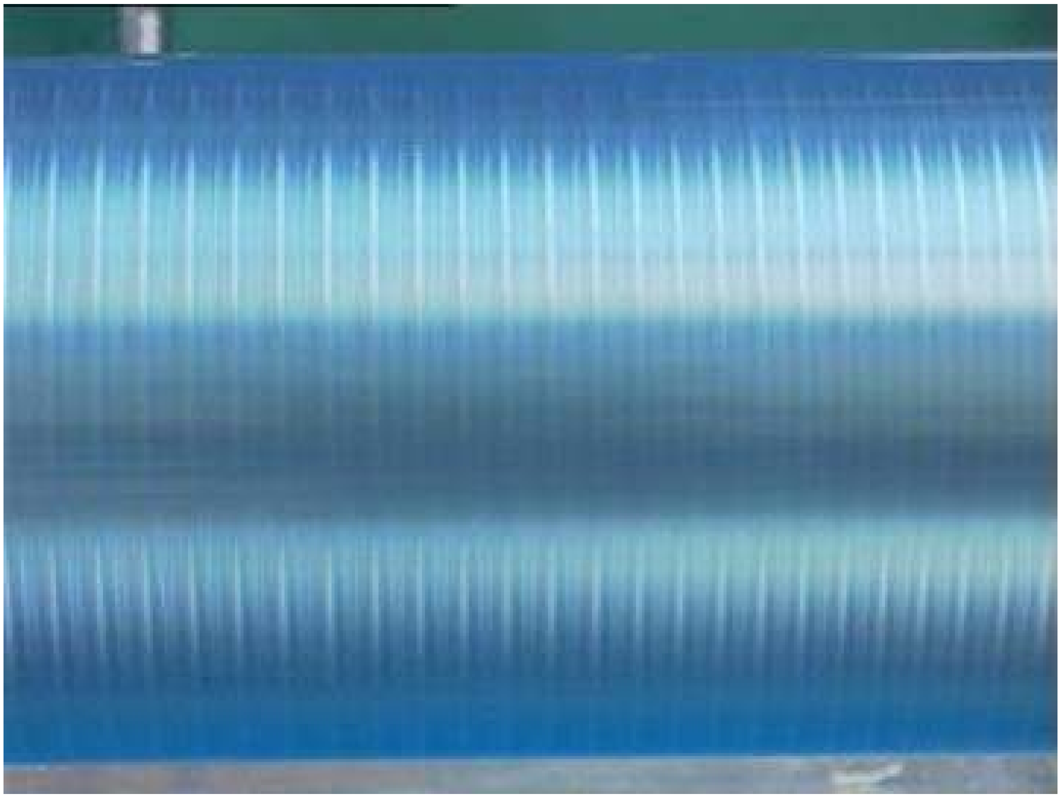

Figure 6.13: Photograph of two-fluid Taylor-Couette flow. The fluids are equal volumes of 60 wt% glycerine in water - 60 wt% Drakeol-35 in kerosene.

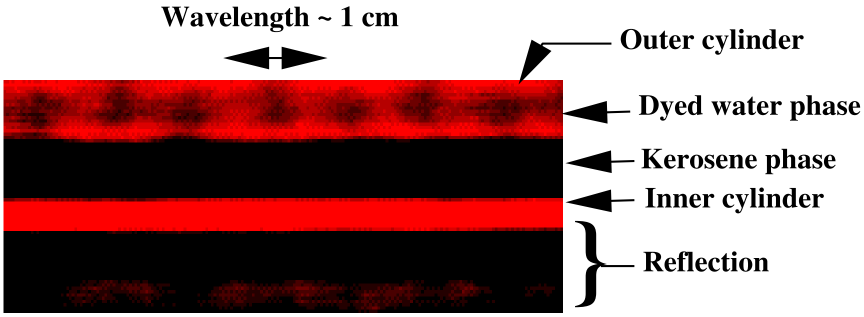

Figure 6.14: The Laser Induced Fluorescence view of two-fluid Taylor-Couette flow just above the onset where the interface is flat. The red region is the dyed aqueous phase and the black region is the undyed organic phase. The fluids are equal volumes of 60 wt% glycerine in water - 60 wt% Drakeol-35 in kerosene.

theoretical values predicted by both the inviscid and viscid analyses are compared in Figures 6.16 and 6.17. Figure 6.17 also includes the experimentally observed onset for the time dependent vortices. Countercurrent axial flow was not included in these experiments, and therefore the aluminum inner cylinder with the double-holed double spacers was used. The onset of Taylor vortices was determined visually by laser highlighted flow visualization of particles swept into vortex at the critical point. As expected from the inviscid and viscous theories, Taylor vortices first appear in the less viscous phase and the interface remains flat. Furthermore, the viscous theory and the experimental results agree very well quantitatively. Only at low rotation rates is there a slight discrepancy. This is an indication that gravity is still important at the lower outer cylinder rotation rates. Since the experimental results also agree well with the inviscid theory, the simple Rayleigh criterion may be used in preliminary calculations for even these relatively viscous fluids.

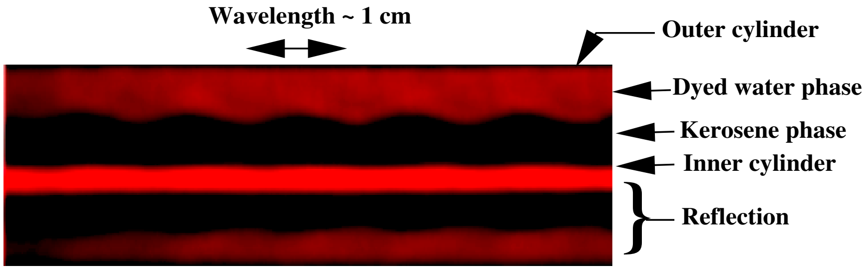

Figure 6.15: LIF view of two-fluid Taylor-Couette flow with a wavy interface. The fluids are equal volumes of 60 wt% glycerine in water - 60 wt% Drakeol-35 in kerosene.

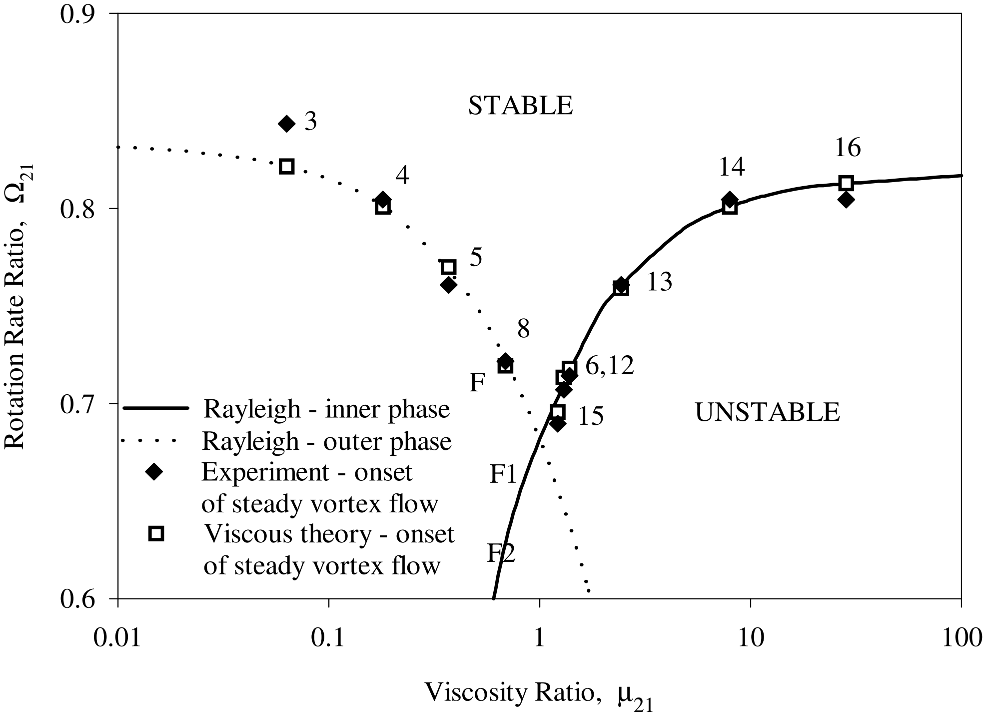

Figure 6.16: A comparison of the experimental results and invisid and viscid theoretical predictions for the onset of two-fluid Taylor-Couette flow with various viscosity ratios and equal fluid depths. The fluid pairs are identified by number corresponding to the entries in Table 6.1. $\Omega_2 = 7$ rev/s. Point F correponds to the FLUENT run (Fig.4.4), $\Omega_2 = 6.0$ rev/s. Point F1 corresponds to the FIDAP run for counterrotating vortices (Fig. 4.5), $\Omega_2 = 8.2$ rev/s; point F2 corresponds to the FIDAP run for corotating vortices (Fig. 4.6), $\Omega_2 = 7.7$ rev/s.

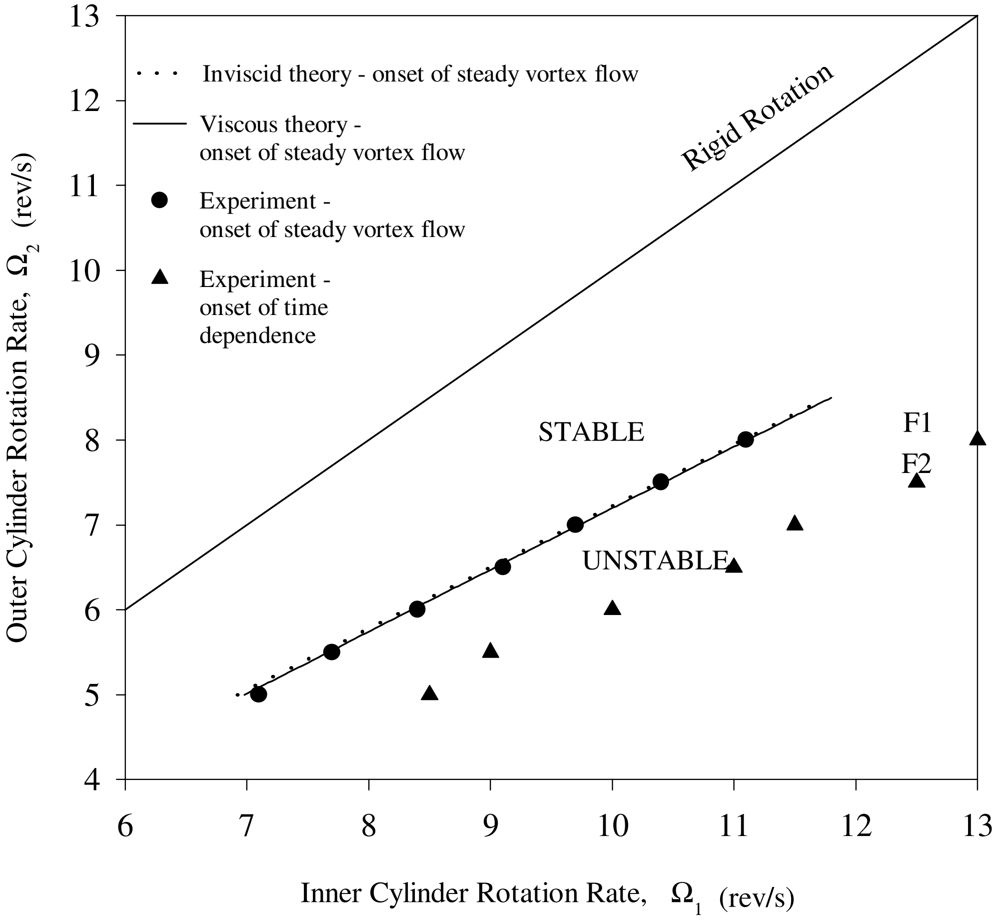

Figure 6.17: A comparison of the experimental results and invisid and viscid theoretical predictions for the onset of two-fluid Taylor-Couette flow in a typical fluid pair. The experimentally observed onset of time dependence is also recorded. The fluids are equal volumes of 60 wt% glycerine in water - 60 wt% Drakeol-35 in kerosene ($\mu_{21} = 0.69$). The point marked F1 corresponds to the FIDAP calculation for counterrotating vortices (Figure 4.5); the point marked F2 corresponds to the FIDAP calculation for corotating vortices (Figure 4.6).

6.3.2 Axial Dispersion

The effects of Taylor number and axial flow are expected to be similar in one and two-fluid Taylor-Couette flow. However, in the two-fluid case, axial dispersion must be considered for both phases. When only one phase is Rayleigh unstable, the boundary conditions require weaker vortices in the other phase and, as a result, the axial dispersion in both phases is expected to decrease.

With the addition of countercurrent axial flow, however, the effects on axial dispersion is less predictable. Before the onset of vortices, the countercurrent axial velocity profiles may be easily determined by the equations of motion and continuity (section 3.1.2). For cases when the fluid viscosities, axial flowrates, and the fluid depths of the two phases are not matched, backflow can occur in one of the phases and as a result increase axial dispersion in that phase. Figure 3.1 illustrates a velocity profile for countercurrent axial flow and the resulting backflow. However, this backflow effect may be mitigated by the presence of Taylor vortices in that phase to reduce axial dispersion. For the countercurrent flow rates accessible in the experiments, the effect of Taylor vortices seems to dominate the effect of backflow and axial dispersion is minimized near the onset of the vortex flow.

Figures 6.18 and 6.19 summarize the effect of Taylor vortices on dispersion for the case of nearly matched viscosities. The minimum axial dispersion occurs in both phases very near the onset of instability. Further increases in the relative rotation rate result in stronger vortices and higher dispersion. This is consistent with similar experiments in the one fluid case (section 2.3).

The dispersion characteristics of two-fluid Taylor-Couette flow when the phase viscosities are not matched are included in Figure 6.21. In this case, the heavy phase is less viscous and therefore, it becomes Rayleigh unstable first. Axial dispersion in the heavy fluid is at a minimum slightly after the heavy fluid critical point. In contrast, the axial dispersion in the light phase reaches a minimum slightly *before* the light fluid critical point (as predicted by the Rayleigh criterion). This occurs because the Rayleigh unstable heavy phase drives a weaker vortex motion in the light phase. Figure 6.20 illustrates the opposite case where the heavy phase is more viscous; similar behavior is observed.

The minimum in axial dispersion is consistently observed near the onset of the vortex flow in the corresponding phase. However, the actual quantification of the dispersion is less repeatable. Since dispersion is determined by the shape of the outlet curve, it can be sensitive to small irregularities in the flow pattern and operation. The quantification of axial dispersion in one fluid Taylor-Couette flow also varies widely, although the trends are clear (section 2.3).

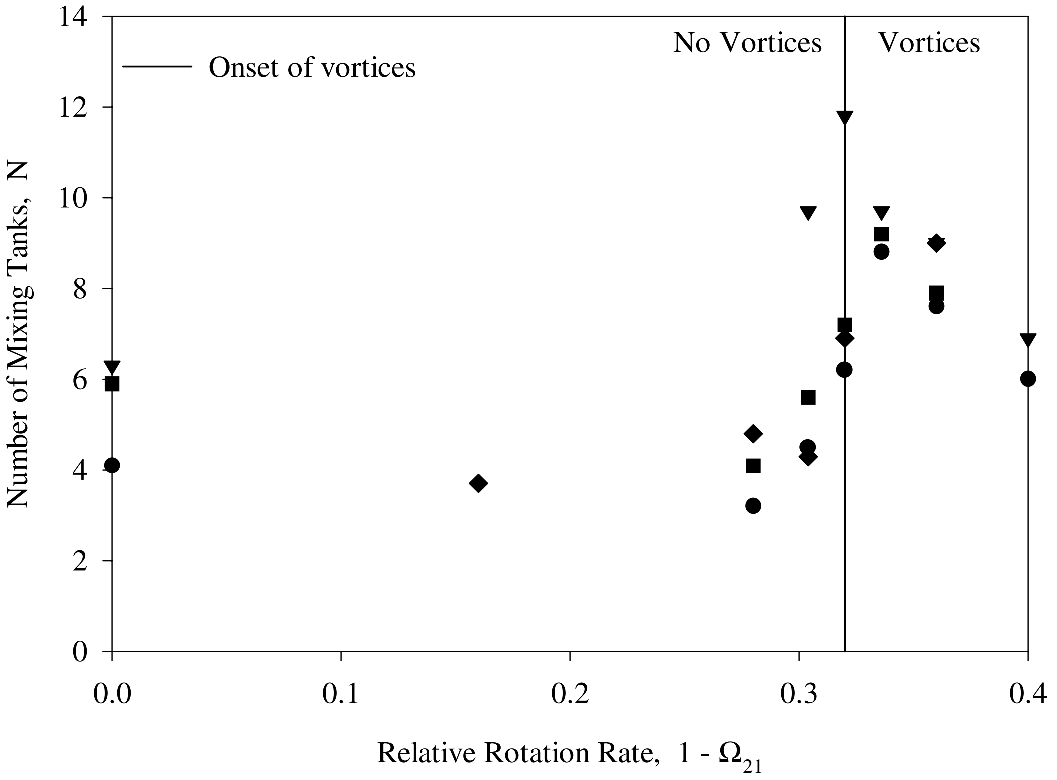

Figure 6.18: Axial dispersion in the heavy phase with matched viscosity fluids. The vertical line represents the onset of two-fluid Taylor-Couette flow. The fluids are equal volumes of 60 wt.% glycerine in water and 50 wt.% Drakeol-35 in IsoPar-L ($\mu_{21} = 0.96$). The different symbols identify the individual experiment series.

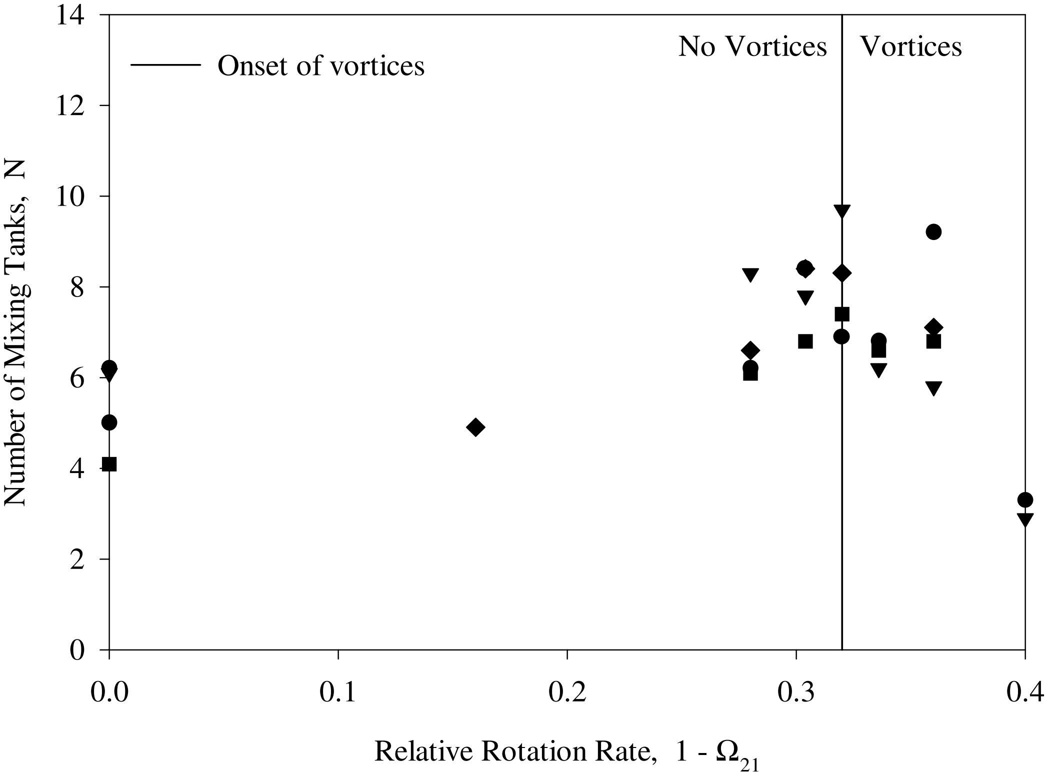

Figure 6.19: Axial dispersion in the light phase with matched viscosity fluids ($\mu_{21} = 0.96$). The vertical line represents the onset of two-fluid Taylor-Couette flow. The fluids are equal volumes of 60 wt.% glycerine in water and 50 wt.% Drakeol-35 in IsoPar-L ($\mu_{21} = 0.96$). The different symbols identify the individual experiment series.

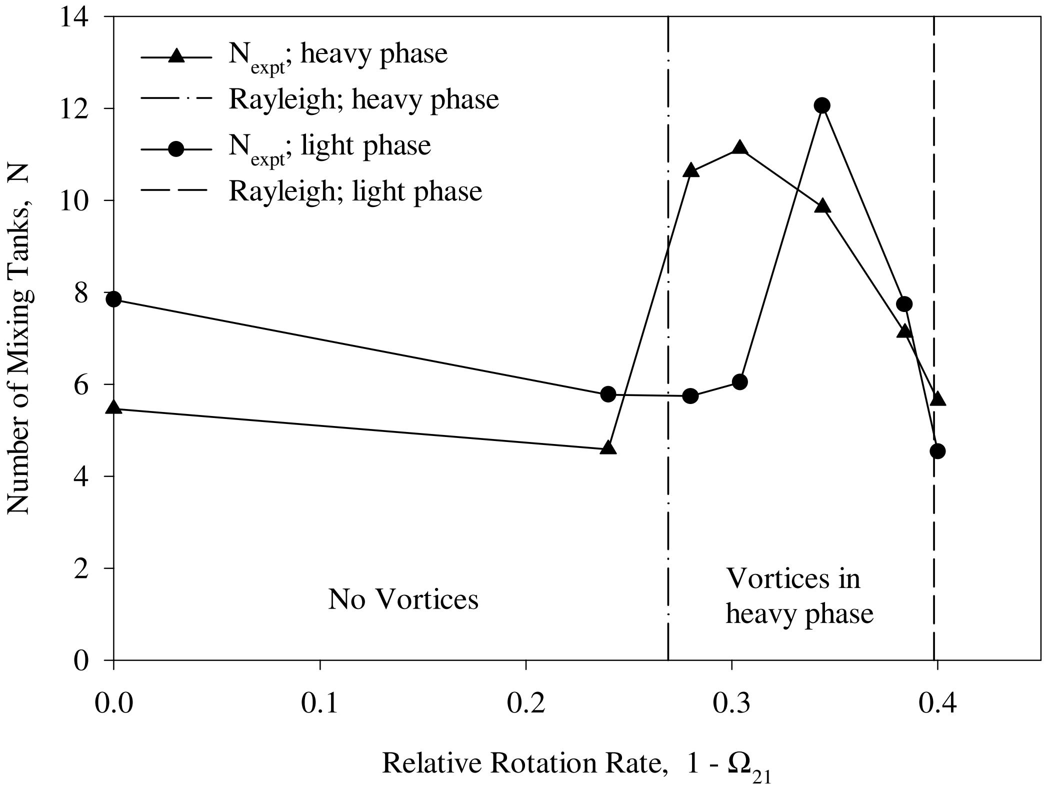

Figure 6.20: Axial dispersion in both phases with a more viscous inner phase ($\mu_{21} = 0.63$). The vertical lines represent the onset of two-fluid Taylor-Couette flow. The fluids are equal volumes of 60 wt.% glycerine in water and 60 wt.% Drakeol-35 in IsoPar-L ($\mu_{21} = 0.63$).

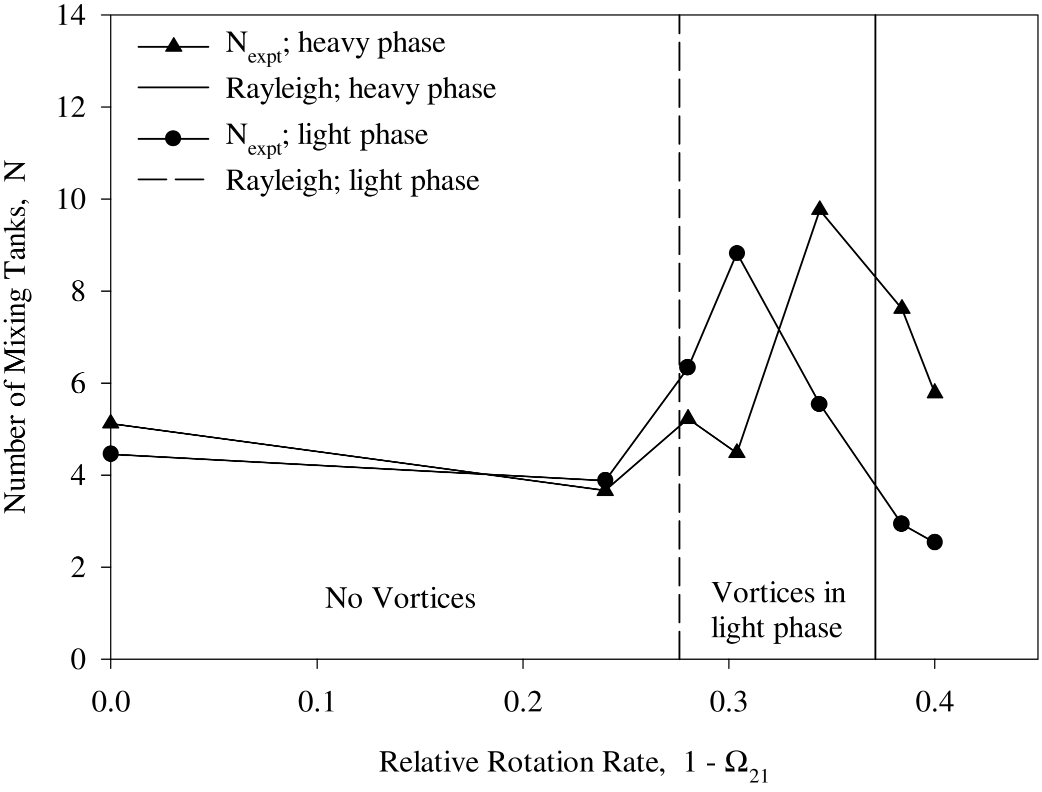

Figure 6.21: Axial dispersion in both phases with a less viscous inner phase. The vertical lines represent the onset of two-fluid Taylor-Couette flow. The fluids are equal volumes of 60 wt.% glycerine in water and 40 wt.% Drakeol-35 in IsoPar-L ($\mu_{21} = 1.46$).

6.3.3 Liquid Extraction

The liquid extraction results are based on experiments with the several different tracers and viscosity ratios. The tracers each have a different partition coefficient, m, as identified in Table 6.2. A comparison of the results for the different tracers reveals which phase tends to be more "mass transfer limiting" for the extraction conditions. The experiments with the different viscosity ratios reveal the effect of vortex strength on extraction performance. Several viscosity ratios were chosen:

1. the nearly matched viscosity case ($\mu_{21} = 0.96$), with both phases Rayleigh unstable and vortices in both phases;
2. the unmatched viscosity case, with only the less viscous phase Rayleigh unstable. Vortices in that phase drive weaker secondary vortices in the more viscous phase. Since the onset of the vortex flow occurs at nearly the same rotation rate ratio for the experiments with $\mu_{21} = 0.63$ and for the experiments with $\mu_{21} = 1.46$, the vortex velocities in both of these experiments should also be approximately equal. The only difference between these two experiments is then which phase contains the vortices;
3. the unmatched viscosity case, with more extreme viscosity ratios: $\mu_{21} = 0.23$ and $\mu_{21} = 4.91$. Again, the vortices in both experiments should have nearly equal veloctities.

The results of these extraction experiments are illustrated in Figures 6.22, 6.23, and 6.24 and provide the basis for calculating mass transfer coefficients and number of theoretical stages. The fraction of tracer extracted significantly increases once Taylor vortices appear in one of the phases. In Figure 6.22, only a maximum of 12% of the injection of acetophenone was extracted. This could appear to be disappointing, but is actually quite good. Since the partition coefficient is $m = 0.125$, the absolute maximum extraction possible is 12.5% with infinite stages. For partition coefficients greater than unity, 100% of the tracer may be extracted with infinite stages.

The experimental values for the overall mass transfer coefficients, K_1, were calculated by equation 6.2; the effects of axial velocity and dispersion are included in the definition of the mass transfer coefficient. The theoretical predictions for the overall mass transfer coefficient (neglecting dispersion) were calculated using penetration theory and either (1) the countercurrent axial velocity profile when vortices were not present or (2) Computational Fluid Dynamics (CFD) of two-fluid Taylor-Couette flow with countercurrent axial flow when vortices were present. The onset of the vortex pattern was determined by the viscous linear stability analysis of section 3.2.2. CFD and boundary layer theory are discussed in sections 4.2 and 5.2, respectively. Boundary layer theory predicts the individual mass transfer coefficients, k_1 and k_2, and the only difference between two is the diffusivity in that phase. The diffusivity in the heavy phase

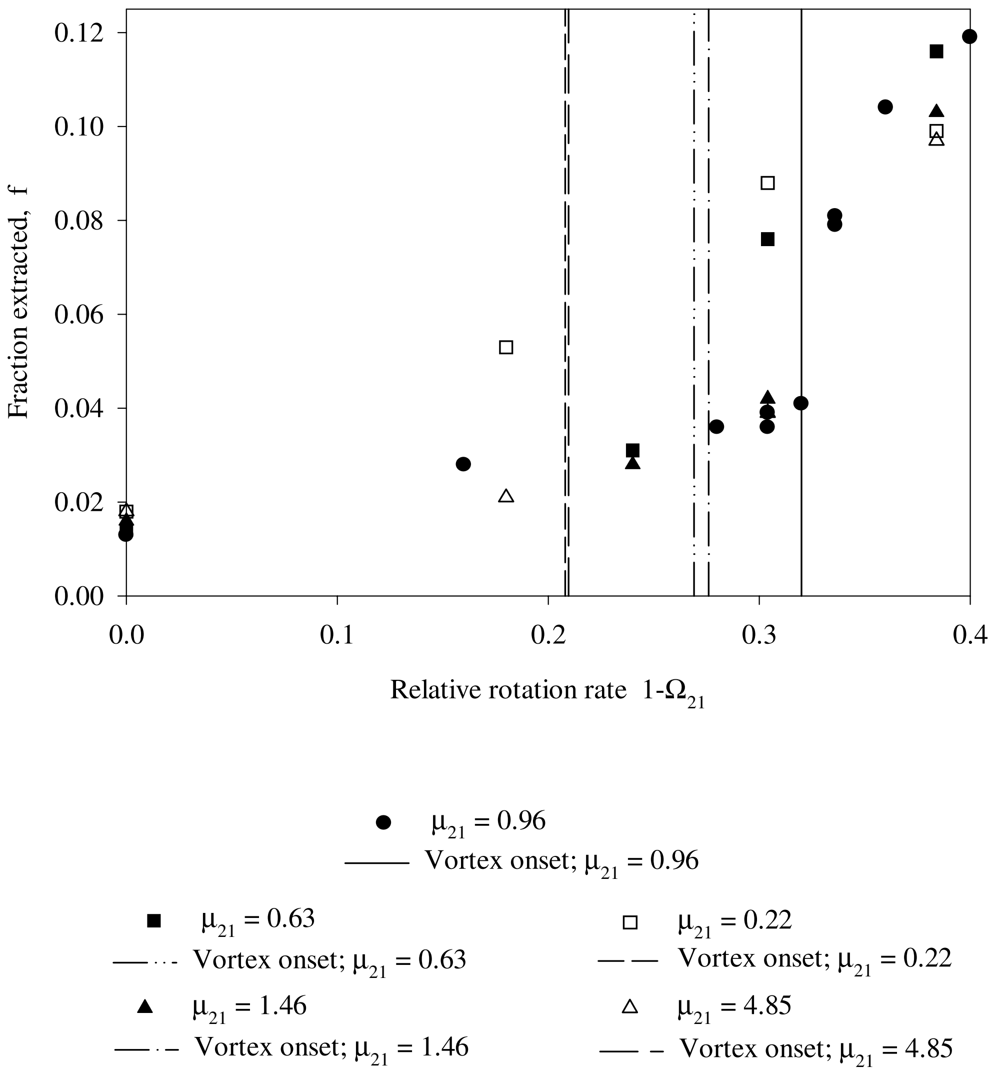

Figure 6.22: Fraction of acetophenone extracted from the light phase versus the relative rotation rate of the cylinders. The vertical lines represent the onset of two-fluid Taylor-Couette flow for various fluid pairs. ($m = 0.125$)

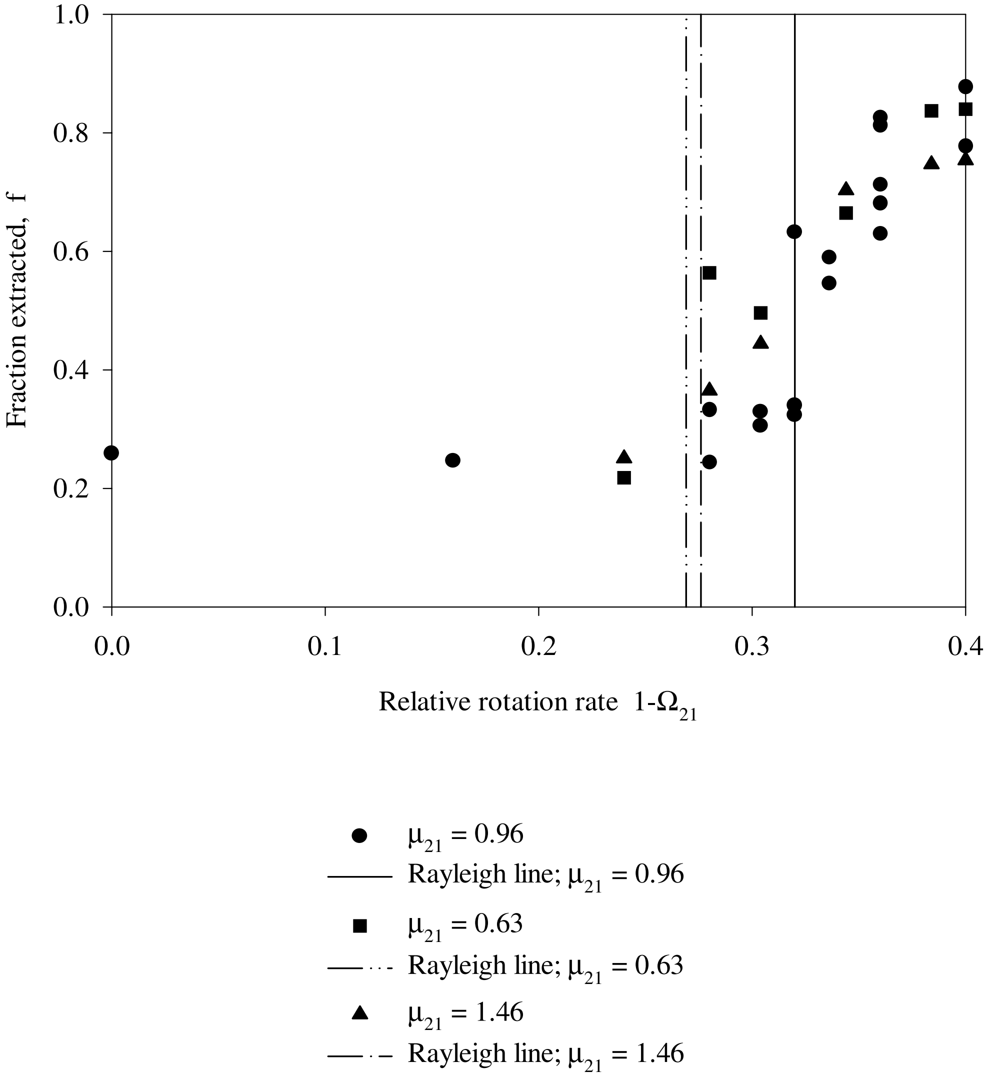

Figure 6.23: Fraction of sec-phenethyl alcohol extracted from the light phase versus the relative rotation rate of the cylinders. The vertical lines represent the onset of two-fluid Taylor-Couette flow for various fluid pairs. ($m = 2.7$)

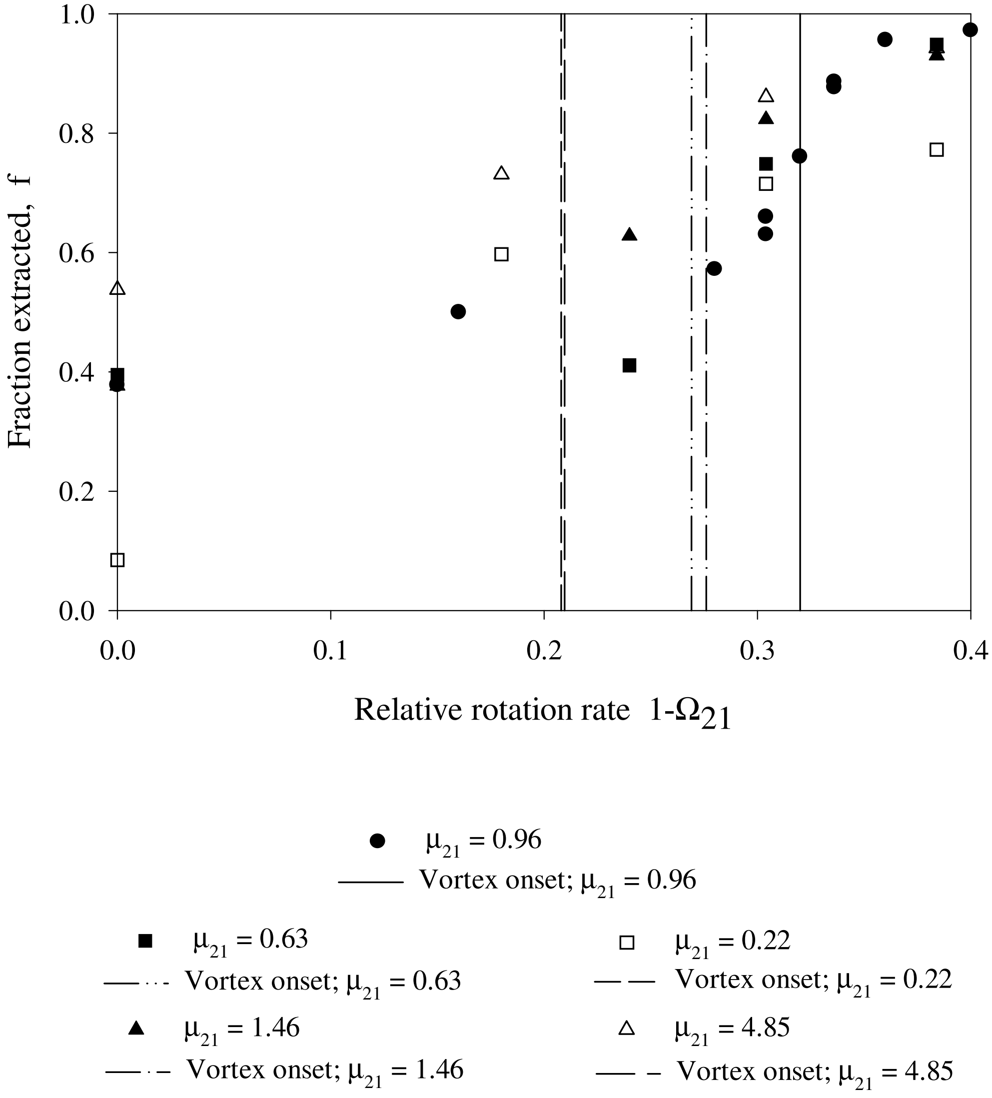

Figure 6.24: Fraction of benzyl alcohol extracted from the light phase versus the relative rotation rate of the cylinders. The vertical lines represent the onset of two-fluid Taylor-Couette flow for various fluid pairs. ($m = 14.0$)

was estimated by the Wilke-Chang equation to be $D_2 = 10^{-6}$ cm^2/s and the diffusivity in the light phase $D_1 = \mu_{12} D_2$ [19].

The experimental and theoretical results for acetophenone ($m = 0.125$) are plotted in Figures 6.25 (the matched viscosity case), 6.26 and 6.27 (the unmatched viscosity cases). Similarly, the results for sec-phenethyl alcohol ($m = 2.7$) are plotted in Figures 6.28, and 6.29; the results for benzyl alcohol ($m = 14.0$) in Figures 6.30, 6.31 and 6.32. The onset of Taylor vortices in the less viscous phase (as predicted by the inviscid and viscous analyses) is indicated by the vertical lines.

There are several important features of these graphs:

- For all cases, the overall mass transfer coefficient, $Nu = \frac{K_1 d}{D_2}$, is small and nearly constant until vortices appear and then increases dramatically with increasing strength of the Taylor vortices. The mass transfer coefficient is approximately linearly proportional to the relative rotation rate as expected by penetration theory and a weakly non-linear analysis for the vortex velocity strength.

- The calculated mass transfer performance further increases once the vortices in the more stable phase are sufficiently strong; the slope of the curve (Nu vs. $1 - \Omega_{21}$) increases. This is the point where corotating vortices first appear when countercurrent axial flow is not present. This increase is most visible in Figures 6.27 and 6.31, but is also apparent in Figures 6.26, 6.29, and 6.32.

- The repeatability of the experiments is good.
- The theoretical predictions and the experimental observations agree within a factor of three with the experimental results higher than the predictions. End effects and axial dispersion were not included in the theoretical analysis.
- The increase in axial dispersion at the higher rotation rates does not seem to degrade the mass transfer performance. This is not surprising, since the majority of the mass transfer occurs quickly and primarily at the injection end, before dispersion effects develop significantly.
- The maximum Nusselt numbers compare well with liquid-liquid extraction in packed columns where correlation for individual mass transfer coefficients is

  $$Nu_{ind.} = 0.0051 Re^{2/3} Sc^{1/2} (ad)^{0.4} (d(g/\nu^2)^{1/3}).$$

  Here d is the nominal packing size, g gravity, and the Reynolds number is based on the superficial fluid velocity and the packing area per bed volume [19]. For $Re = 50$, $Sc = 1000$, $m = 2.7$, and 1 inch Raschig rings, the overall Nusselt number is approximately $Nu = 2000$.

- When the tracer prefers the raffinate (light) phase ($m \ll 1$), the extract (heavy) phase is "mass transfer limiting". Therefore, Taylor vortices with their higher surface renewal would be expected to be more beneficial in the heavy phase. This occurs when the heavy fluid is less viscous than the light fluid ($\mu_{21} < 1$). As observed in Figures 6.26 and 6.27, the mass transfer coefficient is always higher when Taylor vortices are in the heavy phase. The opposite effect is observed when the tracer prefers the extract (heavy) phase as seen in Figures 6.31 and 6.32. This suggests the following operating guidelines: when $m \gg 1$, better performance is expected when $\mu_{21} > 1$ and vice versa.

- When the Schmidt numbers for the two phases are approximately equal (as in the matched viscosity case), penetration theory predicts that the individual mass transfer coefficients for the two phases are approximately equal. In this case, the overall mass transfer coefficient is approximately

  $$K_1 = \frac{mk_1}{m+1}. \tag{6.4}$$

  Table 6.4 shows that the normalized overall mass transfer coefficients based on equation 6.4 agree well with the experimental values for this matched viscosity case. The theoretical and experimental values where separately normalized by $K_1/K_{1,\text{acetophenone}}$.

- Without countercurrent axial flow, FIDAP predicts corotating vortices and a corresponding decrease in mass transfer performance. Since the experiments do not show a similar decrease, it suggests that corotating vortices have not appeared. Both FIDAP and the linear stability analysis predict that corotating vortices disappear with countercurrent flow [8].

Only a few experiments were completed at higher countercurrent axial flow rates due to the primitive weir system. As seen in figure 6.33, increasing the axial flowrate decreases the mass transfer performance. This would be expected since in the both the one and two fluid cases, higher flowrates have been shown to (1) stabilize the Taylor vortices so the vortex strength is decreased [14], (2) create streamlines that bypass the vortices [48], (3) increase axial dispersion [32, 83], and (4) decrease the residence time in the extractor. The adverse effects of increased flowrate may be counteracted by increasing the relative rotation rate of the cylinders.

The number of theoretical stages may be calculated from equation 6.3. The results again are nearly independent of rotation rate below the critical Taylor number and then increases above the critical Taylor number. A maximum of 1.5 theoretical stages are observed in the experiments. This compares favorably with commercial extractors considering the two-fluid Taylor-Couette extractor has not been optimized (see Table 2.8). Furthermore, the performance for the commercial equipment reported in the literature is for fluid pairs with diffusion coefficients an order of magnitude higher than the estimated diffusion coefficients in these experiments. When our results are adjusted using the pentration theory relation for the diffusion coefficient, $n \propto \sqrt{D^*} \approx \sqrt{10}$, this two-fluid Taylor-Couette extractor prototype has approximately 4.5 theoretical stages which is very competitive with the commercial equipment.

Tracer	Partition Coefficient, m	$K_{1,norm}$ Theory	$K_{1,norm}$ Experiment
Acetophenone	0.125	1	1
sec-Phenethyl Alcohol	2.7	6.6	6.3
Benzyl Alcohol	14.0	8.9	9.0

Table 6.4: Comparison of normalized overall mass transfer coefficients as theoretically predicted and experimentally observed. 60 wt.% glycerine-water / 50 wt.% Drakeol-35 in IsoPar-L ($\mu_{21} = 0.96$).

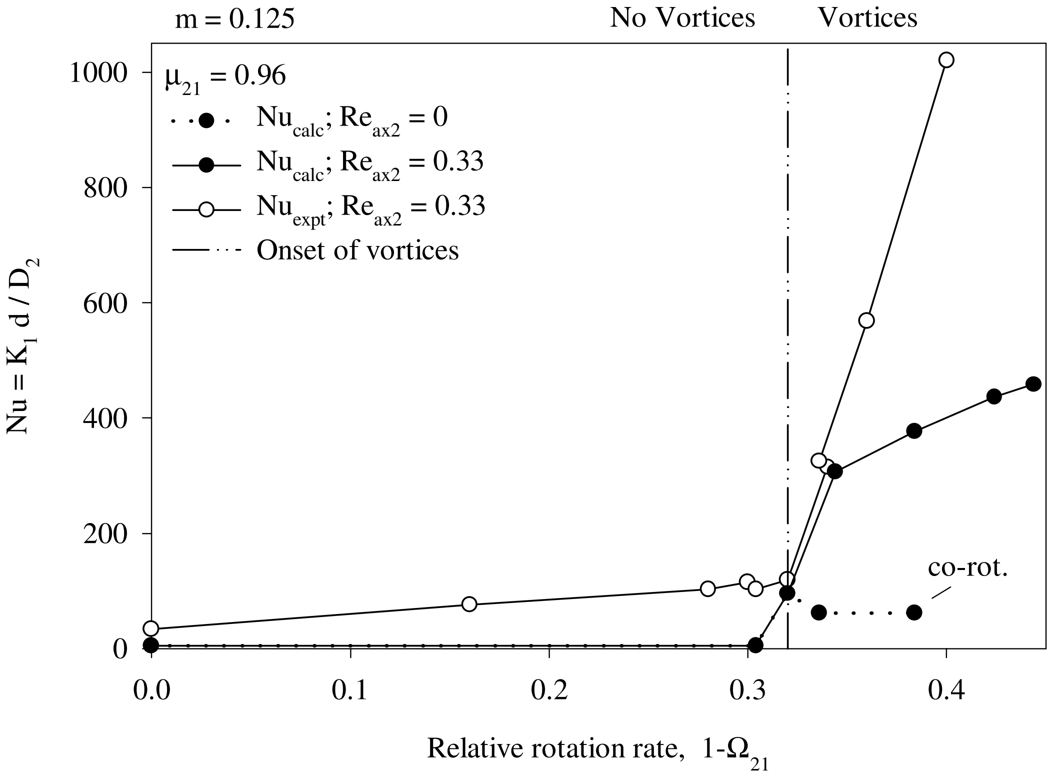

Figure 6.25: Mass transfer coefficients for the extraction of acetophenone ($m = 0.125$) from the light phase as a function of relative rotation rate - the matched viscosity case. The fluids are equal volumes of 60 wt.% glycerine in water and 50 wt.% Drakeol-35 in IsoPar-L ($\mu_{21} = 0.96$).

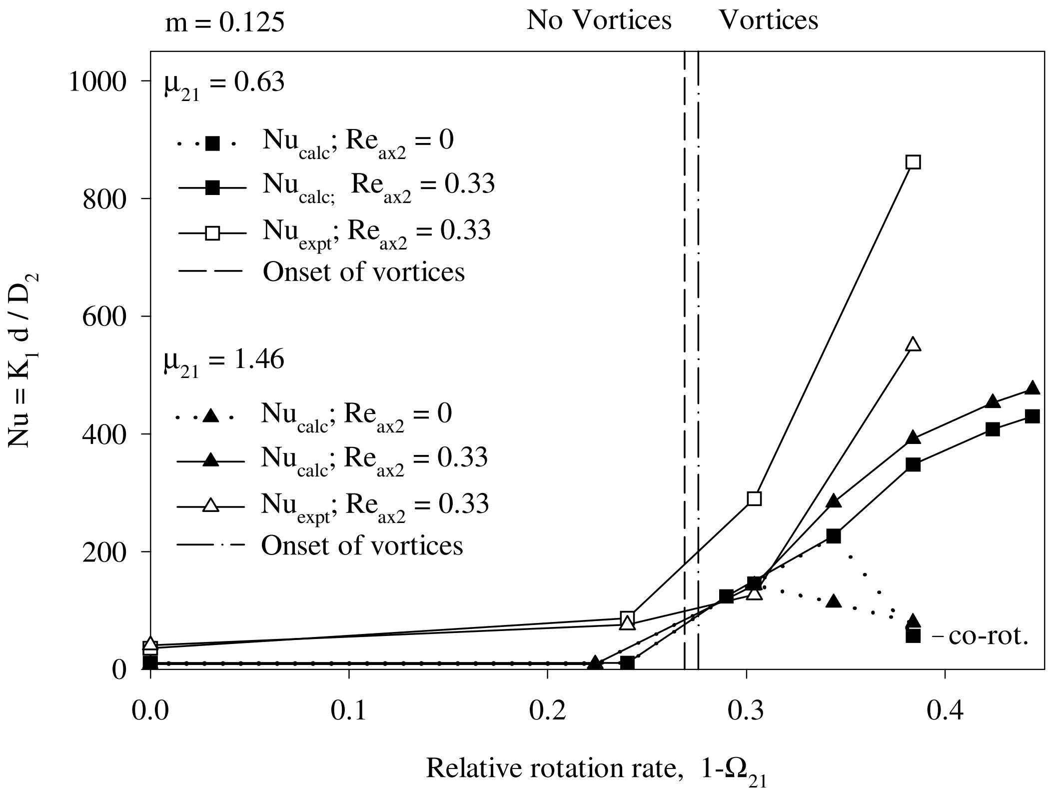

Figure 6.26: Mass transfer coefficients for the extraction of acetophenone ($m = 0.125$) from the light phase as a function of relative rotation rate - the unmatched viscosity case. The fluid pairs are equal volumes of 60 wt.% glycerine in water with 60 wt.% Drakeol-35 in IsoPar-L ($\mu_{21} = 0.63$) and 60 wt.% glycerine in water with 40 wt.% Drakeol-35 in IsoPar-L ($\mu_{21} = 1.46$).

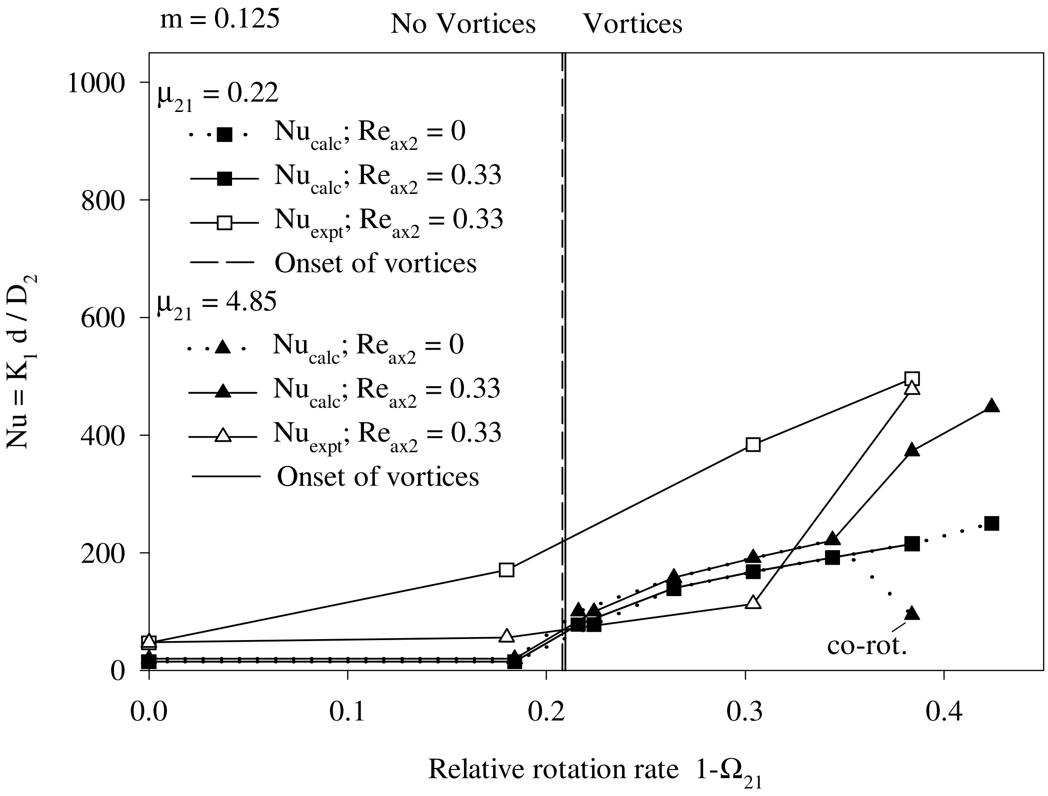

Figure 6.27: Mass transfer coefficients for the extraction of acetophenone ($m = 0.125$) from the light phase as a function of relative rotation rate - the unmatched viscosity case. The fluid pairs are equal volumes of 60 wt.% glycerine in water with 80 wt.% Drakeol-35 in IsoPar-L ($\mu_{21} = 0.23$) and 60 wt.% glycerine in water with 0 wt.% Drakeol-35 in IsoPar-L ($\mu_{21} = 4.91$).

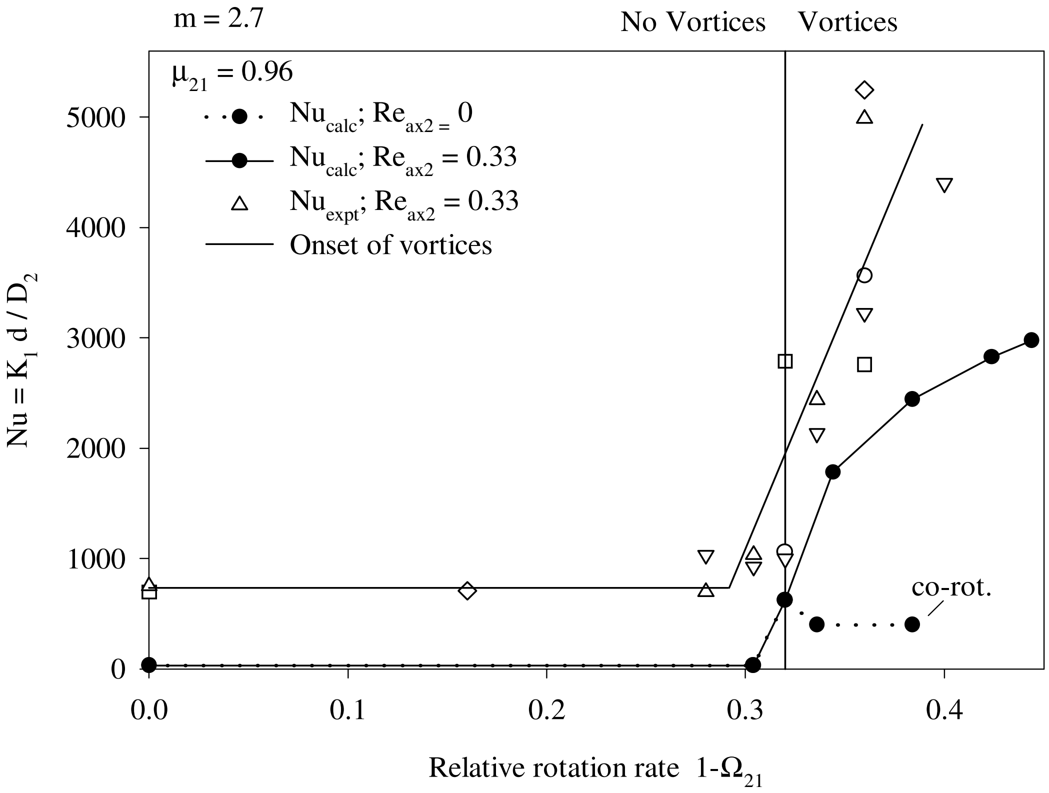

Figure 6.28: Mass transfer coefficients for the extraction of sec-phenthyl alcohol ($m = 2.7$) from the light phase as a function of relative rotation rate - the matched viscosity case. The fluids are equal volumes of 60 wt.% glycerine in water and 50 wt.% Drakeol-35 in IsoPar-L ($\mu_{21} = 0.96$).

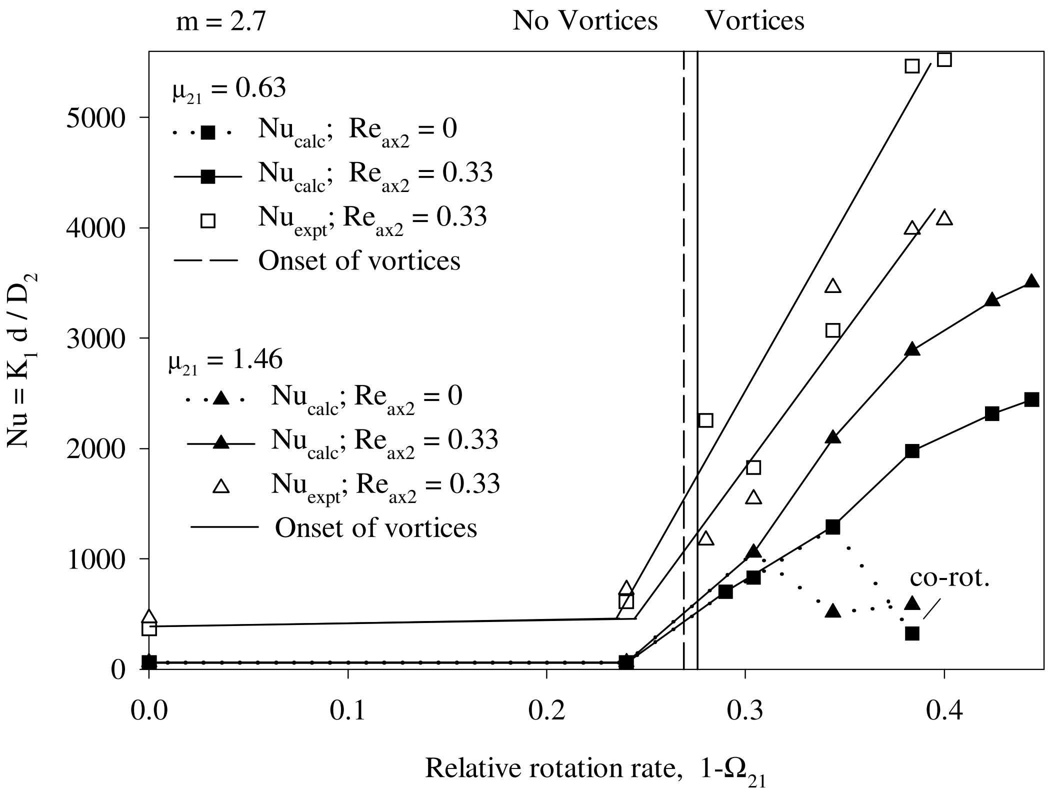

Figure 6.29: Mass transfer coefficients for the extraction of sec-phenthyl alcohol ($m = 2.7$) from the light phase as a function of relative rotation rate - the unmatched viscosity case. The fluid pairs are equal volumes of 60 wt.% glycerine in water with 60 wt.% Drakeol-35 in IsoPar-L ($\mu_{21} = 0.63$) and 60 wt.% glycerine in water with 40 wt.% Drakeol-35 in IsoPar-L ($\mu_{21} = 1.46$).

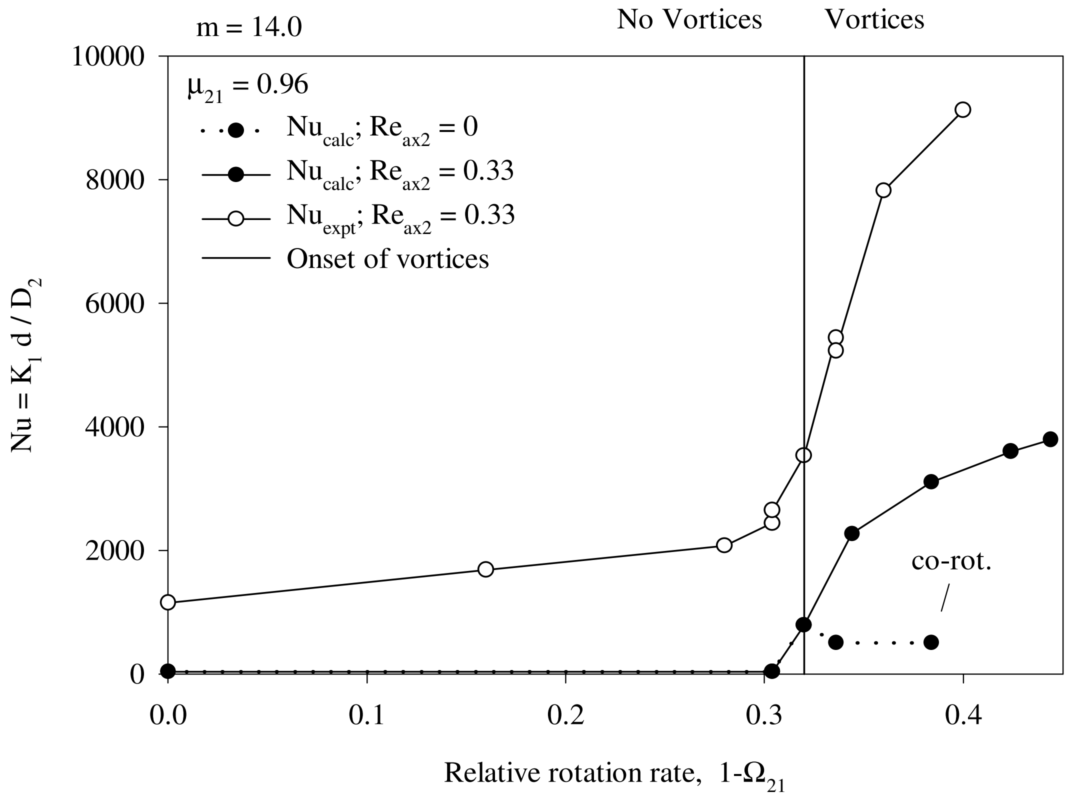

Figure 6.30: Mass transfer coefficients for the extraction of benzyl alcohol ($m = 14.0$) from the light phase as a function of relative rotation rate - the matched viscosity case. The fluids are equal volumes of 60 wt.% glycerine in water and 50 wt.% Drakeol-35 in IsoPar-L ($\mu_{21} = 0.96$).

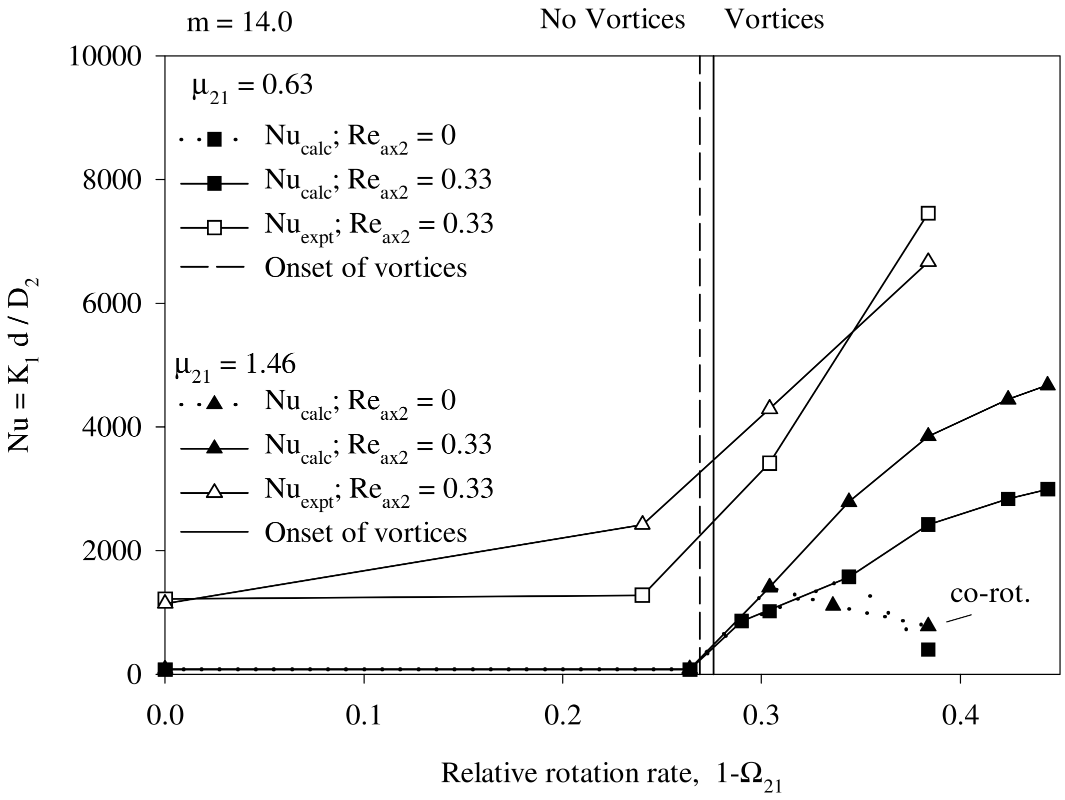

Figure 6.31: Mass transfer coefficients for the extraction of benzyl alcohol ($m =$ 14.0) from the light phase as a function of relative rotation rate - the unmatched viscosity case. The fluid pairs are equal volumes of 60 wt.% glycerine in water with 60 wt.% Drakeol-35 in IsoPar-L (μ_{21} = 0.63) and 60 wt.% glycerine in water with 40 wt.% Drakeol-35 in IsoPar-L ($\mu_{21} = 1.46$).

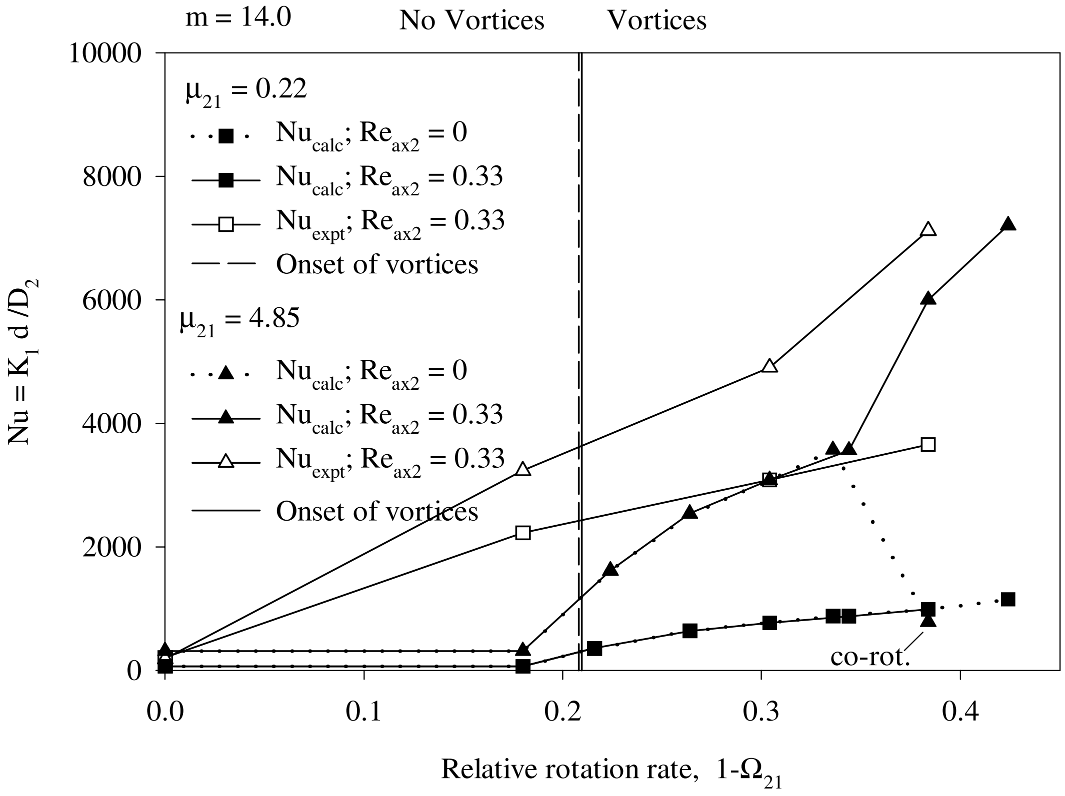

Figure 6.32: Mass transfer coefficients for the extraction of benzyl alcohol ($m = 14.0$) from the light phase as a function of relative rotation rate - the unmatched viscosity case. The fluid pairs are equal volumes of 60 wt.% glycerine in water with 80 wt.% Drakeol-35 in IsoPar-L ($\mu_{21} = 0.23$) and 60 wt.% glycerine in water with 0 wt.% Drakeol-35 in IsoPar-L ($\mu_{21} = 4.91$).

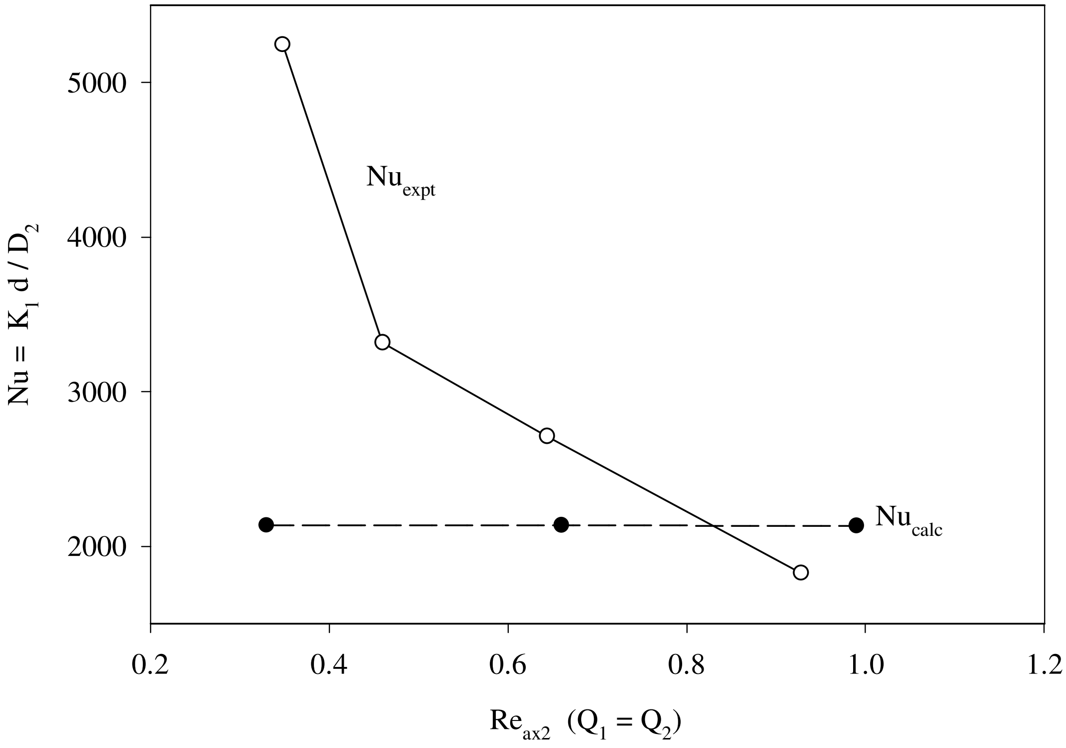

Figure 6.33: The effect of axial flowrate on the experimentally determined mass transfer coefficient for the extraction of sec-phenethyl alcohol extraction from the light phase in the matched viscosity case. The fluid pairs are equal volumes of 60 wt.% glycerine in water and 50 wt.% Drakeol-35 in IsoPar-L ($\mu_{21} = 0.96$). $\Omega_{21} = 0.64$, $\Omega_{21,c} = 0.687$.

Chapter 7

Summary

The fluid mechanics and the mass transfer characteristics of radially stratified two-fluid Taylor-Couette flow have been investigated in an effort to develop a new device for liquid-liquid extraction. In a two-fluid Taylor-Couette extractor, the two phases retain their individual integrity and contact each other only at a single well-defined interface. Although the interfacial area is small, the vortex motion provides an active surface for mass transfer. This differs from standard liquid-liquid extraction processes, which maximize a relatively inactive surface area by dispersing one phase as small droplets in the other phase. Such dispersion based systems are often inadequate for liquid pairs that are easily emulsifiable, such as in bioseparations that use aqueous two phase or reverse micelle systems. Figure 1.1 is a schematic of a two-fluid Taylor-Couette liquid extractor.

The present study has demonstrated that two-fluid Taylor-Couette flow with countercurrent axial flow is achievable in practice. When the vortices first appear, axial dispersion is minimized and the interphase mass transfer starts to increase. In supercritical two-fluid Taylor-Couette flow, the extraction performance continues to improve with the mass transfer coefficient proportional to strength of Taylor vortices. A maximum of 4.5 theoretical stages is observed for the conditions investigated. This is quite promising considering the prototype design is far from optimized. Just halving the gap width alone would give twice as many vortices and therefore better mass transfer coefficients. In addition, modifying the end effects that result from the primitive weir system could also significantly improve the extraction performance and permit operation at larger rotation rate differences for even higher efficiencies.

These simple modifications would bring the Taylor-Couette extractor above the level of available centrifugal extractors, which have benefited from a long optimization process. The Taylor-Couette extractor would also then be competitive with packed columns for separation efficiency, and with potentially better flow control and decreased product residence times than in packed columns. This suggests that further optimization studies and design improvements could produce a highly competitive extractor for the relatively small production levels typical of the biotechnology industry. The Taylor-Couette extractor would have not only the separation efficiency of current commercially available equipment, but also the desirable and uniquely inherent features of simple fluid mechanics and prevention of emulsion formation.

The theoretical analyses for both the fluid mechanics and the mass transfer agree quite well with experimental results and provide a good basis for the commercial design and development of a two-fluid Taylor-Couette extractor. The linear stability analysis predicts the onset of the two-fluid Taylor-Couette instability and the combination of boundary layer theory and computational fluid dynamics predicts the interphase mass transfer without empiricism.

Although this study was primarily interested in two-fluid Taylor-Couette flow, other instabilities can also occur. With low viscosity fluids at low rotation rates, two-fluid Taylor-Couette flow is not observed experimentally, but rather the barber pole pattern, which is believed to be a lingering gravitational effect. At high countercurrent axial flowrates, the linear stability analysis predicts a Kelvin-Helmholtz instability related to the countercurrent flow profile. If axial flow is not present, the two computational fluid dynamics packages (FLUENT and FIDAP) calculate that at sufficiently high relative rotation rates, vortices paired across the interface corotate, instead of counterrotate, with each other. Although these effects are all very interesting from a fluid mechanics point of view, they would seriously degrade the extraction efficiency and must be understood in order to be avoided in the design and operation of an extractor.

Chapter 8

Future Designs and Development

8.1 Further Studies

To design and optimize a Taylor vortex extraction system, better understanding is needed of the supercritical behavior of two-fluid Taylor-Couette flow especially when countercurrent flow is present. For this computational fluid dynamics would continue to be helpful. The important items to include in future studies are:

- Enhanced vortices. What is the effectiveness of adding features to the cylinders to enhance the vortex motion? How is the countercurrent axial flow behavior affected?
- Corotating vortices. Under what conditions do corotating vortices appear?
- Interface deformation. How does the radius ratio, fluid depth, fluid properties, and outer cylinder rotation rate affect the interface deformation and is this important?

- Other instabilities. Is the barber pole pattern a lingering gravitational effect? Is the Kelvin-Helmholtz instability a concern in practice? When does the azimuthal viscous shear instability appear?

- Axial dispersion. A predictive model for axial dispersion must be developed and incorporated into the mass transfer model. Why does the minimum in axial dispersion occur near the onset of the vortex flow? Can this minimum be shifted, broadened, or removed?

In addition, further experiments are required to demonstrate that two-fluid Taylor-Couette is a commercially viable process, especially for bioseparations. Preliminary experiments suggest that two-fluid Taylor-Couette flow with countercurrent axial flow in aqueous-aqueous systems is achievable. However, a more sophisticated equipment design is necessary to provide an adequate environment for bioproducts. Since these low density difference systems are more prone to emulsion formation and carry-over at the ends, a very careful weir design is required. Some considerations for future equipment designs and experiments include:

- Does the mass transfer performance continue to improve with more extreme rotation rate differences? What is the limiting factor - emulsion formation, denaturation, appearance of corotating vortices, dispersion?

- Are corotating vortices observed in practice?

- How can the performance be improved by adding features to the cylinders?
- How do viscoelastic fluids behave?

8.2 Equipment Design

For a commercial extractor, several important equipment modifications are required: (1) a sealed design to maintain an internal sterile environment, (2) higher countercurrent axial flow rates, and (3) higher mass transfer coefficients through greater rotation rate differences or cylinder modifications. In addition, several design changes could improve the overall ease of operation. The following list summarizes the design criteria to be considered:

- Sealed system. The annulus should be sealed to allow startup and shutdown while filled with fluids. In addition, an internal sterile environment can then be maintained.
- Startup/shutdown. Provisions must be included to allow (1) removal of air bubbles in the process of filling the device and (2) complete emptying of system after extraction is finished.
- Maintenance access. The design should be as simple as possible to allow for easy clean-up and sterilization of the extractor. Furthermore, access to replace/repair the inlet and outlet ports, seals, and belts should be straightforward.

- Rotary seal design. Rotary seals are notorious trouble spots in rotating equipment and each should be carefully considered. In general, the smaller the seal diameter, the better the sealing performance in addition to reduced drag and power consumption. Two main options exist for the rotary seals: lip seals and mechanical seals. Lip seals are a low precision design and therefore have a lower initial cost but higher maintenance cost. In contrast mechanical seals require very careful machining and installation, and have a higher initial cost but lower maintenance. As a comparison, the Podbielniak has four mechanical seals, which would be the absolute minimum for a two-fluid Taylor-Couette extractor.

- Rotation rate difference. Better mass transfer performance is expected with higher relative rotation rate differences. The rotation rate difference can be limited by (1) emulsion formation due to cylinder misalignment or end conditions or (2) undersized motors.

- Minimum annular gap to minimize hold-up volume and diffusional distances. The practical gap width is determined by machinability and alignment.

- Weir system. The weir system should be designed for volume ratios ranging from 0.1 - 10, which are typical of other centrifugal extractors. Any seals or contacting parts should be isolated as much as possible from the interface to reduce emulsion formation.

- Materials of construction. For biologicals, the system must be sterilizable and for maximum compatibility the number of materials should be minimized. In addition, visualization of the annulus, particularly the ends, aids in troubleshooting.
- Minimal stagnant or high shear Ekman zones.
- Features added to the inner and outer cylinders to promote stronger vortex flows.
- Control system to control the flows rates and the interface position.

The several designs for the next generation extractor are included in Figures 8.1, 8.2, and Figure 8.3. The design in Figure 8.1 is the most similar to the existing equipment and its features include:

- Rotary seals. This design has six rotary seals and two wipers. The two wipers operate as weirs and for end effect reduction. Two large rotary seals provide the connection between the inner and outer cylinder. An alternative would be to have end plates that rotate with the outer cylinder. In this case smaller seals would be required, but an Ekman shear zone would be introduced for each end.

- Hollow inner cylinder. The hollow inner cylinder provides transport of the heavy and light fluids.

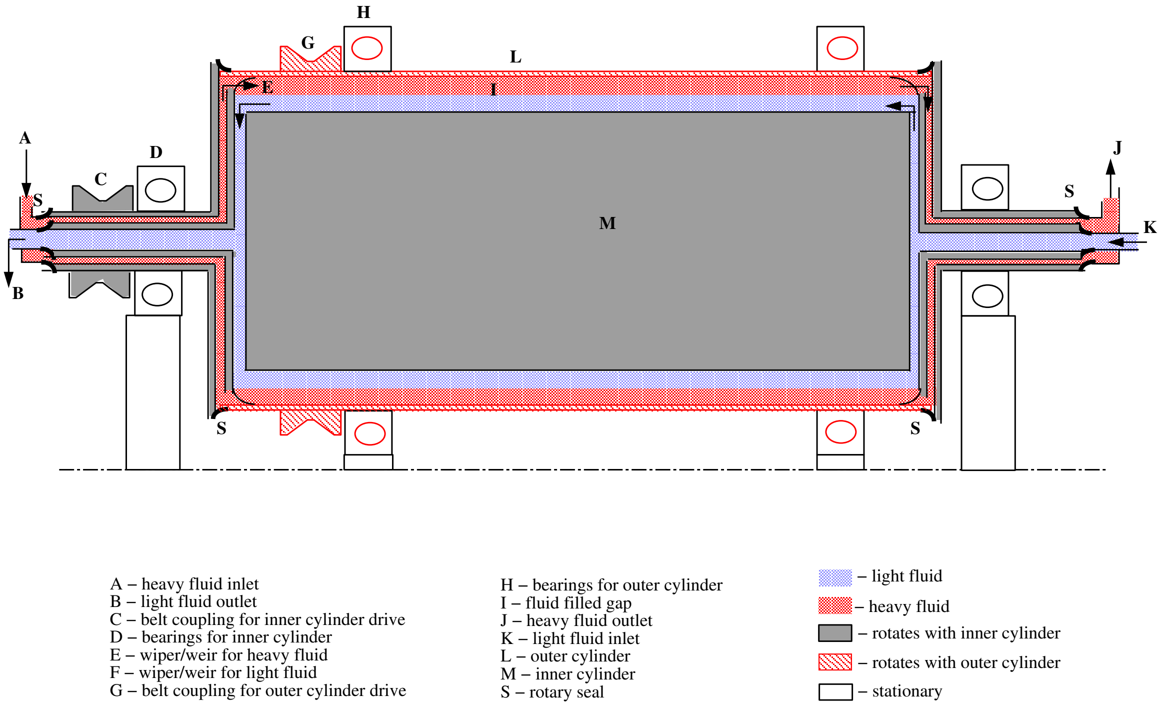

Figure 8.1: Future equipment design option 1

The design in Figure 8.2 is also quite similar to the existing equipment and should not introduce unexpected behavior. The features include:

- Rotary seals. This design incorporates five rotary seals and two wiper seals. Four of the rotary seals isolate the rotating equipment from the inlet and outlet ports and are identical to the Podbielniak design. The fifth rotary seal could be eliminated if the light fluid inlet wiper operates as a seal. The two wipers are primarily to reduce end effects by providing a transition from the inner cylinder rotation to the outer cylinder. However, the sealing action of the wipers will also retard fluid from entering the stagnant Ekman shear zones.
- Hollow cylinders. The inner and outer cylinders are hollow for the introduction and withdrawal of fluids. One side is dedicated to light fluid handling and the other for heavy fluid. The hollow outer cylinder is unusual, but has three purposes (1) to eliminate an Ekman shear zone, (2) provide a balance for the inner cylinder, and (3) eliminate a rotary seal.

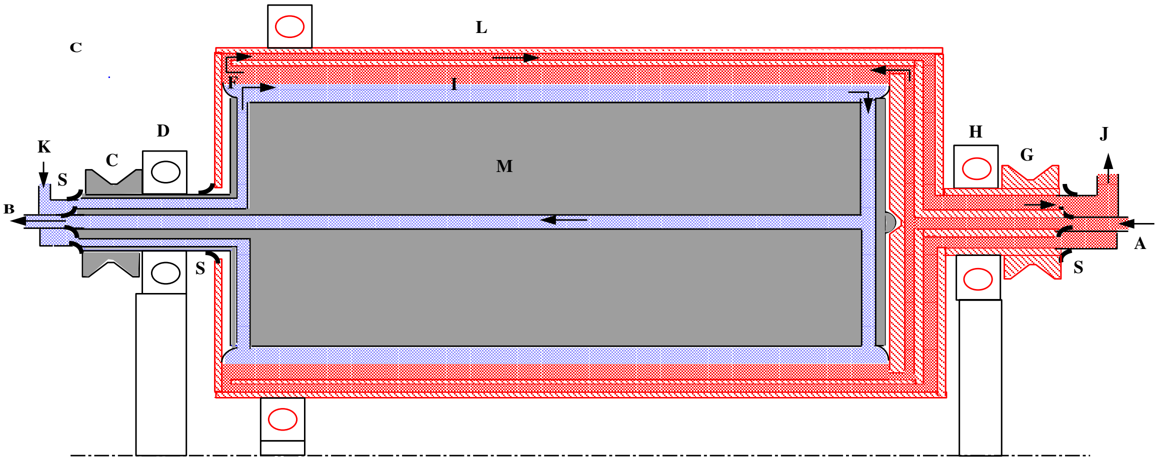

A – heavy fluid inlet
B – light fluid outlet
C – belt coupling for inner cylinder drive
D – bearings for inner cylinder
E – wiper/weir for heavy fluid
F – wiper/weir for light fluid
G – belt coupling for outer cylinder drive

H – bearings for outer cylinder
I – fluid filled gap
J – heavy fluid outlet
K – light fluid inlet
L – outer cylinder
M – inner cylinder
S – rotary seal

▒ – light fluid
▓ – heavy fluid
■ – rotates with inner cylinder
▨ – rotates with outer cylinder
☐ – stationary

Figure 8.2: Future equipment design option 2

The design in Figure 8.3 is the least similar to the existing equipment and could introduce some unexpected behavior. However, the design has several attractive features and should be strongly considered. The design highlights include:

- Stationary end plates. The end plates are stationary to provide very easy access to the annulus. The wipers are weirs that also provide the transition to the rotating cylinders to reduce end effects. This design is very easy to construct. *The major unknown with this design is how will the weirs perform?*

- Rotary seals. There are only four rotary seals in this design. Furthermore, the wipers have little sealing responsibility. The rotary seals, however, are relatively large in diameter.

- No stagnant zones. There are no stagnant zones and the only Ekman zones are in the small inlet and outlet reserviors.

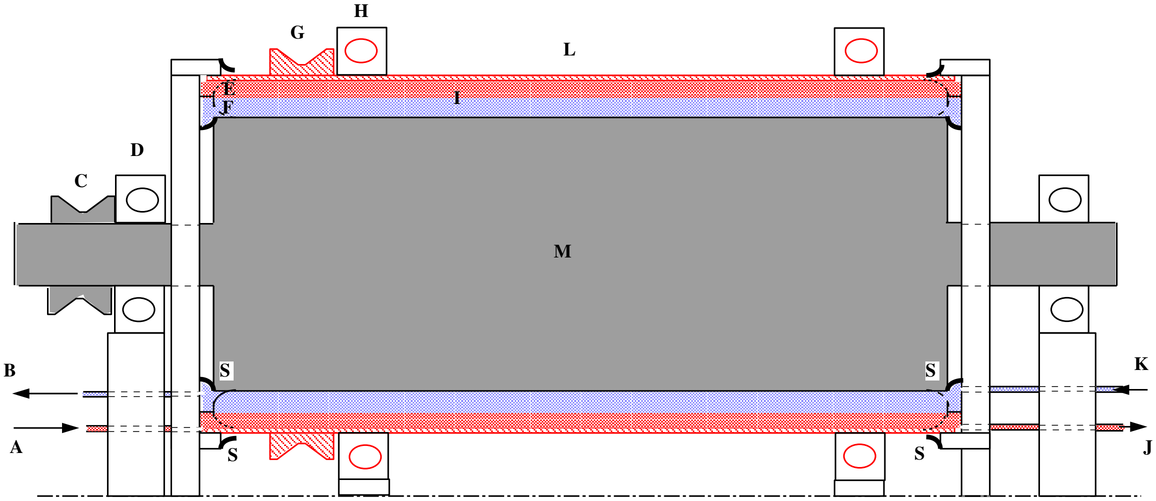

A – heavy fluid inlet
B – light fluid outlet
C – belt coupling for inner cylinder drive
D – bearings for inner cylinder
E – wiper/weir for heavy fluid
F – wiper/weir for light fluid
G – belt coupling for outer cylinder drive

H – bearings for outer cylinder
I – fluid filled gap
J – heavy fluid outlet
K – light fluid inlet
L – outer cylinder
M – inner cylinder
S – rotary seal

🟦 – light fluid
🟥 – heavy fluid
■ – rotates with inner cylinder
▨ – rotates with outer cylinder
☐ – stationary

Figure 8.3: Future equipment design option 3

Notation

a	Mass transfer surface area per unit volume
A	Base flow (two-fluid Couette flow) coefficient
B	Base flow (two-fluid Couette flow) coefficient
c	Growth rate of the disturbance velocities
C	Concentration
$d = R_2 - R_1$	Cylinder gap width (cm)
D	Diffusion coefficient (cm^2/s)
$D = \partial/\partial r$	Derivative operator
$D_* = \partial/\partial r + 1/r$	Derivative operator
D/Dt	Substantial derivative operator
D^*	Dispersion coefficient (cm^2/s)
$Ek_j = \frac{\mu_j}{2\rho_j \Omega_2 d^2}$	Ekman number for phase j
f	Fraction extracted

F	Coefficient in equation for countercurrent axial flow
$Fr = \frac{R_2\Omega_2^2}{g}$	Froude number
G	Coefficient in equation for countercurrent axial flow
H	Coefficient in equation for countercurrent axial flow
$J_2 = \frac{(\rho_2-\rho_1)\Omega_2^2R_2^3}{S}$	Dimensionless group measuring centifugal to surface tension effects
k	Radial mass transfer coefficient in one fluid Taylor-Couette flow
K_j	Overall mass transfer coefficient based on phase j
k_j	Individual mass transfer coefficient for phase j
L	Characteristic length
$m = \frac{C_2^*}{C_1^*}$	Partition coefficient
M_0	Zeroth moment
M_1	First moment
M_2	Second central moment
n	Number of theoretical stages
N	Number of mixing tanks describing axial dispersion
$Nu = \frac{2kd}{D}$	Nusselt number for radial mass transfer in one fluid Taylor-Couette flow
$Nu = \frac{D^*}{D}$	Nusselt number for axial dispersion

$Nu = \frac{K_1 d}{D_2}$	Nusselt number for interphase mass transfer in two-fluid Taylor-Couette flow
p	Disturbance pressure for linear stability analysis
P	Base state pressure profile
P_z	Pressure due to countercurrent axial flow
$Pe = ReSc$	Peclet number
Q	Volumetric flowrate (ml/min)
r	Radial coordinate
R	Cylinder radius (cm)
$R_{12} = R_1/R_2$	Radius ratio
$Re_1 = \frac{\Omega_1 R_1 d}{\nu_1}$	Azimuthal Reynolds number
$Re_\theta = \frac{(\Omega_1 - \Omega_2) R_1 d}{\nu}$	Azimuthal Reynolds number
$Re_{ax} = \frac{\bar{W} d}{\nu}$	Axial Reynolds number
S	Interfacial tension (dyne/cm)
$Sc = \nu/D$	Schmidt number
t	time
$T = -\frac{4\Omega_1^2 d^4 (R_{12}^2 - \Omega_{21})}{\nu^2 (R_{12}^2 - 1)}$	Taylor number for a single fluid
$\bar{T} = -\frac{1}{2}(1+\mu)\frac{4A\Omega_1 d^4}{\nu^2}$	Taylor number for a single fluid with axial flow

$Ta = \frac{\Omega_1 R_1 d}{\nu} \left(\frac{d}{R_1}\right)^{1/2}$	Modified Taylor number
$T_1 = -\frac{4\Omega_1^2 d^4 (R_{1i}^2 - \Omega_{i1})}{\nu_1^2 (R_{1i}^2 - 1)}$	Taylor number for inner fluid
$T_2 = -\frac{4\Omega_i^2 d^4 (R_{i2}^2 - \Omega_{21})}{\nu_2^2 (R_{i2}^2 - 1)}$	Taylor number for outer fluid
u	Characteristic velocity
$\mathbf{v}$	Disturbance velocities for linear stability analysis
V	Azimuthal base flow velocity profile (cm/sec)
W	Axial velocity profile for counterflow (cm/sec)
$\bar{W}$	Average axial velocity (cm/sec)
$x = y - 1/2$	Radial coordinate
$y = r/d - (1-\epsilon)/\epsilon$	Radial coordinate
z	Axial coordinate
Z	Total axial length

Greek characters:

α	Axial wavenumber
$\dot{\gamma} = \frac{\partial v_z}{\partial y}$	Velocity gradient
$\Gamma = Z/R_1$	the aspect ratio of the extractor
δ	Small parameter describing deviations from rigid rotation, the boundary layer thickness, or the taper of interface due to counter flow
$\epsilon = d/R_2$	Narrow gap parameter
θ	Azimuthal coordinate
μ	Dynamic viscosity (g-cm/s)
$\mu_{21} = \mu_2/\mu_1$	Dynamic viscosity ratio
ν	Kinematic viscosity (cm^2/s)
$\nu_{21} = \nu_2/\nu_1$	Kinematic viscosity ratio
ρ	Fluid density (g/ml)
$\rho_{21} = \rho_2/\rho_1$	Density ratio
τ_{ij}	Shear stress acting in the i direction due to a velocity gradient in the j direction
$\Omega = \frac{V}{r}$	Base flow rotation profile
Ω_j	Rotation rate of cylinder j (rad/s or rev/s)
$\Omega_{21} = \Omega_2/\Omega_1$	Rotation rate ratio

Subscripts/Superscripts:

1	Inner fluid or cylinder
2	Outer fluid or cylinder
c	At the critical point
i	Interface
r	Radial direction
z	Axial direction
θ	Azimuthal direction
$*$	At equilibrium or a dimensional quantity
$\hat{}$	Disturbance quantity

Bibliography

[1] A. Acrivos. On the Solution of the Convection Equation in Boundary Layer Flows. *Chem. Eng. Sci.* **17**:457-465. 1962.

[2] A. Acrivos and J.D. Goddard. Asymptotic Expansions for Laminar Convection Heat and Mass Transfer. *J. Fluid Mech.* **23**:273-291. 1965.

[3] P.A. Albertsson. *Partition of Cell Particles and Macromolecules.* John-Wiley and Sons. New York. 3rd ed. 1986.

[4] C.D. Andereck (ed.) *Ordered and Turbulent Patterns in Taylor Couette Flow.* Plenum Press. New York. 1992.

[5] R. Aris. On the Dispersion of a Solute in a Fluid Flowing through a Tube. *Proc. Roy. Soc. Lond. A.* **237**:67-77. 1956.

[6] G. Baier, T.M. Grateful, M.D. Graham, and E.N. Lightfoot. Prediction of Mass Transfer in Spatially Periodic Systems. *Chem. Eng. Sci.* **54**:343-355. 1999.

[7] G. Baier and M.D. Graham. Two-Fluid Taylor-Couette Flow: Experiments and Linear Theory for Immiscible Liquids between Corotating Cylinders. *Phys. Fluids.* **10**(12):3045-3055. (1998).

[8] G. Baier and M.D. Graham. Two-Fluid Taylor-Couette Flow: Experiments and Linear Theory for Immiscible Liquids between Corotating Cylinders with Countercurrent Axial Flow. Preprint. 1999.

[9] R.B. Bird, W.E. Stewart, and E.N. Lightfoot. *Transport Phenomena.* John Wiley and Sons. New York. 1960.

[10] H. Brenner. Dispersion Resulting from Flow through Spatially Periodic Porous Media. *Phil. Trans. R. Soc. Lond. A.* **297**:81-133. 1980.

[11] M.E. Brewster, K.Y. Chung, and G. Belfort. Dean Vortices with Wall Flux in a Curved Channel Membrane System. 1. A New Approach to Membrane Module Design. *J. Mem. Sc.* **81**:127-137. 1993.

[12] R.J. Campero and R.D. Vigil. Spatio-temporal Patterns in Liquid-Liquid Taylor-Couette-Poiseuille Flow. *Phys. Rev. Lett.* Preprint.

[13] C. Canuto, M.Y. Hussaini, A. Quarteroni, and T.A. Zang, *Spectral Methods in Fluid Dynamics.* Springer. 1988.

[14] S. Chandrasekhar. *Hydrodynamic and Hydromagnetic Stability.* Dover Publications. New York. 1981.

[15] K.Y. Chung, R. Bates, and G. Belfort. Dean Vortices with Wall Flux in a Curved Channel Membrane System. 4. Effect of Vortices on Permeation Fluxes of Suspensions in Microporous Membrane. *J. Mem. Sc.* **81**:139-150. 1993.

[16] F. Coeuret and J. Legrand. Mass Transfer at the Electrodes of Concentric Cylindrical Reactors Combining Axial Flow and Rotation of the Inner Cylinder. *Electrochimica Acta.* **26**:865-872. 1981.

[17] S. Cohen and D.M. Marom. Experimental and Theoretical Study of a Rotating Annular Flow Reactor. *Chem. Eng. J.* **27**:87-97. 1983.

[18] W.D. Conway and R.J. Petroski (eds.) *Modern Counter-current Chromatography.* ACS Symposium Series No. 593. American Chemical Society. Washington, D.C. 1995.

[19] E. Cussler, *Diffusion: Mass Transfer in Fluid Systems.* Cambridge University Press (1997).

[20] L. Dahuron and E.L. Cussler. Protein Extractions with Hollow Fibers. *AIChE J.* **34**(1):130-136. 1988.

[21] A. Davey. The Growth of Taylor Vortices in Flow between Rotating Cylinders. *J. Fluid Mech.* **14**:336-368. 1962.

[22] M. Davis and E. Weber. Liquid Liquid Extraction between Rotating Cylinders. *Ind. Eng. Chem.* **52**(11):929-934. 1960.

[23] M. Dekker, K. van 'T Riet, S.R. Weijers, J.W.A. Baltussen, C. Laane, and B.H. Bijsterbosch. Enzyme Recovery by Liquid-Liquid Extraction Using Reversed Micelles. *Chem. Eng. J.* **33**:B27-B33. 1986.

[24] G. Desmet, H.Verelst, and G.V. Baron. Local and Global Dispersion Effects in Couette-Taylor Flow - I. Description and Modeling of the Dispersion Effects. *Chem. Eng. Sci.* **51**(8):1287-1298. 1996.

[25] G. Desmet, H.Verelst, and G.V. Baron. Local and Global Dispersion Effects in Couette-Taylor Flow - II. Quantitative Measurements and Discussion of the Reactor Performance. *Chem. Eng. Sci.* **51**(8):1299-1309. 1996.

[26] M. A. Dominguez-Lerma, G. Ahlers, and D.S. Cannell. Effects of “Kalliroscope” Flow Visualization Particles on Rotating Couette-Taylor Flow. *Phys. Fluids.* **28**(4):1204-1206. 1985.

[27] R.J. Donnelly. Taylor-Couette Flow: The Early Days. *Phys. Today.* Nov.:32-39. 1991.

[28] R.J. Donnelly and D. Fultz. Experiments on the Stability of Spiral Flow between Rotating Cylinders. *Proc. Nat. Acad. Sci.* **46**:1150-1154. 1960.

[29] J. Dos Reis Coimbra, J. Thommes, and M.-R. Kula. Continuous Separation of Whey Proteins with Aqueous Two-Phase Systems in a Graesser Contactor. *J. Chrom. A.* **668**:85-94. 1994

[30] P.G. Drazin and W.H. Reid. *Hydrodynamic Stability.* Cambridge University Press. Cambridge. 1981.

[31] M. Eisenberg, C.W. Tobias, and C.R. Wilke. Mass Transfer at Rotating Cylinders. *Chem. Eng. Prog. Symp. Ser.* **No. 16**(Vol. 51): 1-16. 1955.

[32] Y. Enokida, K. Nakata, and A. Suzuki. Axial Turbulent Diffusion in Fluid between Rotating Coaxial Cylinders. *AIChE J.* **35**(7):1211-1214. 1989.

[33] H. Fasel and O. Booz. Numerical Investigation of Supercritical Taylor-vortex Flow for a Wide Gap. *J. Fluid Mech.* **138**:21-52. 1984.

[34] J.R. Flower, N. Macleod, and A.P. Shahbenderian. The Radial Transfer of Mass and Momentum in an Axial Fluid Stream between Coaxial Rotating Cylinders - I Experimental Measurements. *Chem. Eng. Sci.* **24**:637-650. 1969.

[35] J.R. Flower and N. Macleod. The Radial Transfer of Mass and Momentum in an Axial Fluid Stream between Coaxial Rotating Cylinders - II. The Analogy between Mass and Momentum Transfer in Streams Containing Secondary Flows. *Chem. Eng. Sci.* **24**:651-662. 1969.

[36] C.T. Gallagher, D.T. Leighton, and M.J. McCready. Experimental Investigation of a Two-Layer Shearing Instability in a Cylindrical Couette Cell. *Phy. Fluids.* **8**(9):2385-2392. 1996.

[37] B.S. Garbow. Algorithm 535: the QZ Algorithm to Solve the Generalized Eigenvalue Problem for Complex Matrices. *ACM Trans. Math. Software.* **4**:404-410. 1978.

[38] K. Gebauer, L. Steiner, S. Hartland. Centrifugal Extraction with Axial Countercurrent Flow. *Ger. Che. Eng.* **6**:381-386. 1983.

[39] R.C. Giordano, R.L.C. Giordano, D.M.F. Prazeres, and C.L. Cooney. Analysis of a Taylor-Poiseuille Vortex Flow Reactor - I: Flow Patterns and Mass Transfer Characteristics. *Chem. Eng. Sci.* **53**(20):3635-3652. 1998.

[40] J.C. Godfrey and M.J. Slater (eds.) *Liquid-Liquid Extraction Equipment.* John Wiley and Sons. Chichester. 1994.

[41] N.F.Gordon, C.M.V.Moore, and C.L. Cooney. An Overview of Continuous Protein Purification Processes. *Biotec. Adv.* **8**:741-762. 1990.

[42] J.Green and W.M. Jones. Couette Flow of Dilute Solutions of Macromolecules: Embryo Cells and Overstability. *J. Fluid Mech.* **119**:491. 1982.

[43] J. Grifoll, X. Farriol, and F. Giralt. Mass Transfer at Smooth and Rough Surfaces in a Circular Couette Flow. *Int. J. Heat Mass Transfer.* **29**(12):1911-1918. 1986.

[44] Z.H. Gu and T.Z. Fahidy. Mass Transport in the Taylor-Vortex Regime of Rotating Flow. *Chem. Eng. Sci.* **40**:1145-1153. 1985.

[45] D. Haim and L.M. Pismen. Performance of a Photochemical Reactor in the Regime of Taylor-Görtler Vortical Flow. *Chem. Eng. Sci.* **49**(8):1119-1129.1994.

[46] U.B. Holeschovsky and C.L. Cooney. Quantitative Description of Ultrafiltration in a Rotational Filtration Device. *AIChE J.* **37**(8):1219-1226. 1991.

[47] A.E. Hosoi and L. Mahadevan. Axial Instability of a Free-Surface Front in a Partially Filled Horizontal Rotating Cylinder. Preprint. 1997.

[48] T. Howes and M. Rudman. Flow and Axial Dispersion Simulation for Travelling Axisymmetric Taylor Vortices. *AIChE J.* **44**(2):255-262. 1998.

[49] H.C. Hu and R.E. Kelly. Effect of a Time-Periodic Axial Shear Flow upon the Onset of Taylor Vortices. *Phys. Rev. E.* **51**(4):3242-3251. 1995.

[50] J.G. Huddleston and A. Lyddiatt. Aqueous Two-Phase Systems in Biochemical Recovery. *Appl. Biochem. Biotech.* **Jan.**:249-279. 1990.

[51] H.Hustedt, K.H. Kroner, U. Menge, and M.R. Kula. Enzyme Purification by Liquid-Liquid Extraction. *Enzy. Eng.* (H.H. Weetall and G.P.Royer, eds.) **Vol.5**:45-47. 1981.

[52] H. Hustedt, K.-H. Kroner, and N. Papamichael. Continuous Cross-Current Aqueous Two-Phase Extraction of Enzymes from Biomass. *Proc. Biochem.* **Oct.**:129-137. 1988.

[53] G. Iosilevskii, H. Brenner, C.M.V. Moore, and C.L.Cooney. Mass Transport and Chemical Reaction in Taylor Vortex Flows with Entrained Catalyst Particles: Applications to a Novel Class of Immobilized Enzyme Biochemical Reactors. *Phil. Trans. R. Soc. Lond. A.* **345**:259-294. 1993.

[54] Y.Ito and W.D. Conway (eds.) *High-Speed Countercurrent Chromotography.* John Wiley and Sons. New York. 1996.

[55] D.A. Janes, N.H. Thomas, and J.A. Callow. Demonstration of a Bubble Free Annular Vortex Membrane Bioreactor for Batch Culture of Red Beet Cells. *Biotech. Tech.* **1**(4):257-262. 1987.

[56] D.D. Joseph, K. Nguyen, and G.S.Beavers. Non-uniqueness and Stability of the Configuration of Flow of Immiscible Fluids with Different Viscosities. *J. Fluid Mech.* **141**:319-345. 1984.

[57] D.D. Joseph, Y.Renardy, M.Renardy, and K. Nguyen. Stability of Rigid Motions and Rollers in Bicomponent Flows of Immiscible Liquids. *J. Fluid Mech.* **153**:151-165. 1985.

[58] D.D. Joseph, Y.Y.Renardy. *Fundamentals of Two-Fluid Dynamics. Part 1: Mathematical Theory and Applications*. Springer-Verlag. New York. 1993.

[59] J.B. Joshi, S.B. Sawant, K.S.M.S. Raghava Rao, T.A. Patil, K.M. Rostami, and S.K. Sikdar. Continuous Counter-Current Two-Phase Aqueous Extraction. *Bioseparation.* **1**:311-324. 1990.

[60] K. Kadam. Reverse Micelles as a Bioseparation Tool. *Enzyme Microb. Technol.* **8**:266-273. 1986.

[61] R. Kappesser, I. Cornet, and R. Greif. Mass Transfer to a Rough Rotating Cylinder. *J. Electrochem. Soc.* **118**(12):1957-1959. 1971.

[62] K.Kataoka, H.Doi, T.Hongo, and M. Futagawa. Ideal Plug-Flow Properties of Taylor Vortex Flow. *J. Chem. Eng. Japan.* **8**(6):472-476. 1975.

[63] K. Kataoka and T. Takigawa. Intermixing over Cell Boundary between Taylor Vortices. *AIChE J.* **27**(3):504-508. 1981.

[64] Y. Kawase and J.J. Ulbrecht. Laminar Mass Transfer between Concentric Rotating Cylinders in the Presence of Taylor Vortices. *Electrochimica Acta.* **33**(2):199-203. 1988.

[65] E.L. Koschmieder. *Bénard Cells and Taylor Vortices.* Cambridge University Press. New York. 1993.

[66] E.L. Koschmieder. Taylor Vortices between Eccentric Cylinders. *Phys. Fluids.* **19**(1):1-4. 1976.

[67] K.H.Kroner, V.Nissinen, and H. Ziegler. Improved Dynamic Filtration of Microbial Suspensions. *Biotech.* **5**:921-924. 1987.

[68] K.H. Kroner and V. Nissinen. Dynamic Filtration of Microbial Suspensions Using and Axially Rotating Filter. *J. Mem. Sci.* **36**:85-100. 1988.

[69] E.R. Krueger, A. Gross, and R.C. Di Prima. On the Relative Importance of Taylor Vortex and Non-axisymmetric Modes in Flow between Rotating Cylinders. *J. Fluid Mech.* **24**:521-538. 1966.

[70] J. Legrand, P. Dumargue, and F. Coeuret. Overall Mass Transfer to the Rotating Inner Electrode of a Concentric Cylindrical Reactor with Axial Flow. *Electrochimica Acta.* **25**:669-673. 1980.

[71] J. Legrand and F. Coeuret. Circumferential Mixing in One-Phase and Two-Phase Taylor Vortex Flows. *Chem. Eng. Sci.* **41**(1):47-53. 1986.

[72] R.A. Leonard, D.B. Chamberlain, and C. Conner. Centrifugal Contactors for Laboratory Scale Solvent Extraction Tests. *Sep. Sci. Tech.* **32**(1-4):193-210. 1997.

[73] O. Levenspiel. *Chemical Reaction Engineering.* John Wiley and Sons. New York. 2nd Ed. 1972.

[74] E.N. Lightfoot. "Estimation of Heat and Mass Transfer Rates" in *Lectures in Transport Phenomena.* A.I.Ch.E. Continuing Education Series #4. 1969.

[75] T.C. Lo, M.H.I. Baird, and C. Hanson. *Handbook of Solvent Extraction.* John Wiley and Sons. New York. 1983.

[76] R.M. Lueptow, A. Docter, and K. Min. Stability of Axial Flow in an Annulus with a Rotating Inner Cylinder. *Phys. Fluids A.* **4**(11):2446-2455. 1992.

[77] N. Macleod and T. Ruess. The Radial Transfer of Mass to an Axial Stream of Liquid between Coaxial Rotating Cylinders. *Chem. Eng. Sci.* **30**:235-242. 1975.

[78] P.S. Marcus. Simulation of Taylor-Couette Flow. Part I. Numerical Methods and Comparison with Experiments. *J. Fluid Mech.* **146**:45-64. 1984.

[79] P.S. Marcus. Simulation of Taylor-Couette Flow. Part II. Numerical Results for Wavy-Vortex Flow with One Travelling Wave. *J. Fluid Mech.* **146**:65-113. 1984.

[80] P. Matisse and M. Gorman. Neutrally Buoyant Anisotropic Particles for Flow Visualization. *Phys. Fluids.* **27**(4):759-760. 1984.

[81] B. Mattiasson. Applications of Aqueous Two-Phase Systems in Biotechnology. *Trends Biotech.* **1**(1):16-20. 1983.

[82] K. Min and R.M. Lueptow. Circular Couette Flow with Pressure Driven Axial Flow and a Porous Inner Cylinder. *Exp. Fluids.* **17**:190-197. 1994.

[83] C. Moore and C. Cooney. Axial Dispersion in Taylor-Couette Flow. *AIChE J.* **41**(3):723-727. 1995.

[84] T. Murase, E. Iritani, P. Chidphong, K. Kano, K. Atsumi, and M. Shirato. High-Speed Microfiltration Using a Rotating Cylindrical Ceramic Membrane. *Intl. Chem. Engr.* **31**(2):370-378. 1991.

[85] B.S. Ng and E.R. Turner. On the Linear Stability of Spiral Flow between Rotating Cylinders. *Proc. R. Soc. Lond. A.* **382**:83-102. 1982

[86] N. Ohmura, K. Kataoka, Y. Shibata, and T. Makino. Effective Mass Diffusion over Cell Boundaries in a Taylor-Couette Flow System. *Chem. Eng. Sci.* **52**(11):1757-1765. 1997.

[87] N. Papamichael, B. Börner, and H. Hustedt. Continuous Aqueous Phase Extraction of Proteins: Automated Processing and Recycling of Process Chemicals. *J. Chem. Tech. Biotech.* **54**:47-55. 1992.

[88] J. Parker and P. Merati. An Investigation of Turbulent Taylor-Couette Flow Using Laser Doppler Velocimetry in a Refractive Index Matched Facility. *J. Fluids Eng.* **118**:810-818. 1996.

[89] T.A. Patil, K. Rostami Jafarabad, S.B. Sawant, and J.B. Joshi. Enzyme Mass Transfer Coefficient in Aqueous Two Phase System Using a Packed Extraction Column. *Can. J. Chem. Eng.* **69**:548-556. 1991.

[90] P.I. Pudijiono, N.S. Tavare, J. Garside, and K.D. P. Nigam. Residence Time Distribution from a Continuous Couette Flow Device. *Chem. Eng. J.* **48**:101-110. 1992.

[91] P.I. Pudijiono and N.S. Tavare. Residence Time Distribution Analysis from a Continuous Couette Flow Device around Critical Taylor Number. *Can. J. Chem. Eng.* **71**:312-318. 1993.

[92] R.S. Rahaman, J.Y. Chee, J.M.S. Cabral, and T.A. Hatton. Recovery of an Extracellular Alkaline Protease from Whole Fermentation Broth Using Reversed Micelles. *Biotech. Prog.* **4**(4):218-224. 1988.

[93] Y. Renardy and D.D. Joseph. Couette Flow of Two Fluids between Concentric Cylinders. *J. Fluid Mech.* **150**:381-394. 1985.

[94] M.N. Rosenbluth, H.L. Berk, I. Doxas, and W. Horton. Effective Diffusion in Laminar Convective Flows. *Phys. Fluids.* **30**(9):2636-2647. 1987.

[95] S.B. Sawant, S.K. Sikdar, and J.B. Joshi. Hydrodynamics and Mass Transfer in Two-Phase Aqueous Extraction Using Spray Columns. *Biotech. Bioeng.* **36**:109-115. 1990.

[96] J.F. Scamehorn and J.H. Harwell (ed.) *Surfactant-Based Separation Processes.* Marcel Dekker. New York and Basel. 1989.

[97] G.P. Schneyer and S.A. Berger. Linear Stability of the Dissipative, Two-Fluid Cylindrical Couette Problem. Part 1. The Stably-Stratified Hydrodynamic Problem. *J. Fluid Mech.* **45**:91-110. 1971.

[98] D.A. Simmers and J.E.R. Coney. A Reynolds Analogy Solution for the Heat Transfer Characteristics of Combined Taylor Vortex and Axial Flows. *Int. J. Heat Mass Trans.* **22**:679-689. 1979.

[99] V. Sobolik, B. Benabes, and G. Cognet. Study of Taylor-Couette Flow Using a Three-segment Electrodiffusion Probe. *J. Appl. Electrochem.* **25**(5):441-449. 1995.

[100] R. Spence and R.J.W. Streeton. Counter-Current Liquid-Liquid Extraction in Annulus Columns with Shearing Motion. *Atom. Energy Res. Estab.* (U.K.) Report No. R4091:33. 1962.

[101] W.E. Stewart. Forced Convection in 3-D Flows. I. Asymptotic Solutions for Fixed Interfaces. *AIChE J.* **9**:528-535. 1963.

[102] A.B. Strong and L. Carlucci. An Experimental Study of Mass Transfer in Rotating Couette Flow with Low Axial Reynolds Number. *Can. J. Chem. Eng.* **54**:295-299. 1976.

[103] W.S. Saric and Z. Lavan. Stability of Circular Couette Flow of Binary Mixtures. *J. Fluid Mech.* **47**:65-80. 1971.

[104] D.I. Takeuchi and D.F. Jankowski. A Numerical and Experimental Investigation of the Stability of Spiral Poiseuille Flow. *J. Fluid Mech.* **102**:101-126. 1981.

[105] W. Tam and H. Swinney. Mass Transport in Turbulent Couette-Taylor Flow. *Phys. Rev. A.* **36**(3):1374-1381. 1987.

[106] G.I. Taylor. Stability of a Viscous Liquid Contained between Two Rotating Cylinders. *Phil. Trans. R. Soc. Lond. A.* **223**:289-343. 1923.

[107] G.I. Taylor. Dispersion of Soluble Matter in Solvent Flowing Slowly through a Tube *Proc. Roy. Soc. Lond. A.* **219**:186-203. 1953.

[108] J.D. Thornton. *Science and Practice of Liquid-Liquid Extraction.* Vol. 2. Oxford University Press. New York. 1992.

[109] J.D. Thornton and H.R.C. Pratt. Liquid-Liquid Extraction: Part VII. Flooding Rates and Mass Transfer Data for Rotary Annular Columns. *Trans. Instn. Chem. Engrs.* **31**:289. 1953.

[110] Y. Toya and I. Nakamura. Instability of Two-Fluid Taylor Vortex Flow. *Trans. Japan Soc. Mech. Engr. Part B.* **63**(612):35-43. 1997.

[111] R.E. Treybal. *Liquid Extraction.* McGraw-Hill Book Company. 1963.

[112] P.L. Versteegen and D.F. Jankowski. Experiments on the Stability of Viscous Flow between Eccentric Rotating Cylinders. *Phys. Fluids.* **12**(6):1138-1143. 1969.

[113] H. Walter and G. Johansson. *Methods in Enzymology. Vol. 228. Aqueous Two-Phase Systems.* Academic Press. San Diego. 1994.

[114] T. Wei, E.M. Kline, S.H.-K. Lee, and S. Woodruff. Görtler Vortex Formation at the Inner Cylinder in Taylor Couette Flow. *J. Fluid Mech.* **245**:47-68. 1992.

[115] M. Wimmer. An Experimental Investigation of Taylor Vortex Flow between Conical Cylinders. *J. Fluid Mech.* **292**:205-227. 1995.

[116] H. Winzeler and G. Belfort. Enhanced Performance for Pressure-Driven Membrane Processes: the Argument for Fluid Instabilities. *J. Mem. Sc.* **80**:35. 1993.